

THESIS

QUATERNARY ALLUVIAL LINEAMENTS IN THE ATACAMA DESERT, NORTHERN CHILE:  
MORPHOLOGY, RELATIONSHIPS TO BEDROCK STRUCTURES, AND LINK TO THE SEISMIC CYCLE  
OF THE ANDEAN SUBDUCTION MARGIN

Submitted by

Emily A. Perman

Department of Geosciences

In partial fulfillment of the requirements

For the Degree of Master of Science

Colorado State University

Fort Collins, Colorado

Spring 2023

Master's Committee:

Advisor: John Singleton  
Co-Advisor: Sean Gallen

Aditi Bhaskar

Copyright by Emily A. Perman 2023

All Rights Reserved

## ABSTRACT

### QUATERNARY ALLUVIAL LINEAMENTS IN THE ATACAMA DESERT, NORTHERN CHILE: MORPHOLOGY, RELATIONSHIPS TO BEDROCK STRUCTURES, AND LINK TO THE SEISMIC CYCLE OF THE ANDEAN SUBDUCTION MARGIN

Located in the upper plate of the modern Nazca-South American subduction zone, the hyperarid Atacama Desert is an ideal place to study forearc deformation through surface geomorphology. We studied neotectonic lineaments in alluvium between  $\sim 25.5^\circ$  and  $26^\circ$  S in the Coastal Cordillera with the goal of understanding modern forearc strain. Visible in satellite imagery, these lineaments are defined by linear to curvilinear structures consisting of subparallel ridges that range from tens of meters to kilometers in length. Field observations and 10 cm-resolution digital elevation models (DEMs) derived from drone imagery record a consistent, asymmetrical “ridge-trough-ridge” morphology that commonly traces into  $\sim 1\text{--}2$  m-wide bedrock fissures containing gypsum and calcite. Most lineaments in this region trend  $\sim$ N-S to NW-SE, parallel to the dominant bedrock structural grain and the Cretaceous Atacama and Taltal fault systems. Small-scale faults found in the lineament ridges have cm- to mm-scale apparent normal-sense displacement and consistently dip moderately to steeply ( $50\text{--}70^\circ$ ) towards the lineament troughs, defining a graben-like structure. In outcrop, these normal fault zones are enhanced by differential erosion, and in thin section faulted material is distinguishable by increased cementation within fractures penetrating grain boundaries. A tuff deposit within an alluvial fan containing several lineaments yields a zircon U-Pb age of  $2.2 \pm 0.1$  Ma, indicating that lineaments in this fan are Quaternary in age and likely related to upper plate strain due to modern subduction along the Nazca-South American plate boundary. Older alluvial surfaces tend to have lineaments with broader and taller ridges than those formed on relatively younger alluvial surfaces, indicating that these structures formed progressively through time. In addition, profile data gathered from DEMs show a weak linear correlation between lineament trough width and ridge height, meaning that wider lineaments tend to have taller ridges. Along the flanks of two trenched ridges, we observed shallowly-dipping planes that resemble thrust faults, suggesting the ridges may have formed in response to contractional deformation. We propose the lineaments record alternating forearc shortening and extension related to interseismic and coseismic phases of the earthquake cycle, with the

development of ridges and thrust faults recording interseismic shortening and normal faults and fissures which form the central troughs recording coseismic extension.

## ACKNOWLEDGEMENTS

I wish to express my most sincere thanks to both my advisors, Dr. John Singleton and Dr. Sean Gallen. Their continuous enthusiasm, support, mentorship, and encouragement kept me going through the past three and a half years.

This research project owes its success in part to its many collaborators, individuals from Colorado State University, Pontificia Universidad Católica de Chile, University of Colorado Boulder, University of California Santa Cruz, and others. I've met so many remarkable people over the course of this project and visited countless beautiful places. For this I am incredibly grateful. I would like to personally thank Dr. Nikki Seymour and Dr. Skyler Mavor for their excellent mentorship and for their vital contributions to this project.

Funding for this project was provided in part by research grants from the National Science Foundation. I wish to thank the Warner College of Natural Resources: Department of Geosciences for research and teaching fellowships that provided support during my graduate studies.

I received so much support from my family over the course of my time in graduate school. It is truly humbling, and I wish to express my deepest thanks to all my family members.

Lastly, I am so very grateful for the support of my partner, Jonathan. I couldn't have finished this without your constant encouragement, endless patience, and unfaltering optimism.

*Thank you to everyone who believed in me.*

## TABLE OF CONTENTS

ABSTRACT .....	ii
ACKNOWLEDGEMENTS.....	iv
LIST OF SUPPLEMENTARY DATA INCLUDED SEPARATELY .....	vii
1. INTRODUCTION .....	1
2. GEOLOGIC HISTORY.....	3
2.1. Tectonic Setting.....	3
2.2. Bedrock Geology.....	3
2.3. Geomorphology.....	6
2.3.1. Geomorphology of the Coastal Cordillera .....	6
2.3.2. Geomorphology of the Central Depression.....	6
2.4. Climate and Soil Chemistry.....	7
2.5. Seismicity .....	8
3. METHODS.....	10
3.1. Mapping Lineaments.....	10
3.2. Sources of Error in Mapping Lineaments.....	12
3.3. Drone Imaging and Photogrammetry .....	12
3.4. Sources of Error in Photogrammetry.....	12
3.5. DEM Analysis .....	14
3.6. Lineament Orientations .....	14
3.7. Structural Data.....	15
3.8. Alluvium Samples .....	15
3.9. Mapping Relative Age of Alluvial Surfaces.....	15
3.10. U-Pb Geochronology.....	16
4. RESULTS.....	17
4.1. Lineament Occurrence and Morphology .....	17
4.2. Lineaments and Bedrock .....	17

4.3. Lineament Orientation.....	22
4.4. Lineament Height, Width, and Relative Age.....	22
4.5. Cross-Section Exposures of Lineaments .....	30
4.6. U-Pb Geochronology.....	36
5. DISCUSSION.....	40
5.1. Spatial Relationship to Bedrock Features.....	40
5.2. Structural Features in Alluvium of Lineament Ridges .....	40
5.3. Scaling Relationships and Spatial Trends Along Alluvial Surfaces of Different Ages .....	40
5.4. Geochronology .....	41
5.5. Hypotheses for Lineament Genesis .....	41
5.6. The Seismic Cycle in Subduction Systems .....	44
6. CONCLUSIONS .....	48
6.1. Review of Key Findings.....	48
6.2 Future Work .....	49
REFERENCES .....	50
APPENDIX A: DIGITAL ELEVATION MODELS AND DRONE IMAGERY.....	59

LIST OF SUPPLEMENTARY DATA INCLUDED SEPARATELY

Map 1: Chapter 4 Alluvial Lineaments Map, Northern Atacama Desert, Chile

Dataset 1: Chapter 4 Zircon U-Pb analytical data

## 1. INTRODUCTION

In both the forearc and Precordillera of the northern Chilean Andes, we observed enigmatic landforms in alluvial deposits of the Atacama Desert. When viewed in aerial and satellite imagery, these landforms appear as linear features, which we generally refer to as “lineaments.” For the rest of this work, I will be referring to these landform structures as such. In the field, lineaments have characteristic topographies that consist of longitudinally continuous sets of ridges, ~0.5–3 meters in relief, that in cross-section form symmetric to asymmetric M-shaped topographic profiles. These landforms are concentrated between ~25.5–26° S in alluvial deposits in the Coastal Cordillera, but some are found as far east as the Precordillera. It is vital to study these features in this area because many well-preserved examples can be found here. These lineaments trace into bedrock exposures, so they also provide insight into how deformation is expressed in bedrock and influenced by older structures. In addition, incised exposures of alluvium in this area offer the potential for understanding the geometry of surficial deformation associated with the lineaments.

Relatively few studies have addressed these lineaments. In Arabasz’s (1971) study, he conducted a comprehensive study of the Atacama fault system near 24–26°S, including the geomorphology of the region. In his geomorphological section, he collected a variety of data on the lineaments, which he called “ridge-trench-ridge” features. Arabasz observed the nature of the alluvium on the ridges and in the troughs, finding a higher concentration of coarse material on the ridges. He made a series of plane-table elevation profiles across the lineaments, noting their characteristic M-shaped morphology with the bottom of the trench consistently lower than that of the surrounding, undisturbed alluvium. Along with the elevation transects, Arabasz conducted penetration tests of the alluvium comprising the lineaments, finding that shear stress tended to increase with depth and that, often, the ridges penetrated more easily than the troughs. He also noted their tendency to overlie mapped bedrock faults, though he observed that frequently there is no clear vertical offset across them (Arabasz, 1971).

Audin et al. (2003) studied lineaments farther east in the Chilean Precordillera, where the lineaments are associated with the Domekyo fault system. They document deflections of intermittent fluvial systems across the lineaments, which overlie a series of normal faults creating half-grabens (Audin et al., 2003). This study was not

focused on identifying lineaments as a unique landform, though it does showcase the tendency for lineaments to overly bedrock faults.

In both studies, lineaments are referred to generally as “fault scarps.” Arabasz (1971) entertains both non-tectonic and tectonic components regarding the origins of these features, noting faulted alluvium along the lineament traces. Ultimately, he suggests that the shrink-swell action of expansive soils could potentially create a wedge-shaped structure responsible for the ridges and trough, though he still notes the possibility of a tectonic component (Arabasz, 1971). Considering these studies, much can still be learned about these landforms. A knowledge gap exists concerning their spatial distribution and any overall patterns in their orientation, and additional data are needed regarding their geomorphology and structural geometry. Little is known of their internal structure except for what Arabasz (1971) gathered from the penetration tests. Digital elevation datasets covering lineament topography, including the surrounding alluvial fans, are also lacking.

This study addresses some of these knowledge gaps and builds on preliminary work conducted by Dr. Skyler Mavor and Dr. Rodrigo Gomila in 2018 (e.g., Mavor, 2021, Chapter 3), data and observations which are incorporated into this investigation. Through the lens of tectonic geomorphology and structural geology, this study utilizes field work, remote sensing techniques, topographic analysis, and geochronology to map the spatial distribution, characterize the morphology and clarify the origins of these mysterious features. The map drafted in this study contains thousands of lineament segments mapped from satellite imagery, and the orientations of lineament segments are compared to the orientations of known bedrock faults. This study visited dozens of lineament sites in the field, focusing specifically on cuts in the alluvial fans that exposed lineaments in cross-section. We also dug several trenches by hand through sections of lineament ridges. This study utilized a large amount of digital data, including hundreds of drone photographs of lineaments, cm-scale digital elevation models, and locations of lineament ridges mapped on top of satellite images. In addition, this study contains samples of alluvium from fault zones found in lineament cross-section exposures, as well as an age constraint provided by an ash-fall tuff. Finally, we provide some evidence for how the features change through time, by analyzing the changes in elevation across alluvial fan surfaces of different ages and provide a potential model for their formation.

## 2. GEOLOGIC HISTORY

### 2.1 Tectonic Setting

Known colloquially as “the driest place on the planet”, the Atacama Desert comprises the northernmost third of Chile (Figure 1a). The region is bounded to the east by the Andes Mountains, which owe their extreme topography to the E-dipping Nazca-South American subduction zone. At present, this convergent plate boundary reflects the coupled interaction between the Nazca and South American plates. The Andean convergence cycle initiated after the supercontinent Gondwana broke apart in the Late Triassic to Early Jurassic (e.g., Mpodozis and Ramos, 1989; Charrier et al., 2007). The direction of convergence and the degree of plate coupling has varied, as reflected by alternating periods of upper plate margin-parallel shortening, extension, and strike-slip movement (Scheuber and Gonzalez, 1999; Charrier et al., 2007; Horton, 2018). Much of the basement in the Coastal Cordillera in northern Chile is comprised of the Jurassic-aged magmatic arc, indicating that ~200 km of the forearc has been removed by subduction erosion since the start of the Andean convergence cycle (Allmendinger et al., 2010). Convergence rates and directions have changed over the lifetime of the subduction margin. Convergence rates declined in the Oligocene/Early Miocene, likely resulting from highly oblique subduction (Pardo-Casas and Molnar, 1987; Somoza, 1998; Allmendinger et al., 2010). Orthogonal plate boundary convergence reached its maximum in the mid-Miocene, with rates up to 15 cm/year (Pardo-Casas and Molnar, 1987; Somoza, 1998). Subsequently, convergence rates decreased, with the current GPS-measured rate being less than half of that at ~6 cm/year (Angermann et al. 1999).

### 2.2 Bedrock Geology

The bedrock geology of the Coastal Cordillera near 25–26° S is largely comprised of Paleozoic rocks and the Late Jurassic/Early Cretaceous volcanic arc. Coastal areas are dominated by Paleozoic basement, including folded and faulted low-grade metamorphic rocks of the Chañaral Epimetamorphic Complex intruded by coarse-grained Permian granites of the Cifuncho Plutonic Complex (Contreras et al., 2013). The Paleozoic basement is intruded by Late Triassic to Early Cretaceous arc-related granitoids and overlain by Late Triassic to Early Cretaceous continental and marine sedimentary units and volcanics, including widespread deposits of the Jurassic La Negra Formation (Contreras et al., 2013; Escribano et al., 2013; Espinoza et al., 2014). Areas around the Atacama

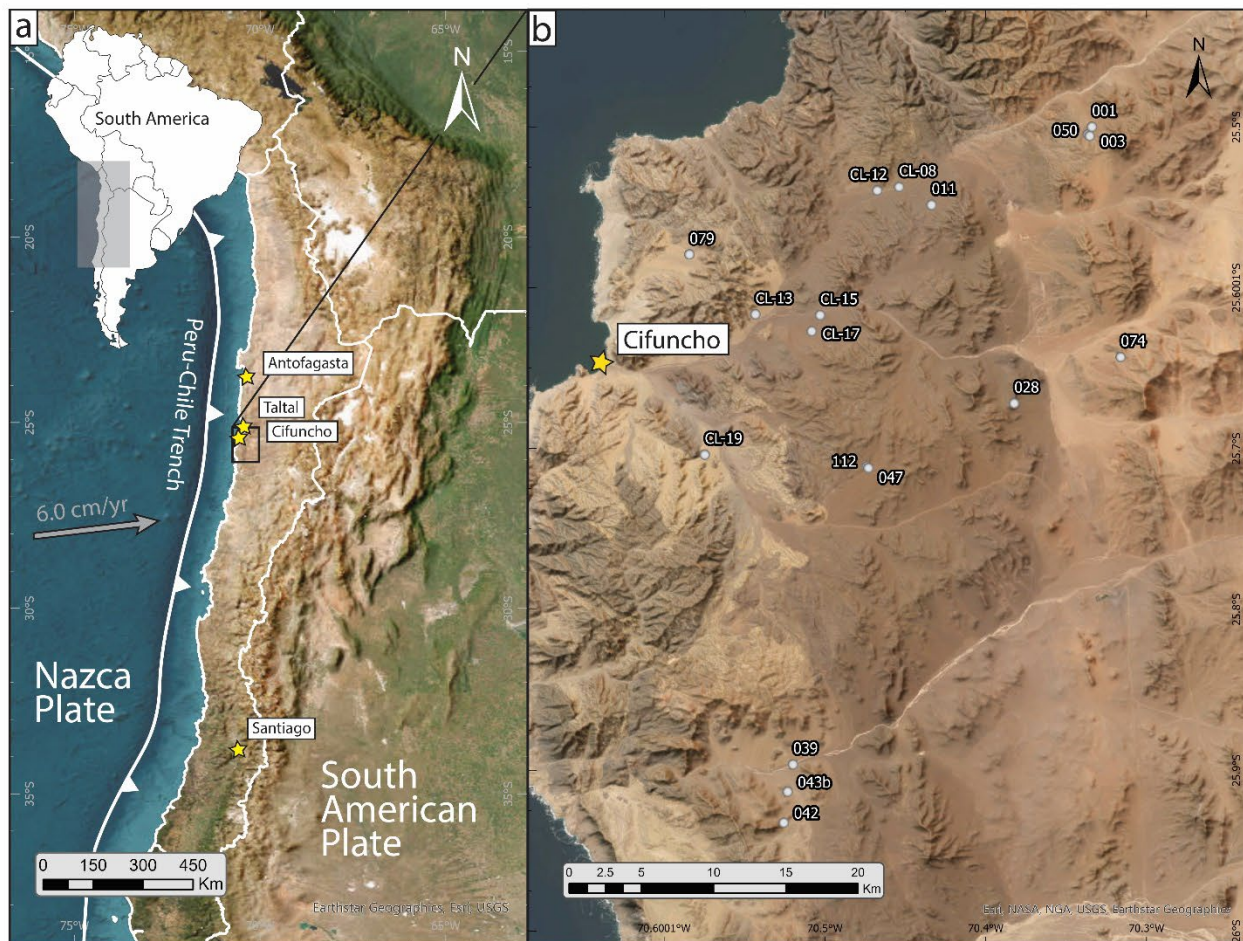


Figure 1. Base images from ESRI World Imagery basemap. a) Tectonic plate boundaries; present-day convergence vector (grey), from Angermann et al., 1999, Fig. 2, San Felix Islands station. b) Site locations referenced within text and figures, site names that begin with “CL” are abbreviated.

fault system are dominated by units composed of the Lower Jurassic/Early Cretaceous volcanic arc. The oldest rocks present to the east of the AFS are those of the Chañaral Epimetamorphic Complex, exposed either as “roof pendants” or tectonically-exhumed blocks (Espinoza et al., 2014). This complex is intruded by plutonic rocks of the Jurassic-Cretaceous batholith. Upper Cretaceous to Lower Miocene units are absent in this area, from which a depositional hiatus is inferred (Espinoza et al., 2014).

Four major Mesozoic bedrock fault systems dominate this part of the Coastal Cordillera: the Atacama fault system, the Taltal fault system, the Tigrillo fault system, and the Northwest fault system. The Atacama fault system (AFS) spans ~1,000 km along the Coastal Cordillera of northern Chile. The AFS near 25–26° S consists of roughly N-S striking subvertical fault strands that cumulatively record  $\sim 54 \pm 6$  km of ductile to brittle sinistral shear in the Early Cretaceous (~133–110 Ma; Seymour et al., 2020, 2021). Located just southeast of Taltal, the Taltal fault system is an NW-striking, subvertical fault system that cumulatively displaces the eastern strand of the Atacama fault system by ~11 km in a sinistral sense across a ~15 km wide area (Mavor et al., 2020). The Tigrillo fault extends from the coast between Taltal and Cifuncho to ~20 km south of Chañaral. It strikes approximately N-S, though it is more undulate compared to the neighboring AFS to the east. The Tigrillo fault system is primarily interpreted as an E-dipping normal fault system, separating Triassic to Middle Jurassic rocks from a series of plutonic complexes, that accommodated extension during the early stages of the Andean orogeny and was later locally reactivated by sinistral slip (Grocott and Taylor, 2002; Contreras et al., 2013). Though this area contains sets of both NE- and NW-striking faults, the NW-striking fault sets are the most prominent, including the Northwest fault system near Cifuncho (Contreras et al., 2013). These NW-striking faults are interpreted to record sinistral slip during the Middle to Late Jurassic (Contreras et al. 2013).

It is likely that both the Taltal fault system and the Northwest fault system reactivated older NW-striking weak zones, such as SW-vergent thrusts and associated thrust-related folds in the late Paleozoic basement (Fuentes et al., 2016; Mavor et al., 2020). Additionally, some bedrock units such as the Chañaral Epimetamorphic Complex and the Chañaral mélange possess a NW-SE-trending structural grain related to late Paleozoic, NE-directed subduction (Bell, 1982), which may serve as a precursor to the formation of NW-striking faults.

## 2.3 Geomorphology

### 2.3.1 *Geomorphology of the Coastal Cordillera*

Owing to the hyperaridity of the region, geomorphic features tend to be extremely well preserved in the Atacama Desert. The geomorphic features of the Coastal Cordillera change dramatically from west to east: from the true coastline, across the coastal scarp, crossing the mountain range and into the continental basin beyond. The coastline is dominated by a combination of wave-cut marine terraces and *rasas* (large, steep, coastal cliffs of marine origin, attributed to repeated sea level highstands superimposed on a slowly uplifting rocky coast; Regard et al., 2010). In my field area, deposits found on the modern coastline are primarily Pleistocene-Holocene eolian, marine, and coastal beach deposits (Contreras et al., 2013). Farther east of the coastline and penetrating the Coastal Cordillera mountain range are high fluvial terraces and a dissected pediment surface, thought to represent a “single continental planation surface” (Rodríguez et al., 2013). Abandoned fluvial channels form a network of valleys that cross-cut the mountain range, though flow of ephemeral channels is occasionally initiated by the region’s rare precipitation events. Adjacent to these lowland valleys are abundant, large alluvial fans, which most commonly coalesce into *bajadas*. In my field area, alluvial deposits range in age from Miocene to Holocene (e.g., Contreras et al., 2013; Espinoza et al., 2014). The Miocene Atacama Gravels (Mga) unconformably overlie the bedrock and are covered by Miocene-Pliocene alluvial deposits that locally fill channels carved into Mga (Contreras et al., 2013). Pleistocene-Holocene alluvial/colluvial deposits overlie these units (Contreras et al., 2013). Ages of alluvium in this region are not well constrained, but around my field area K-Ar and  $^{40}\text{Ar}/^{39}\text{Ar}$  biotite ages from ash layers in alluvial deposits range from ~12–4 Ma (Marinovic et al., 1995; Escribano et al., 2013; Álvarez et al., 2016). Farther in from the coastline, Pleistocene-Holocene (Quaternary) eolian, salic, and nitrate deposits can be found (Espinoza et al., 2014). Playa-type deposits are often present in decameter-scale, local shallow basins formed in alluvial deposits.

### 2.3.2 *Geomorphology of the Central Depression*

The Central Depression (CD) is bounded on its western side by the Atacama fault system and the Coastal Cordillera, and on its eastern flank by the Domeyko fault system, a major structure in the Chilean Precordillera (e.g., Arabasz, 1971; Audin et al., 2003). The CD was “endorheic,” or a closed basin, from the Upper Paleocene through the Pliocene with it becoming a primary drainage basin for water flowing from the east throughout the Neogene (Diaz et al., 1999; Sáez et al., 1999; Hartley and Chong, 2002; Audin et al., 2003). A dominant feature in this area is

the regional pediplain, interpreted to be a recently dissected feature that was once a single roughly continuous surface extending throughout the southern Atacama Desert (Audin et al., 2003). Arabasz (1971) describes this surface as a “low-relief surface,” characterized by deeply weathered rocks and veneered pediments. Between Taltal and Papos, an area covered by my study, this old topography is preserved ~10-20 km inland (Arabasz, 1971). Even individually faulted blocks show signs of inheritance of the pediplain surface, with highly weathered rocks still present on their upper surfaces (Arabasz, 1971). Major alluvial fan deposits are estimated to represent typical Pliocene and Quaternary deposits, derived from the Precordillera and attributed to the period of hyperaridity ~3–6 Ma (Hartley and Chong, 2002). Similar to the Coastal Cordillera, these alluvial deposits overlie the Atacama Gravels Formation (Audin et al., 2003). Cobbles dated from a relict fan surface in the Atacama Gravels in the Central Depression provide a model surface exposure age of 9 Ma (Nishiizumi et al., 2005). Established drainage networks cut into the Pliocene-Quaternary (Hartley and Chong, 2002) alluvial deposits, forming tectonic markers where their courses are deflected or disconnected.

Audin et al. (2003) discusses a lineament site where “nested” alluvial surfaces of different ages are dissected by an active drainage network. Interpreting lineaments as active tectonic fault scarps (“half-grabens”), they note that only the largest of the streams can cross an active scarp and re-join its channel downstream. Smaller streams result in ephemeral “sag ponds,” blocked at the base of the scarp (Audin et al., 2003). Further confounding the geomorphic signal is the observation that lineaments themselves form trenches, which likely channelize surface flow and enhance erosion.

## **2.4 Climate and Soil Chemistry**

The Atacama Desert is a zone of extreme hyperaridity, which influences geomorphic processes and the types of landforms preserved there. The core receives less than 3 mm of precipitation per year (Rech et al., 2006). Rare precipitation events can be extreme, often resulting in flooding and rapid incision. In areas closer to the coast, daily fog or *camanchaca* from the Pacific is the main source of water for animals and plants alike. Factors contributing to the hyperaridity include the Andean rain shadow, the area’s latitudinal position, and the coastal temperature inversion associated with the cold Humboldt ocean current (Houston and Hartley, 2003; Rech et al., 2006). As a result of the climate, surface deposits across the entire region are extremely well preserved.

Rech et al. (2006) identified four classes of paleosols preserved in the Calama Basin, a location northeast of this study's field area. Their study identifies middle-upper Miocene strata contain calcic vertisols and calcic argillisols, which in all locations sampled are overlain by a thick, well-developed gypsisol (Barros Arana geosol), and calcisols are present within Quaternary deposits and geomorphic surfaces. Their study also shows the Barros Arana geosol is a well-developed salic gypsisol that directly overlies Paleozoic volcanic bedrock and is also found within Miocene alluvial fan deposits. Most notably, this geosol contains large V-shaped salt fractures, or "sand dikes" which may be filled with eolian silts/sands and salts (Rech et al., 2006). Up to 35 cm across and 2 m deep, these features are "similar to fractures in modern Atacama salic soils" (Ericksen, 1981; Rech et al., 2006).

## 2.5 Seismicity

The seismogenic zone of the Nazca-South American plate system dips approximately 12–14° east (Allmendinger & González, 2010, Fig. 2) and extends down-dip to  $50 \pm 5$  km below the Coastal Cordillera in northern Chile (Husen et al., 1999, 2000; Buske et al., 2002). The plate boundary is largely or completely locked during the interseismic part of the seismic cycle (Bevis et al., 2001; Klotz et al., 2001; Allmendinger & González, 2010). InSAR and GPS data suggest a fully locked zone up to 35 km deep with a transition zone between 35–55 km depth (Chlieh et al., 2004). Khazaradze and Klotz (2003) suggest that the depth of the locked zone likely varies along strike. Individual segments of the margin are ruptured by great megathrust earthquakes on a recurrence interval of ~100–150 years (Comte and Pardo, 1991; Loveless et al., 2005).

Some geomorphic features in the Atacama have been attributed in part to the seismic cycle of the region, brought on by the locked convergent boundary (e.g., Audin et al., 2003; Loveless; 2005). Loveless et al. (2005) studied surface cracks in the Salar Grande region of the Atacama (~500 km north of my study's field area), noting that they were best preserved in "gypsum-indurated gravel" or "gypcrete." Their study showed these surface cracks cluster around fault scarps, with faults and cracks having similar orientations. Some cracks penetrate as far as 8–12 m into bedrock and are commonly parallel to bedrock joint sets (Loveless et al., 2005; 2009). Loveless et al. (2005) suggest that most cracks are mode I/opening, but some may be mixed-mode. Notably, they show there is a consistent preferred crack orientation normal to the direction of plate convergence. They conclude that most of these cracks record "approximate E-W extension associated with plate boundary processes such as interseismic loading,

coseismic and postseismic strain, and long-term instability resulting from subduction erosion” (Loveless et al., 2005).

Loveless et al. (2009, 2005) also propose that clusters of surface cracks show systematic orientation patterns that are spatially similar in scale to great earthquake rupture areas. They interpret layers of gypsum plated on crack walls as repeated cycles of sealing and reopening, potentially recording deformation old enough to reflect thousands of ~100-year earthquake cycles (Loveless et al., 2005). Loveless et al. (2009) calculated the coseismic principal deviatoric stress fields for four great earthquakes (M 8.0–8.5) on four different segments of the Andean margin: Arequipa (2001), Antofagasta (1995, Iquique (1877), and southern Peru (1868; International Seismic Centre, 2023). Based on these stress fields, Loveless et al. (2009) shows the orientations of modeled  $\sigma_1$  axes generally align with the mean strikes of nearby crack populations. Loveless et al. (2005, 2009) suggest there are characteristic segments of the tectonic margin that rupture in a cyclical pattern, citing the consistency of crack orientation with mapped geometries of the epicenters of great earthquakes. These studies outline how modeled  $\sigma_3$  axes tend to radiate from the center of the modeled epicenter ellipse, with cracks striking perpendicular to these axes (parallel to  $\sigma_1$ ). Our study is also an investigation of tectonic surface features, utilizing mapping of neotectonic alluvial lineaments to create a similar spatially-oriented dataset. We aim to measure their orientations, characterize their morphology, and define their structural features. With these data, we examine possible formation mechanisms for lineaments, and how they may be connected to the stress regime and the seismic cycle of the broader region.

### 3. METHODS

#### 3.1 Mapping Lineaments

Lineaments have a specific appearance in satellite imagery, possessing unique characteristics that I used to identify and map them directly from the images. They consist of sets of parallel ridges, most often two and rarely three or more. These features have a linear to curvilinear trend in map view, with individual ridges possessing a lenticular to oblong shape (Figure 2). These sets of ridges range in the tens of meters in width (measured ridge-to-ridge) and up to several kilometers in length. A single lineament feature may be comprised of a single, longitudinally-continuous set of ridges, or more often, a dissected array of individual segments. In satellite imagery, lineaments commonly display a distinct light/dark color pattern, with the ridges appearing darker than the surrounding alluvium. Often, light-colored playa-type deposits are present in local depressions inside the lineament troughs, which highlight the feature's geometry in satellite imagery. Lineaments with higher relief are typically more prominent, where favorable shading on individual ridges can help define ridge crests.

I mapped lineaments in ArcGIS Pro using ArcGIS Pro World Imagery basemap (Sources: Esri, DigitalGlobe, GeoEye, i-cubed, USDA FSA, USGS, AEX, Getmapping, Aerogrid, IGN, IGP, swisstopo, and the GIS User Community), assisted by Google Earth imagery. The mapping area is roughly rectangular, between 25.50–26.00°S and 70.30–70.65°W and covers ~2000 km<sup>2</sup>. Using the criteria outlined above, combined with field notes and digital elevation models (DEMs), I created a feature class of polylines where each polyline traces the crest of a lineament ridge. For straight segments, the line segment tool was sufficient. For curvilinear segments, I used the anchor point streaming tool, then smoothed the polyline as necessary (smoothing window 1–15 meters). The polylines belong to two different feature classes: Lineament\_Polylines\_Full and Lineaments\_EP. Lineaments\_EP contains all the sub-classifications of lineaments and lineament segments (the polylines are split in places) whereas Lineaments\_Polylines\_Full was used to generate statistics and contains continuous polylines.

Lineaments\_EP contains 4 unique attributes, which I used to categorize lineaments. The 'Confidence' field, ranging from 1–3, is a measure of data quality (1 being the highest quality). It considers factors such as certainty, establishing that the mapped feature is a neotectonic alluvial lineament and not some other linear desert landform or artifact of satellite imagery. It considers estimated accuracy in mapping and the quality of the site. Site quality can

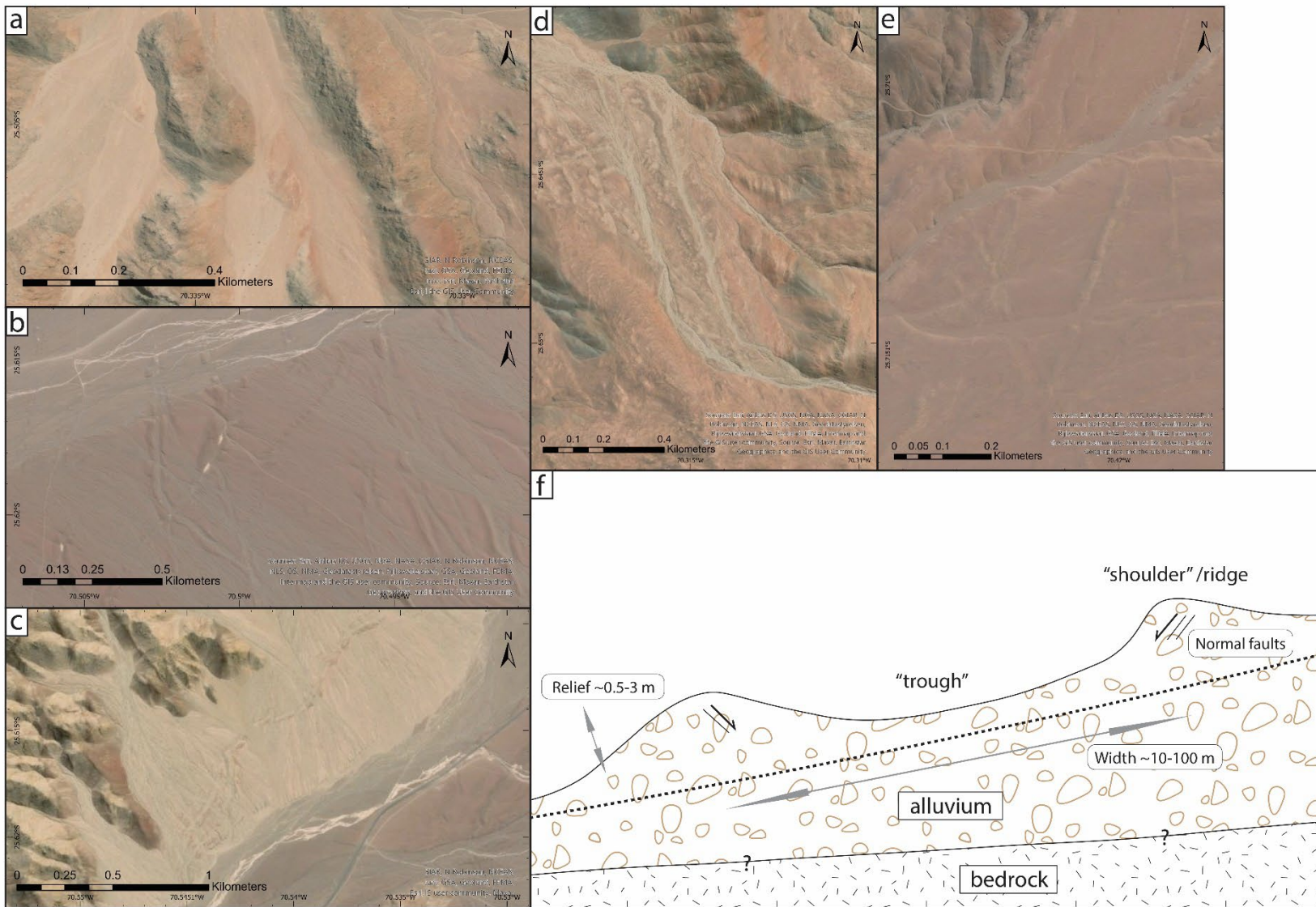


Figure 2. All photos from ESRI World Imagery basemap. a) Site 003; lineament traces over Quebrada Tipias fault, with fissures in central bedrock outcrop. b) Site CL-010520-15; lineaments cross alluvial surfaces of different relative age. c) Site CL-010520-13; curvilinear lineaments cross a bajada. d) Site 074; twin lineaments trace over the eastern branch of the AFS. e) Site 047; multiple lineaments to the south of a deeply incised drainage f) Cross-section diagram of primary features of a typical lineament crossing an alluvial fan (perpendicular to flow direction), dotted line approximates slope of fan.

be impacted by excessive modification by water, wind, or by humans (typically, roads). ‘Shoulder’ is a geometric designation used to display the polylines. Lineament segments are assigned a cardinal direction based on their estimated orientation from the center of the lineament trough. ‘Modified’ is another field used to display the polylines. A lineament segment receives a ‘C’ designation if it traces across a channel (10–50 m wide) and a ‘W’ if it crosses a wash (>50 m wide). Lineament segments crossing channels less than 10 m-wide are not differentiated, with a few rare exceptions. I used the ‘DEM’ field to mark when a lineament is present on one of the ten digital elevation models providing sparse coverage of the map area.

### **3.2 Sources of Error in Mapping Lineaments**

Much of my mapping is done exclusively using satellite imagery. As a result, instances of shadows, blurred images, and inconsistent color palettes can cause a degree of uncertainty in the mapping. A small amount of error may also be introduced while using the ArcGIS Pro smoothing tool on curvilinear ridge segments. In addition, we saw in the field how lineaments could be modified by water and human activity. These changes may not be easily identifiable from satellite imagery alone. Finally, this is the first dataset of its kind, and creating a consistent set of characteristics to map from can be challenging. A copy of the lineament map is available as a supplementary document to this thesis, including lineaments mapped by Emily Perman and Dr. Skyler Mavor (Map 1: Chapter 4 Alluvial Lineaments Map, Northern Atacama Desert, Chile).

### **3.3 Drone Imaging and Photogrammetry**

A DJI Phantom 3 drone was used (piloted by Dr. Rodrigo Gomila) to acquire images for a total of fifteen flights, resulting in ten 10-cm resolution digital DEMs and two outcrop photomosaics. I used a digital camera to obtain photographs for a third outcrop photomosaic. All digital elevation models and outcrop photomosaics were processed in Agisoft Metashape, using the workflow outlined in (Figure 3). DEMs and two accompanying drone photos for each site are available in Appendix A (Figures A1–A20).

### **3.4 Sources of Error in Photogrammetry**

The DEMs were not processed using ground control points, so their georeferencing is dependent on the drone GPS, which has an accuracy of 2–3 m. Agisoft executes error filtering of the initial point cloud, with the

# Creating Digital Elevation Models and Photomosaics in Agisoft Metashape

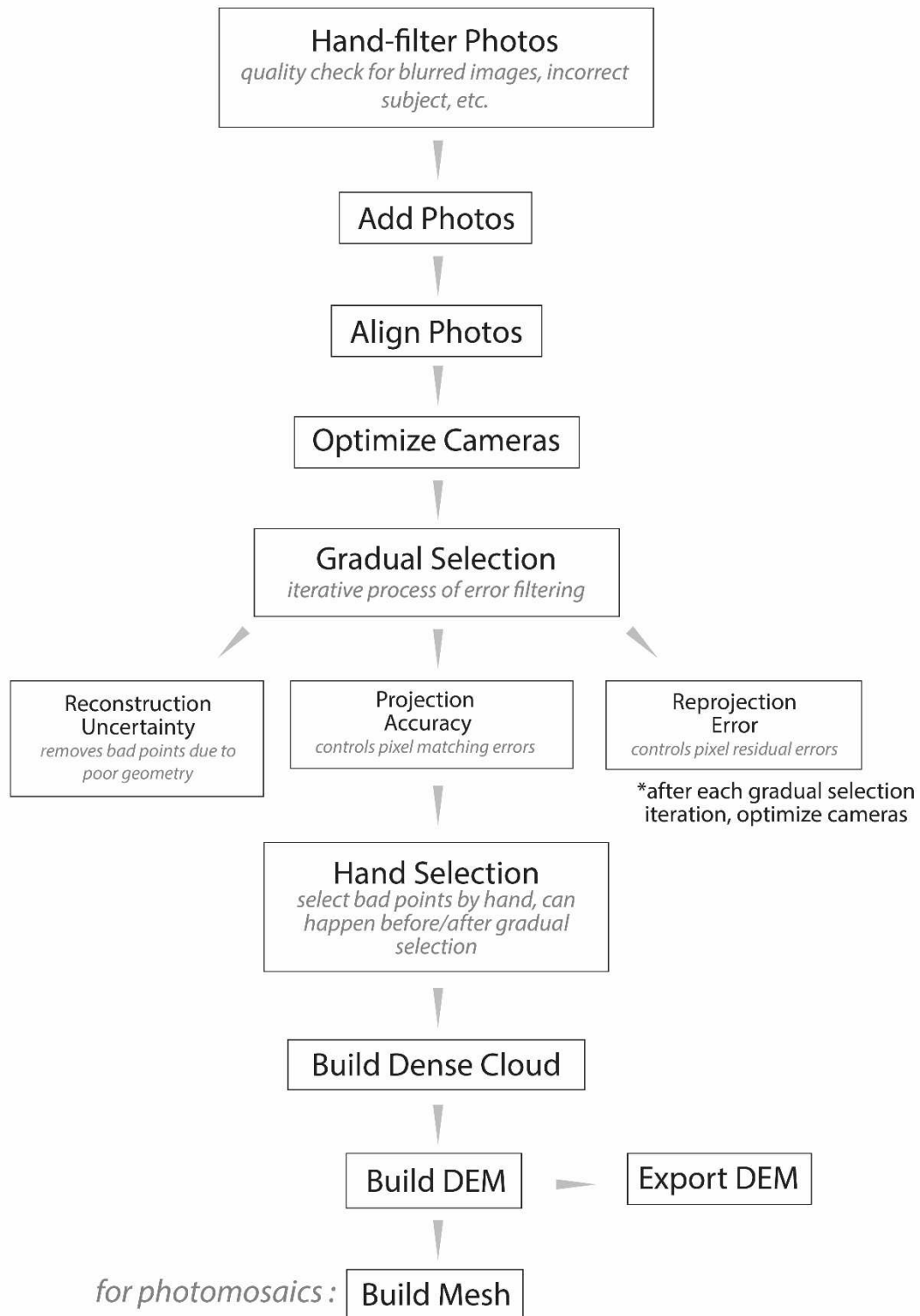


Figure 3. Workflow adapted from document 'Agisoft Photoscan Methods,' authored by Dan Scott.

metric for an acceptable error threshold is set by the user. A lower number of photographs typically means less accuracy, and in general, completed DEMs are noisier toward the outer edges where fewer photos exist and overlap.

### **3.5 DEM Analysis**

I further processed the raw geotiff files from Agisoft in ArcGIS Pro. I projected the geotiffs into UTM coordinates and used those files to create slope maps and hillshades. I used these shaded relief maps to assist with mapping lineaments in areas with DEM coverage. To extract elevation data from lineament sites, we used a combination of MATLAB scripts from TopoToolbox 2 (Schwangart and Scherler, 2014) and custom scripts. Specifically, I was interested in collecting elevation data from transects running perpendicular to lineament axes (“lineament profiles”). After cropping each DEM to a lineament segment of interest, I drew each lineament profile by hand, five profiles per segment spaced roughly equidistant. I drew each profile from west to east, starting from the southernmost extent of the cropped image and proceeding north. Each profile was then individually calibrated by handpicking five points: the outer edge of the west ridge, the crest of the west ridge, the center point of the trough, the crest of the east ridge, and the outer edge of the east ridge. I used the *plotregression* function from MATLAB (r.2020a) to fit a linear regression to a plot of mean lineament ridge height vs. trough width.

### **3.6 Lineament Orientations**

I produced rose diagrams of lineament orientations (trend) using both Polar Plots for ArcGIS (Jenness, 2017) and Allmendinger’s Stereonet 11. As lineament polylines are typically curvilinear, I used the ‘Shapes\_to\_Segments’ tool to convert single smooth polylines to sets comprised of multiple individual straight-line segments. Importantly, this inflates the number of data points used in this analysis, as opposed to calculating statistics using the unmodified polylines. Additionally, the polylines are not all of equal length. To account for this, calculations are weighted by polyline length, meaning that longer polylines have a greater weight than shorter ones. The circular histograms are binned by 5 degrees. I report the maximum value (the bin with the greatest number of data points), mean vector and circular variance from Stereonet 11. I also report the mean direction (approximately equivalent to mean vector), circular variance, angular variance, circular standard deviation, and angular deviation from the PolarPlots statistical tool.

### **3.7 Structural Data**

We (EP, JS, NS, SG) collected orientation data on faults found in well-consolidated, stratified alluvium using a combination of Brunton Geo Transits, Brunton Standard Transits and Allmendinger's Stereonet Mobile app on iPhone (Allmendinger et al., 2017). I compiled measurements of faults in lineament shoulders in Allmendinger's Stereonet 11 (Allmendinger et al., 2012; Cardozo and Allmendinger, 2013), computing the mean fault plane on east and west lineament shoulders separately based on the maximum eigenvector of poles to planes.

### **3.8 Alluvium Samples**

In the field, we collected four pairs of alluvium samples, each consisting of a sample from the faulted zone of alluvium in the channel wall and one immediately adjacent. We collected three pairs of samples from site CL-010520-19, and one set of samples from site 201-E47. In the lab, I applied epoxy to the friable samples before sending them out to be processed into thin sections. We first assessed the basic mineralogic and structural composition of the samples through a standard petrographic microscope. To further determine the composition of the cement present, I used a Terraspec handheld spectrometer. The Terraspec gives confidence levels (ranging from 1–3) for multiple mineral predictions in each sample, drawn from its VNIR/SWIR mineral library. To ensure complete coverage of each sample, I executed two collection runs on each sample, covering approximately half of the thin section with each run of the spectrometer.

### **3.9 Mapping Relative Age of Alluvial Surfaces**

To evaluate potential time-transient changes in lineament morphology, I mapped three distinct alluvial surfaces at site CL-010520-15 which are crossed by several prominent lineaments. I mapped these surfaces using satellite imagery, through surficial color as well as geometric relationships and areas of visible incision. The oldest surface of the three ( $Q_{a1}$ ) is distinguishable from the adjacent, younger  $Q_{a2}$  surface primarily by its darker, reddish hue, as well as through the small amount of incision visible in  $Q_{a2}$  channels running parallel to the main flow direction of the fan. The youngest surface ( $Q_{a3}$ ) truncates the two older surfaces, with its flow direction being effectively perpendicular to the previous two. It is lightest in color and has preserved deposits of ephemeral channels resulting from the region's most recent precipitation event.

### 3.10 U-Pb Geochronology

We collected a sample from an ash-fall tuff preserved within alluvial deposits from site CL-010520-08 (Figure A21). This tuff bed is 5.8 meters below the overlying alluvial fan surface and 3.2 meters above the surface of the modern channel (based on laser range finder measurements). Standard mineral separation procedures were performed to isolate zircon grains from the sample in the lab. After the sample was rinsed and sieved to a grain size of 300  $\mu\text{m}$ , I processed the sample through the vertical and inclined Frantz for magnetic separation. I then performed separation by density on the non-magnetic mineral separate using methyl iodide (MEI) to isolate the zircon grains.

Zircon U-Pb values were measured at the Plasma Analytical Facility at the University of California, Santa Cruz, using the laser-ablation inductively-coupled-plasma method (analysis conducted by Dr. Nikki Seymour). The primary standard used for this method is Temora-2, with secondaries FCZ, Duluth, Dromedary, and Plesovice. Individual spots were selected based on CL images, and zircon U-Pb data were evaluated for common Pb using a Terra-Wasserburg concordia diagram. Plots were generated by Dr. Nikki Seymour and Dr. John Singleton using IsoPlotR software (Vermeesch, 2018). The raw data are available as a supplementary Excel spreadsheet to this manuscript (Dataset 1: Chapter 4 Zircon U-Pb analytical data).

## 4. RESULTS

### 4.1 Lineament Occurrence and Morphology

As a distinct landform, lineaments consist of discontinuous sets of parallel alluvium ridges. Here, I call the ridges “shoulders,” with the central depression noted as the “trough” (Figure 2f). Lineaments are usually visible in aerial imagery at ~1:20,000 scale and smaller. Broadly, these features are linear in map view, but viewed in finer detail, most are curvilinear (Figure 2a-e). The lineaments vary from tens of meters to kilometers long and range between ~10–100 m wide from ridge to ridge. Maximum relief of the shoulders is around 3 m, but most range from 0.5–1 m tall (Figure 4). Lineament shoulder height typically appears asymmetrical for any given lineament, either from the sloping fan surface or by an actual difference in relief.

Lineaments cluster in alluvial fans and other alluvial deposits, appearing to both channelize water flow as well as cut laterally across active channels. Vegetation appears to preferentially grow down the center of some lineaments. In general, sediment size in the alluvial deposits ranges from coarse sand to gravel, with occasional cobbles and boulders. Coarser sediments are often found on the shoulders than in the corresponding trough, and the sediments in the trough and shoulders are often different colors (Figure 4b,d).

### 4.2 Lineaments and Bedrock

Lineaments sometimes directly overlie mapped bedrock faults, trending parallel to the fault strike, or line up with other bedrock structures like opening-mode cracks/fissures and dikes (Figure 5, Figure 6; Mavor, 2021, personal communication). These bedrock fractures are found in exposures adjacent to alluvial lineaments, with the trace of the fracture lining up with the lineament trough. Some of these fractures are identifiable as eroded fault cores, while others remain ambiguous, possibly a result of simple opening-mode cracks. They range from less than a meter to up to two meters in width. In some places where these fissures are identified as eroded fault cores, it is evident that the damage zone of the fault laterally extends much further. Occasionally, significant concentrations of calcite and gypsum are found within the rocks in these fissure/fracture zones. Alluvial lineaments are present along most of the N-S striking Atacama fault system, and along segments of the NW-striking Taltal fault system (Figure 7). Some lineaments extend along strike and connect separate fault segments across alluvial deposits (Figure 7c). A

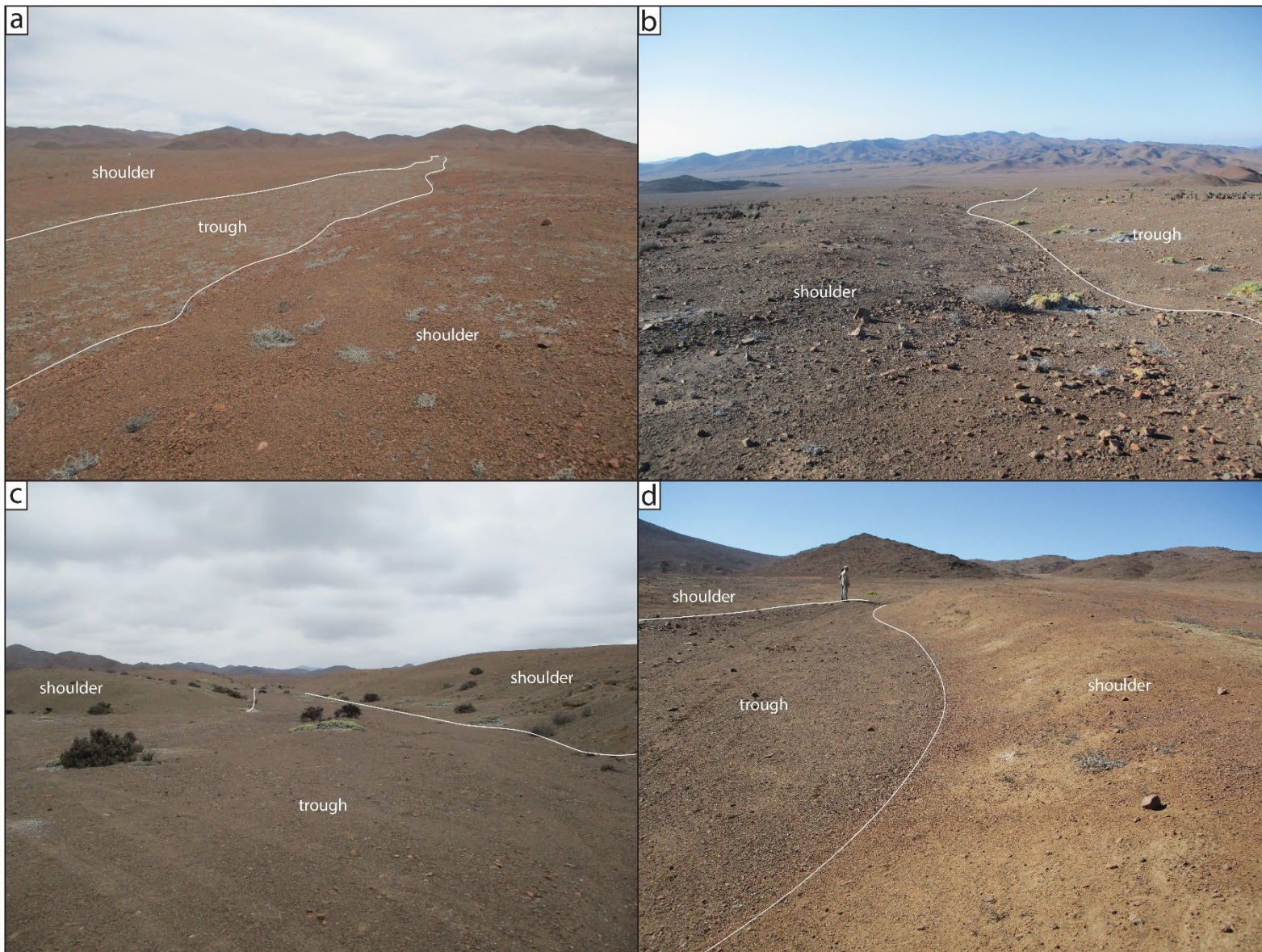
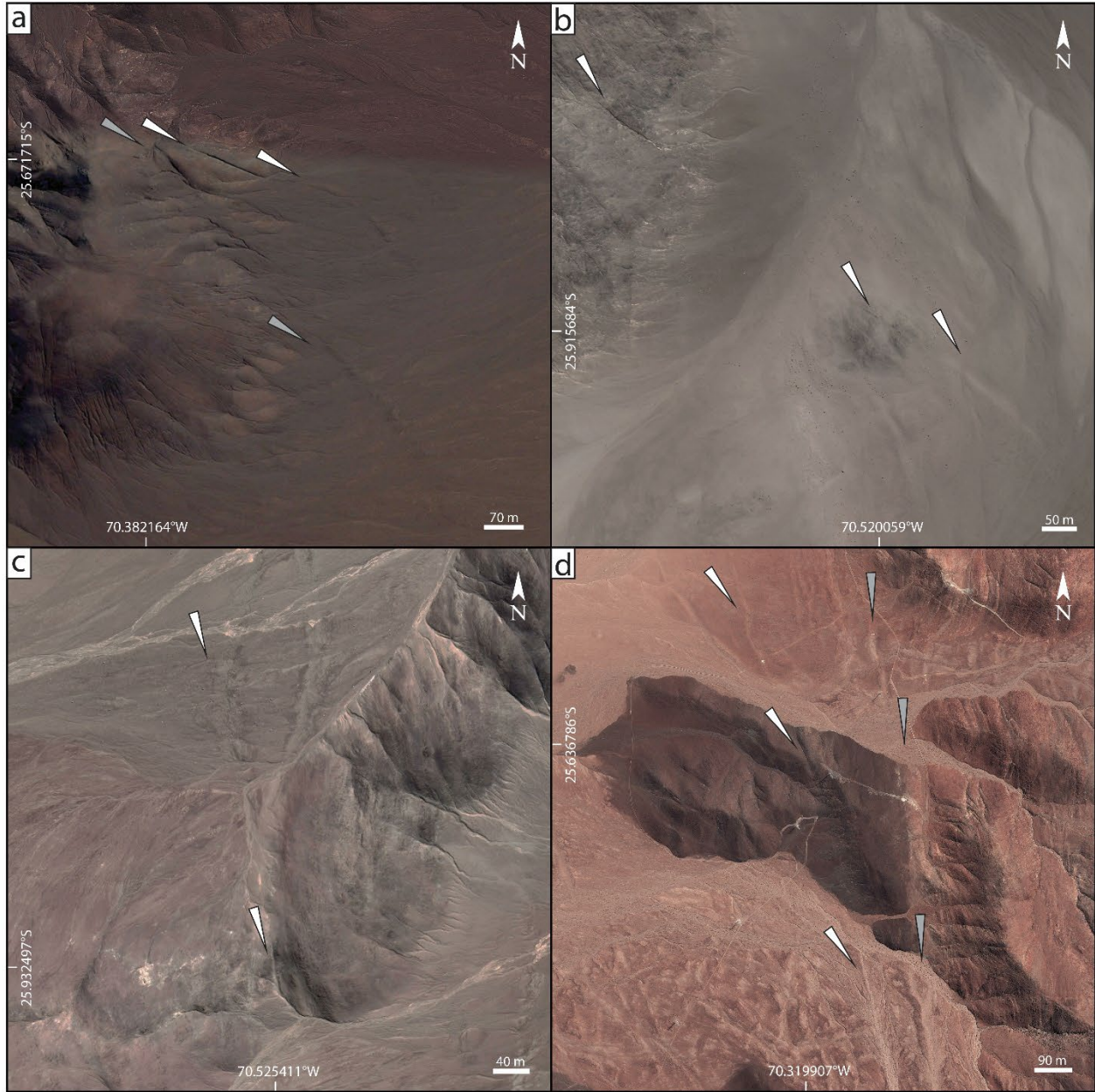


Figure 4. a) Site CL-010520-15; broad, low-relief lineament. b) Site 011; asymmetrical lineament missing one shoulder. c) Site CL-010520-12; lineament intersecting a drainage. d) Site 001; curvilinear lineament, relief between 0.5 - 1 m.





*Figure 6.* a) Site 028; two sets of fissures and lineaments, one set oriented WNW (grey arrows), one set oriented NW (white arrows); Google (n.d.-a). b) Site 043b; two fissures line up with one lineament, oriented NW; Google (n.d.-b) c) Site 042; fissure and lineament set, oriented NNW; Google (n.d.-c) d) Site 074; along trace of the E strand of the Atacama fault, two sets of lineaments and bedrock faults, one set oriented NNW (white arrows) and one set oriented approx. N (grey arrows); Google (n.d.-d)

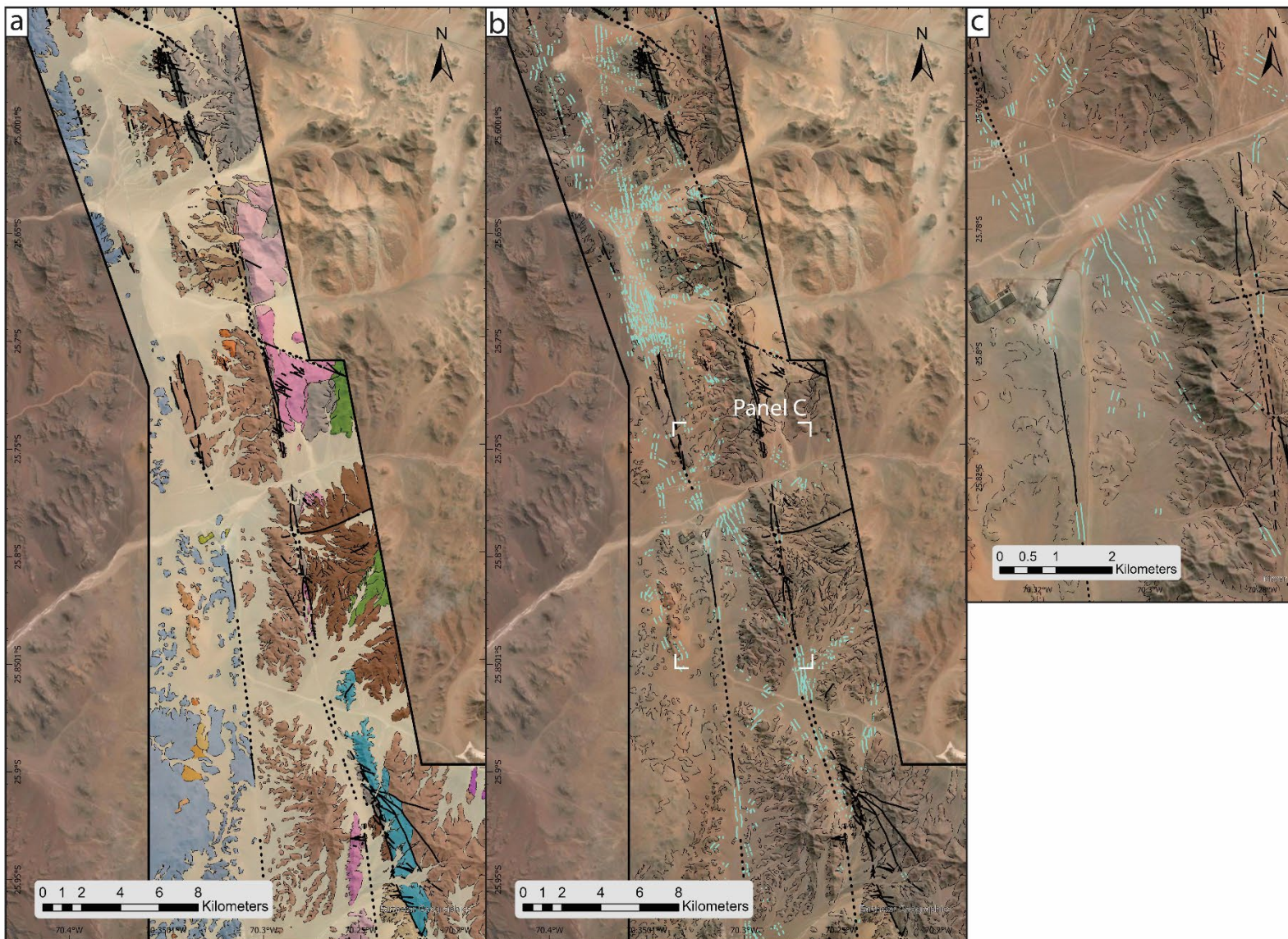


Figure 7. a) Bedrock mapping along the Atacama Fault System, Quaternary deposits shown in tan, major bedrock faults in bold. Modified from Mavor (2021). For explanation of bedrock geology, see publication. b) Lineaments (blue lines) mapped by Skyler Mavor overlaid with bedrock faults (bold black lines). c) In map view, lineaments often extend directly along strike from nearby bedrock faults and connect individual fault strands.

small number of lineaments trace parallel to a population of NW-striking dikes located around sites CL-13 and CL-15 (Mavor, 2021, personal communication).

### **4.3 Lineament Orientation**

Lineaments exhibit a wide range of orientations, with the largest population trending NNW (Figure 8, Figure 9). In this study, I utilized both my own data and those collected by Dr. Skyler Mavor, whose lineament mapping was tightly focused along the AFS as a part of a 1:20,000 mapping effort along a 70 km segment of the fault system (Mavor, 2021). In both lineament datasets, the maximum value, or largest bin, falls between values of  $171^\circ$  and  $180^\circ$  (equivalent to between  $351^\circ$  and  $0^\circ$ ; Figure 8b,c, Table 1). These datasets have similar mean vectors,  $173^\circ \pm 00.5^\circ$  ( $353.2^\circ \pm 00.9^\circ$ ) and  $170.2^\circ \pm 19.2^\circ$  ( $350.2^\circ \pm 19.2^\circ$ ; Figure 9, Table 1), and similar mean direction (Table 2). Typically, large clusters of lineaments will be more or less parallel to one another, though rarely can lineaments be seen crossing each other at a nearly  $90^\circ$  intersection (Figure 2b,e).

### **4.4 Lineament Height, Width, and Relative Age**

From satellite and field observations, we noted that the width and height of lineaments varies. Generally, wider lineaments have taller ridges, and my analysis of the lineament profile data collected from the DEMs shows that there is a weak linear correlation between lineament trough width and ridge height with an adjusted  $r^2$  value of 0.39, and RMSE = 0.62 (Figure 10). In several locations, I observed lineament width and height change with the relative age of different alluvial surfaces (Figure 11,12). Drawing profiles through the different surfaces show a marked difference in the relief of lineament ridges. The lineament profiles with the greatest relief in Figure 12a,b are the red profiles (1,2) drawn through the oldest alluvium,  $Qa_1$ . The red profiles (8,9,12) in Figure 12c,d are also drawn through  $Qa_1$  and exhibit the greatest relief relative to other profiles. Lower relief lineament profiles are present in the  $Qa_2$  surface, green (4,5) in Figure 12a,b and green (7) in Figure 12c,d. Profile 4 in Fig.12a,b shows a high-relief ridge on its western side, but this is due to the profile transecting a relict  $Qa_1$  surface. There is little to no lineament expression shown by the DEM in the youngest surface ( $Qa_3$ ), shown by the blue (3,6) profiles in Fig. 12a,b and the blue (10,11,13) profiles in Fig. 12c,d. However, the portions of the lineaments that cross  $Qa_3$  are still visible in satellite and aerial/drone images. The differences in relief are visible in aerial images as well, especially in the cutbanks of the  $Qa_1$  surface (Figure 13). These observations suggest that older alluvial surfaces tend to have wider and taller lineaments than adjacent younger ones.

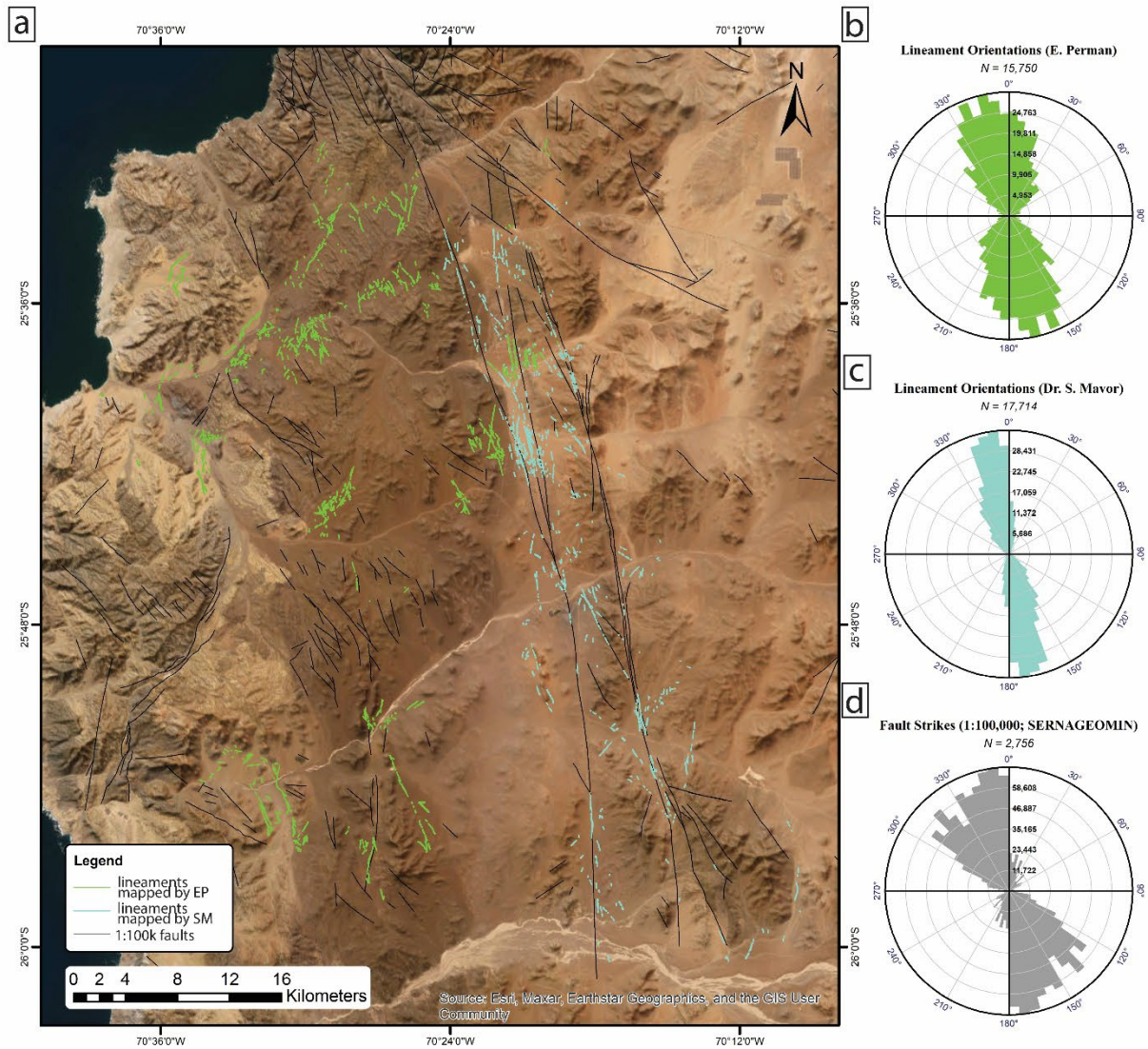


**Figure 8.** a) Field area extent with lineaments mapped by Emily Perman (green; mapping focused around 2020 field stations) and Dr. Skyler Mavor (blue; mapping focused along AFS). *Note:* more lineaments are present in this field area than are mapped here, and lineaments are also found further east into the Precordillera, concentrated in alluvial deposits b) Rose diagram (circular histogram) of lineament orientations (bins of 5°) mapped by Emily Perman. c) Rose diagram (circular histogram) of lineament orientations (bins of 5°) mapped by Dr. Skyler Mavor. d) Rose diagram (circular histogram) of strikes of bedrock faults mapped by SERNAGEOMIN; 1:100,000 scale. Diagrams auto-scaled to fill equal area, and segments are weighted by polyline length.

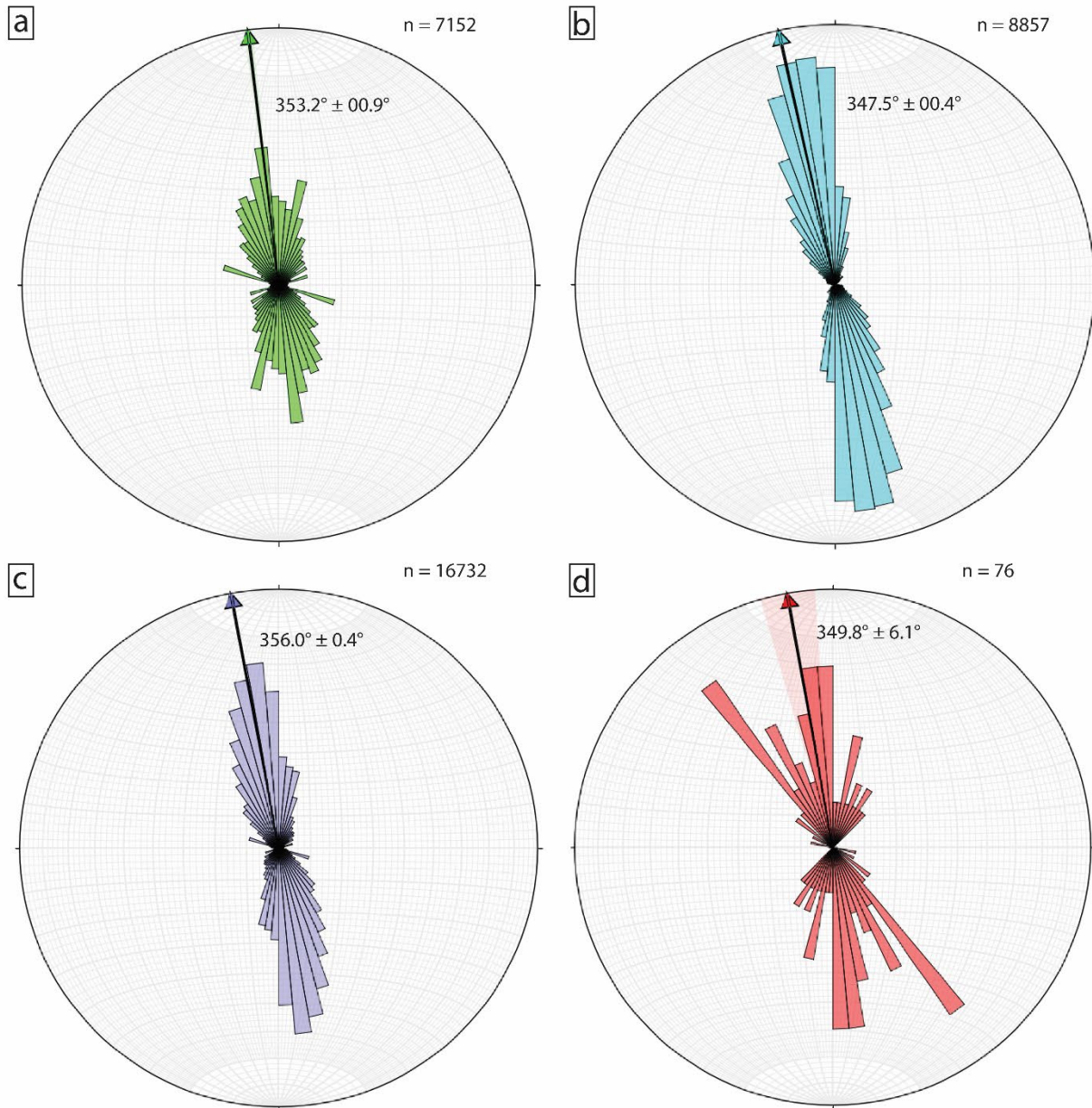


*Figure 9.* a) Rose diagram of lineament trends (circular histogram, bins of 5°) mapped by Emily Perman; n is number of converted polyline segments (any length). b) Rose diagram of lineament trends (circular histogram, bins of 5°) mapped by Dr. Skyler Mavor; n is number of converted polyline segments (any length). c) Data from 'a' and 'b' combined. d) Rose diagram of fault strikes (circular histogram, bins of 5°); small-scale faults collected in alluvium in cross-sections of lineament shoulders; n is number of faults. Mean vector plotted as arrows, shading around arrow is proportional to error in mean vector value. All diagrams scaled equally (15% of perimeter). Diagrams generated in Stereonet 11 (Allmendinger et al., 2012; Cardozo and Allmendinger, 2013), not weighted by segment length.

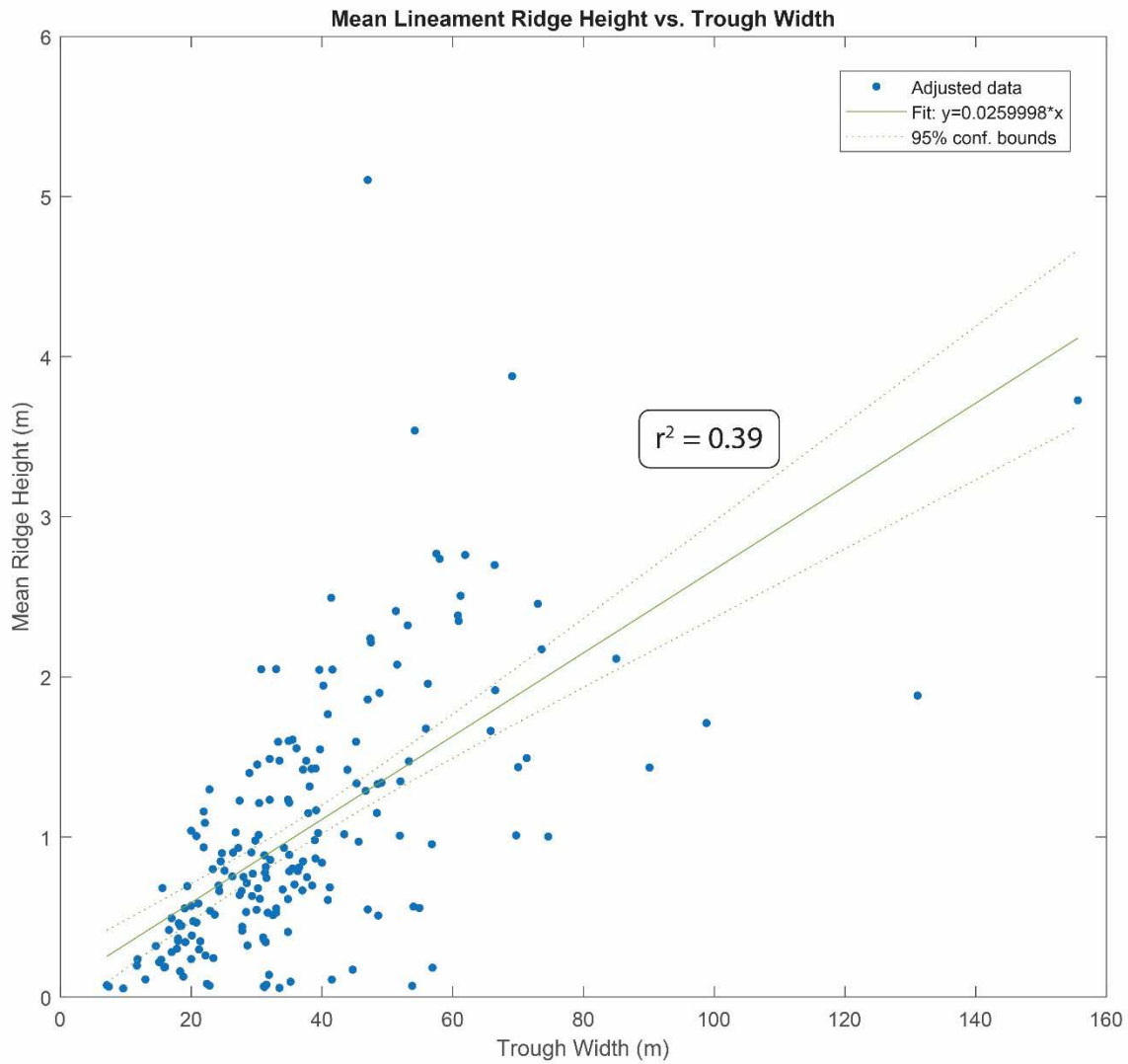


Figure 10. Linear regression model fit to plot of mean lineament ridge height vs. trough width, from all measured lineament profiles. Trough width defined as the distance between the center point of each ridge. Mean ridge height is the mean of the maximum and minimum ridge heights, measured as the relief between the bottom of the trough and the high point of each ridge on slope-detrended profiles. Adjusted  $r^2 = 0.39$  and RMSE = 0.62. Plot generated in MATLAB (r.2020a) using the *plotregression* function.

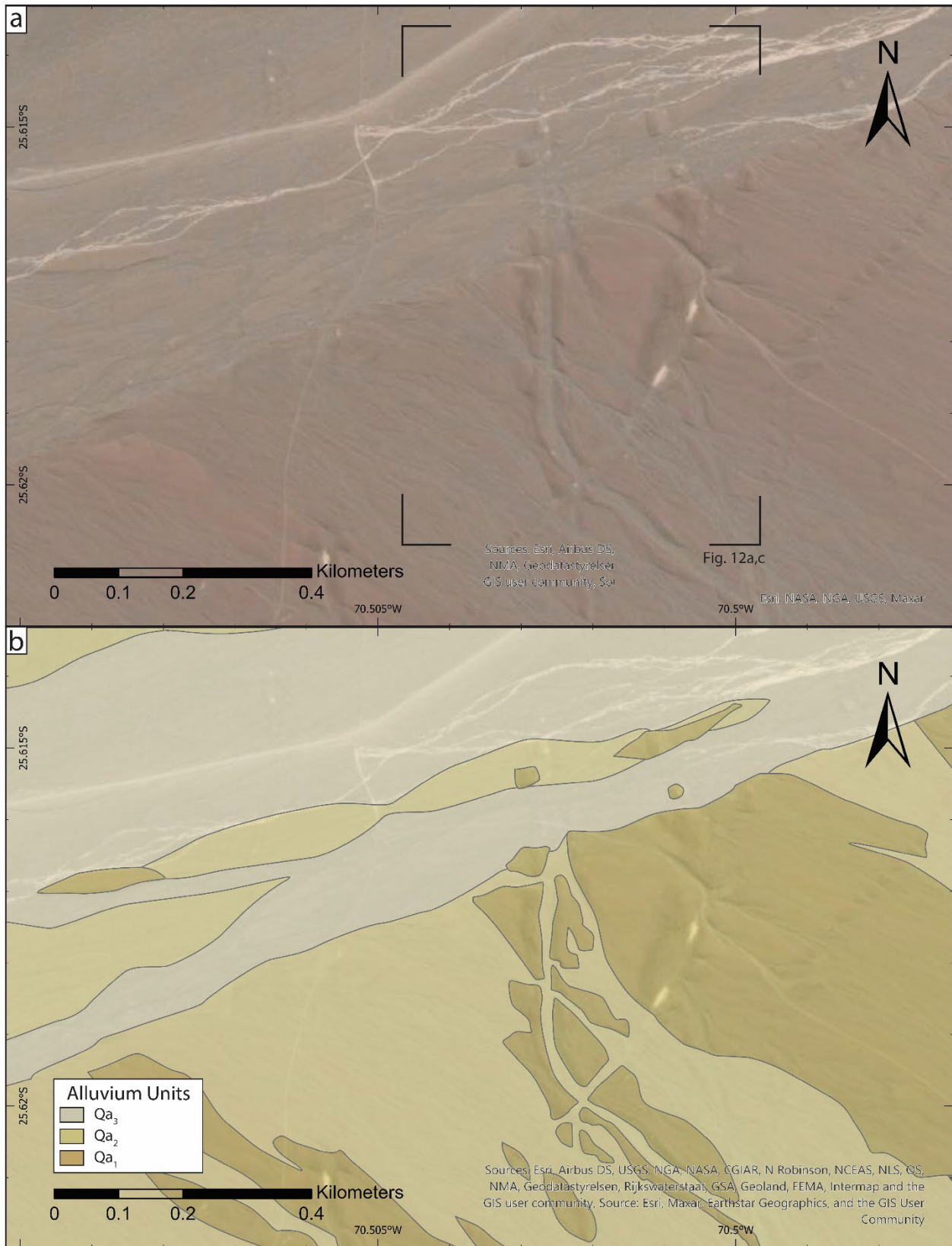


Figure 11. a) Satellite image of site CL-010520-15 (ArcPro World Imagery) containing two lineaments crossing. b) Lineaments cross three alluvial surfaces of relative age (Qa<sub>3</sub> - lightest, Qa<sub>1</sub> - darkest).

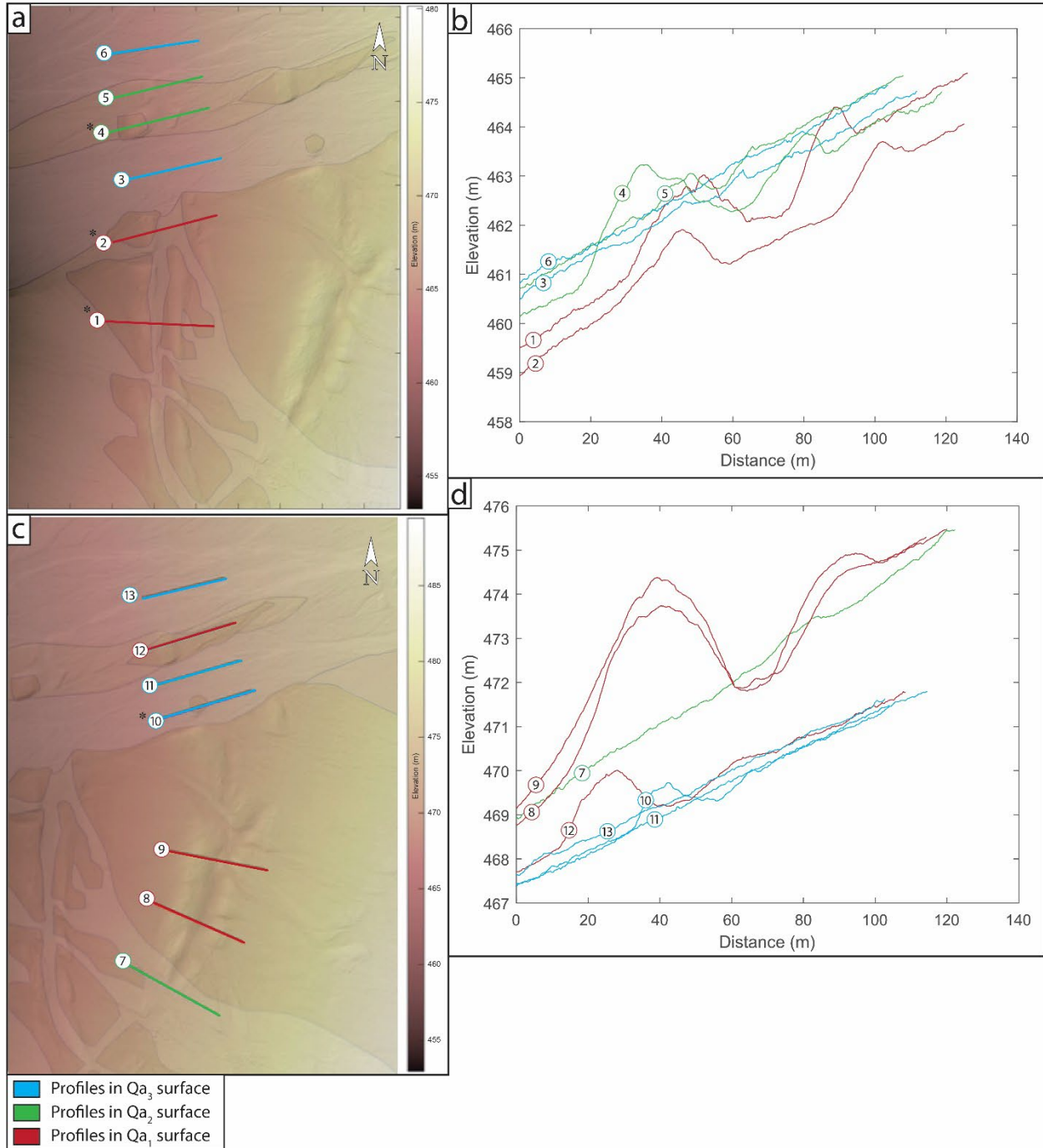


Figure 12. \*some profiles cross multiple surfaces, see mapping in Fig. 11  
 a) Series of profiles drawn perpendicular (W-E) to lineament trough through western lineament. b) Unsmoothed lineament profiles (elevation vs. distance from west-most point). c) Series of profiles drawn perpendicular (W-E) to lineament trough through eastern lineament. d) Unsmoothed lineament profiles (elevation vs. distance from west-most point). Plots generated in MATLAB (see methods, above).

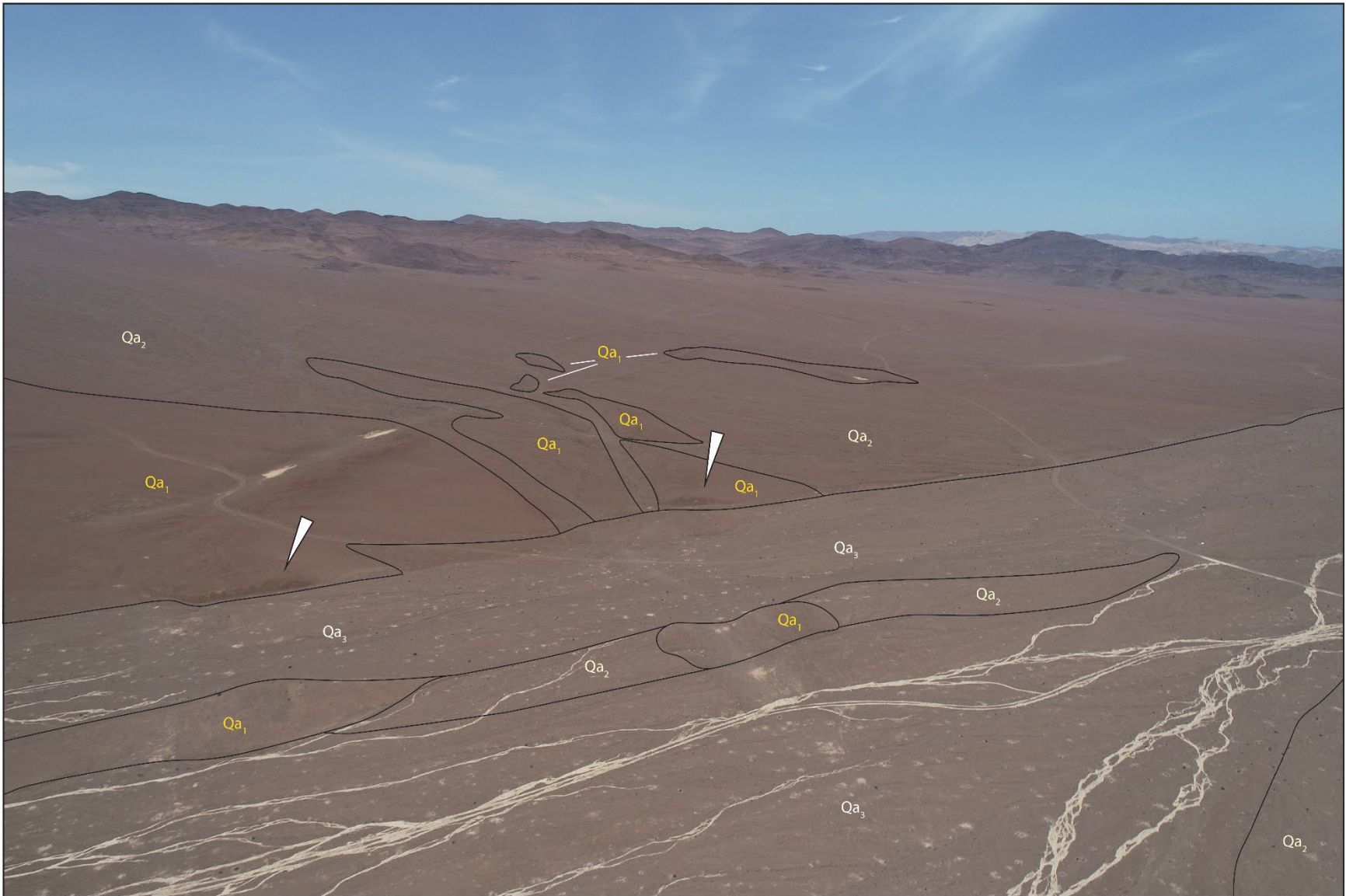


Figure 13. Drone photo looking south on site CL-0105210-15, with labeled alluvium surfaces of different relative age. Qa<sub>3</sub> truncates the older two surfaces and contains light-colored stream deposits from most recent precipitation event. Qa<sub>1</sub> stands out as much darker than the adjoining, younger Qa<sub>2</sub>. Lineament shoulders exposed in cross-section by channel incision (arrows).

Table 1. Circular statistics generated from Stereonet 11 (Allmendinger et al., 2012; Cardozo and Allmendinger, 2013). ‘Segments\_EP’ is converted polyline dataset from lineaments mapped by Emily Perman, ‘Segments\_SM’ is converted polyline dataset from lineaments mapped by Dr. Skyler Mavor.

	Lineament Trends (n = 7152) (Segments_EP)	Lineament Trends (n = 8857) (Segments_SM)	Lineament Trends (n=16732) Segments_EP and Segments_SM combined	Fault Strikes (Small normal faults within lineaments) (n = 76)
Max value	8.1% between 171° and 175°	13.1% between 171° and 175°	13.0% between 171° and 180°	11.8% between 141° and 145°
Mean vector	173.2° ± 0.5° (353.2° ± 0.5°)	167.5 ° ± 0.4° (347.5° ± 0.4°)	176.0° ± 0.8° (356.0 ± 0.8°)	349.8° ± 6.1°
Circular variance	0.541	0.211	0.611	0.341

Table 2. Circular statistics generated from PolarPlots for ArcGis (Jenness, 2014). ‘Segments\_EP’ is converted polyline dataset from lineaments mapped by Emily Perman, ‘Segments\_SM’ is converted polyline dataset from lineaments mapped by Dr. Skyler Mavor.

	Segments_EP (n = 7875)	Segments_SM (n = 8857)
Mean Direction	173.8° (353.8°)	171.7° (351.7°)
Circular Variance	0.159	0.959
Angular Variance	0.318	1.918
Circular Standard Deviation	33.7°	145.0°
Angular Deviation	32.3°	79.4°

#### 4.5 Cross-Section Exposures of Lineaments

Most cross-section exposures of lineaments described by this study are natural incisions found in stream channels (Figure 14). A few are artificial in nature, either trenches dug by hand or via excavator. In these cross-section exposures, we observed planar structures up to a few meters long and up to several centimeters wide, commonly enhanced by preferential erosion (Figure 15). In well-stratified alluvium, these structures record mm to cm-scale apparent normal-sense offset, and clasts within the zones are sometimes rotated into parallelism with the planes. These planes almost exclusively dip toward the trough. In one locality (CL-010520-19) with two faint lineaments, we observed a drag fold indicating apparent normal-sense slip with offsets of ~2 cm (Figure 15e), and in 5 locations within lineament cross-sections, we observed down-dip slickenlines on these planes. At site 047, a fault with m-scale apparent normal offset is visible in the underlying bedrock dipping towards the trough, and it falls along the trend of the lineament in the alluvial fan immediately to the south (Figure 16).

Trenching a lineament at site 050 by hand revealed a structure on the periphery of the lineament shoulder that resembles a thrust fault (Figure 17). This structure consists of gently folded, well-bedded alluvium. The lower bed is truncated by the upper by a planar contact, which dips gently to the southwest (apparent dip ~15-20°) towards the center of the trough. As the trench is oriented 90° to the lineament trend, it parallels the flow direction of the fan channels. A similar structure is found in a different trench at site 039 (Figure 18). In this exposure, the alluvium is not as well bedded compared to site 050, and there is no visible folding. This structure consists of two resistant beds, again with the lower bed truncated by the lower by a planar contact. The contact dips gently to the west (apparent dip ~20°) towards the center of the trough. Importantly, the apparent reverse-sense offset visible in these two trenches is not as evident as the apparent normal-sense offset seen more commonly in more steeply-dipping faults.

We measured 76 faults from 11 different lineaments, categorized by west and east shoulder depending on where they were recorded with respect to the lineament trough (Figure 19). The mean fault plane for the western shoulder is 342, 61 E, and the mean fault plane for the eastern shoulder is 174, 61 W. The mean vector of measured fault strikes on a rose diagram is  $350^\circ \pm 6^\circ$ , and the maximum value or largest bin (11.8%) is between  $141^\circ$  and  $145^\circ$ , with the second-largest bins  $171^\circ$  to  $175^\circ$  and  $176^\circ$  and  $180^\circ$  (Figure 9d, Table 1). These faults range in dip from ~45-75° with some outliers. These fault populations roughly parallel the overlying lineaments from which they were collected (Figure 19b)

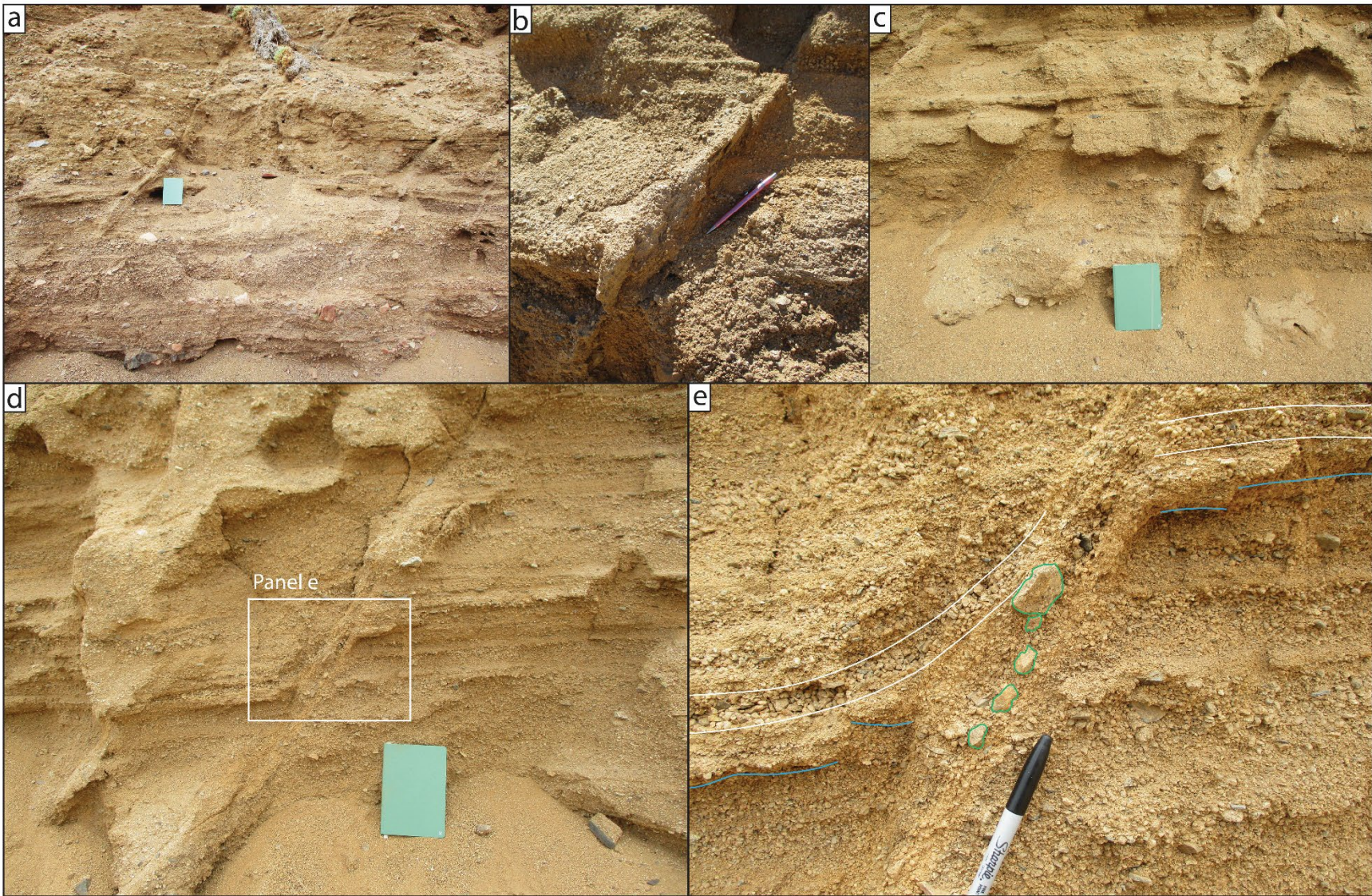


Figure 15. Panels a-d) Fault zones enhanced by preferential erosion, exposed in channel cut. All photos taken at site CL-010520-19 (Figure 13). e) Preserved drag fold with normal-sense offset of several centimeters and rotated grains. White: coarse-grained deformed layer; blue: underside of resistant, deformed layer; green: rotated grains.



Figure 16. a) Site 047; exposure of bedrock fault with apparent normal-sense offset in lineament shoulder and trough, dipping towards trough, exposed in channel cut. b) Location of photo (tip of arrow), view facing southeast along lineament trend (hillshade from DEM; 10 cm resolution).

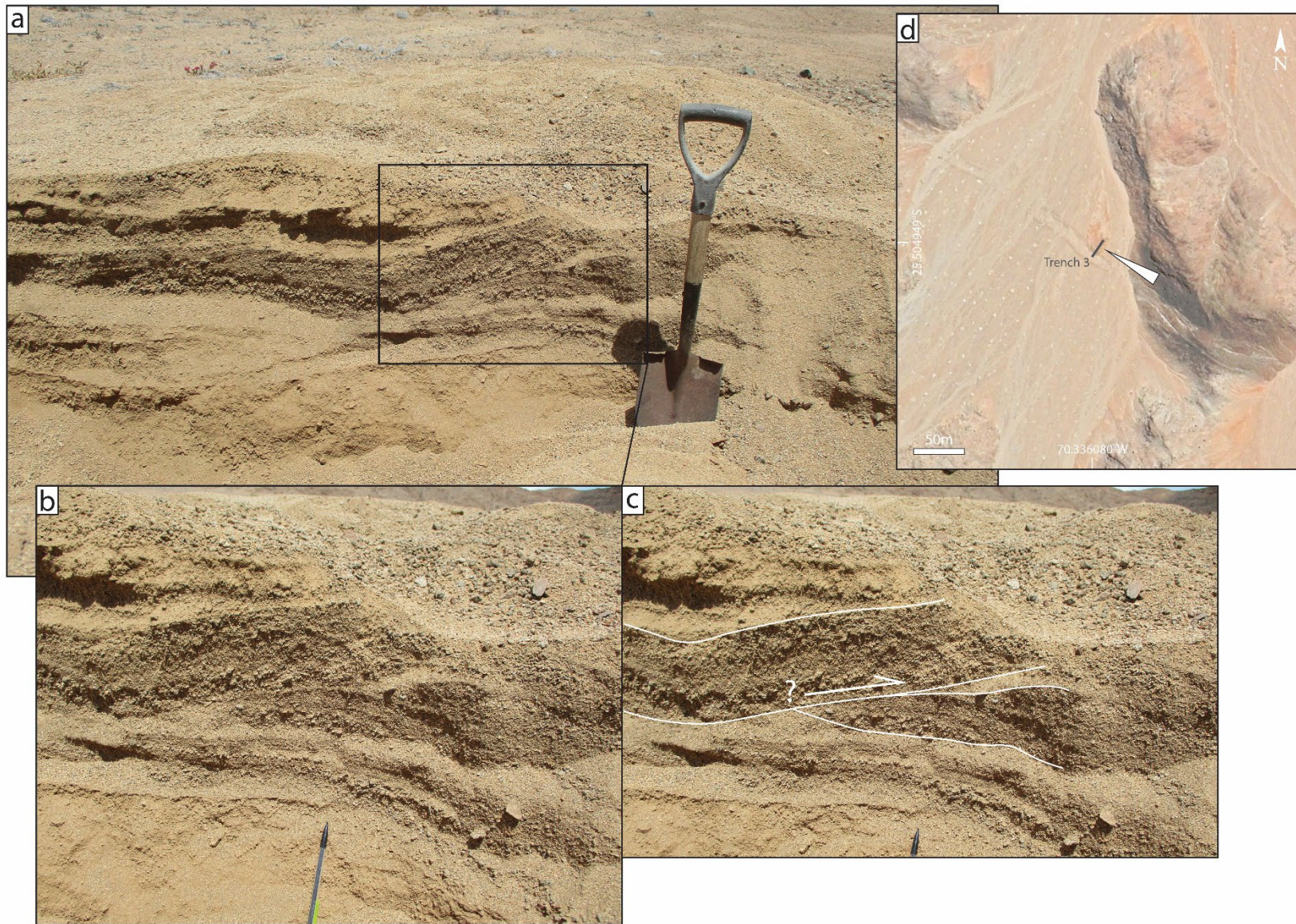


Figure 17. a) Site 050; trench through lineament shoulder (view looking northwest, tip of arrow is approx. photo location), with deformed bedding. b) Closeup of truncated beds. c) Possible thrust fault recorded in deformed bedding. d) Location of trench, dug perpendicular to lineament trend; Google (n.d.-f).

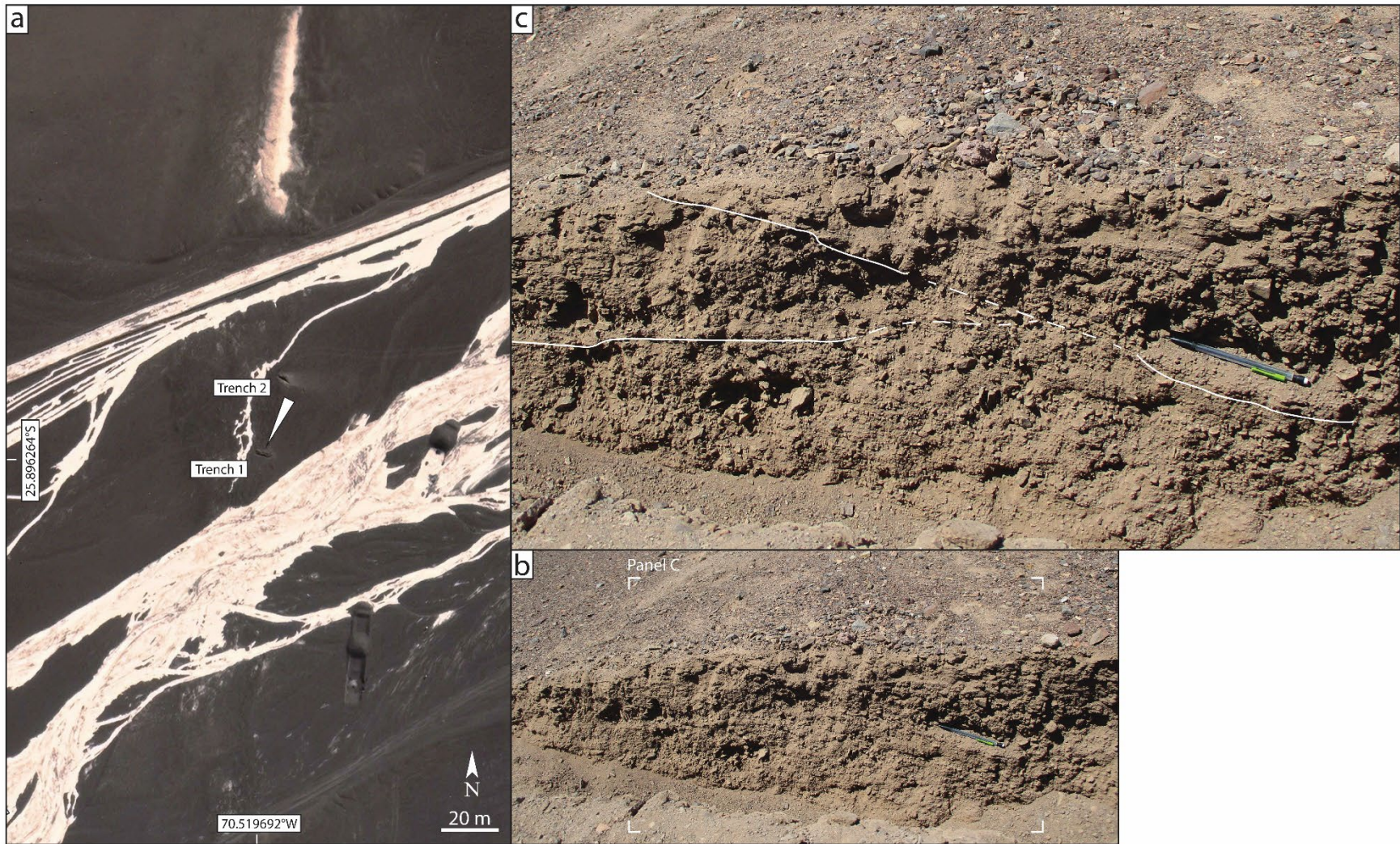


Figure 18. a) Site 039; location of trench, dug perpendicular to lineament trend; Google (n.d.-e). Tip of arrow is approx. photo location for other panels. b) Trench 1, view looking southwest. c) Deformed bedding in Trench 1. White lines contour bottom of resistant beds, dashed where approximate.

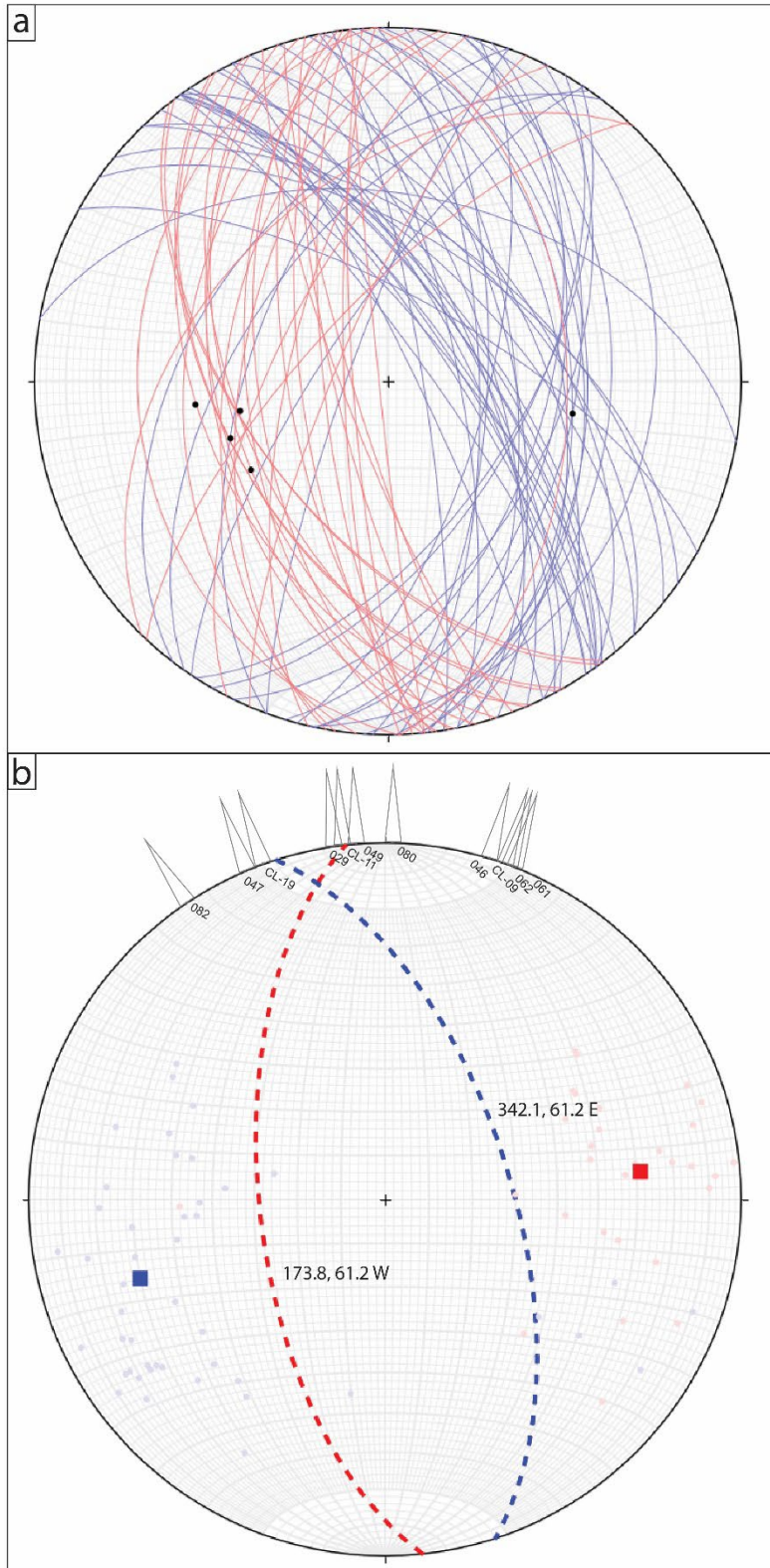


Figure 19. a) Faults collected in consolidated alluvium along cross-section exposures of lineaments. Faults collected in western shoulder are blue and those from the eastern shoulder are red. Slickenlines plotted as black circles. b) Mean fault plane for each dataset plotted as thick dashed line (plane to max eigenvector). Maximum eigenvector for each dataset plotted as filled square. Thin triangles represent average lineament orientations for all eleven lineaments where faults were measured in cross-section.

We sampled the faulted zones and corresponding nearby non-faulted sediment to compare microstructures and possible differences in mineralization or cementation at site CL-010520-19. The fault zones are often more resistant to erosion, displaying positive relief in the exposed channel cut, which may suggest they are preferentially more cemented than the surrounding alluvium (Figure 15). Samples CL-010520-19(a-f) come from a locality with numerous small-scale faults exposed in a drainage below weakly-developed lineaments. In this area, the alluvium is derived almost entirely from the local granitic bedrock. In thin section, there is some evidence of cement present around grain boundaries and in fractures penetrating grain boundaries (Figure 20). Several minerals are present in the cement (Table 3). Ferrihydrite is present in all samples, a hydrous ferric oxyhydroxide mineral. Clays are also present, with both rectorite and palygorskite found variably throughout the samples. The cement of samples 201-E47ab has a similar composition, though it has a different parent bedrock than all the samples. The alluvium from the faulted zones does not appear to record a higher degree of fracturing compared to the non-faulted alluvium, though the cement seems to be associated with fracturing in these samples as it fills fractures that cut across clasts.

#### **4.6 U-Pb Geochronology**

The zircons extracted from the ash-fall tuff sample (n=51) have a near-normal age distribution on a kernel density estimate plot, with a small prominence toward the older ages (Figure 21b). The weighted mean age of this population is  $2.489 \pm 0.015$  Ma, though this age distribution is right-skewed with a pronounced old tail that ranges from  $\sim 2.6$  Ma up to  $\sim 4.0$  Ma (Figure 21a,b). Several of the ages, including some from the older “tail”, plot off the Tera-Wasserburg concordia in a linear array, suggesting some of the zircons have a component of common Pb. Accordingly, we report the age of the tuff as the lower concordia intercept on the Tera-Wasserburg diagram:  $2.2 \pm 0.1$  Ma (Figure 21c). The raw data are available as a supplementary Excel spreadsheet to this manuscript (Dataset 1: Chapter 4 Zircon U-Pb analytical data).

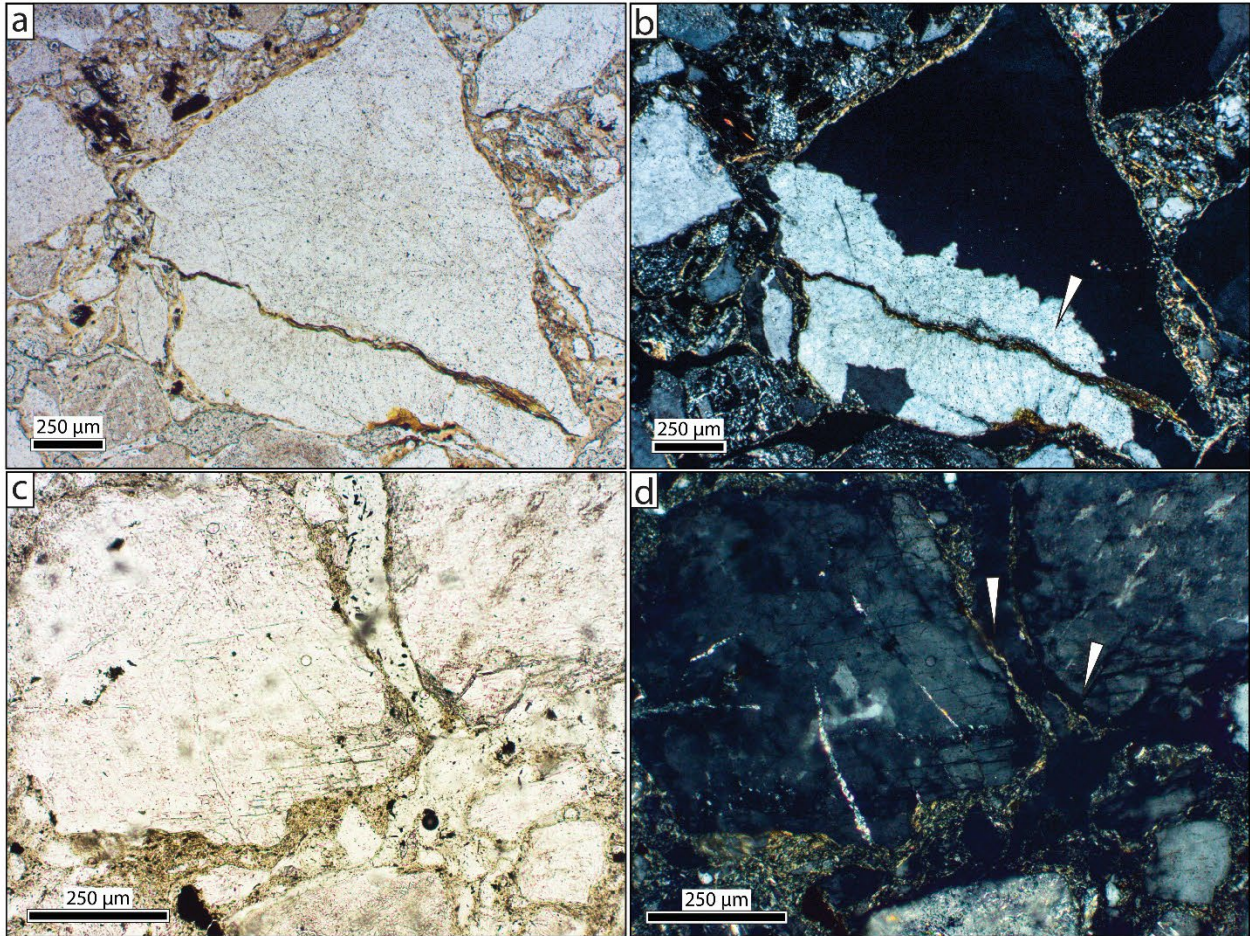


Figure 20. a) Sample CL-010520-19a, 5x, PPL. b) Sample CL-010520-19a, 5x, XPL, arrow indicates cement (brownish material) filling fracture within grain. c) Sample CL-010520-19a, 10x, PPL. d) Sample CL-010520-19a, XPL, arrows indicates cement (brownish material) filling multiple fractures within a single grain.

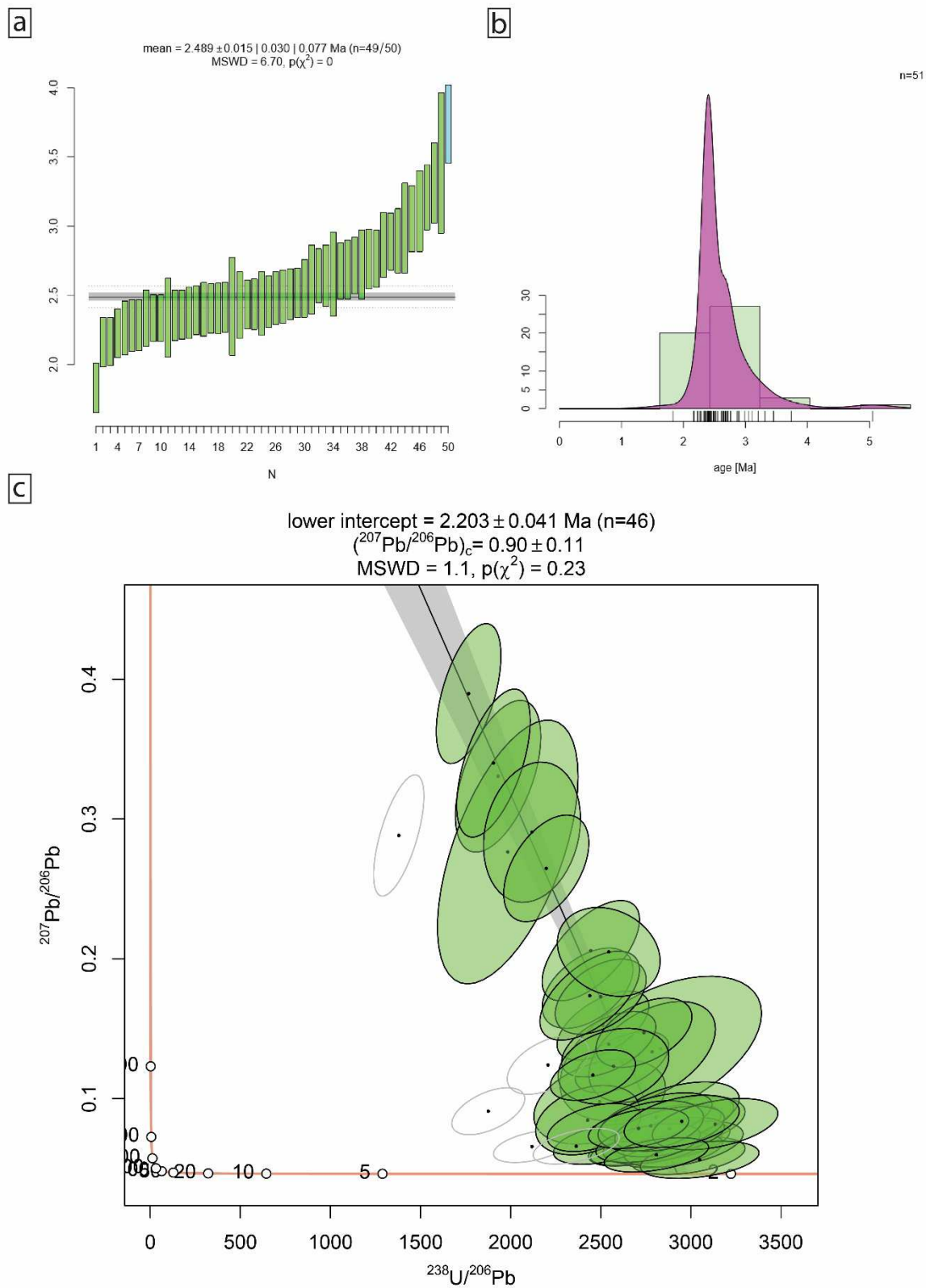


Figure 21. a) Weighted mean plot. b) Kernel density estimate, displaying one almost-normal distributed peak (incl. an older 'tail'). c) Tera-Wasserburg diagram with best age ( $2.2 \pm 0.1$  Ma). Grey, empty ellipses were excluded from the age calculation. Images in panels 'a,b' by Dr. Nikki Seymour, image in panel 'c' by Dr. John Singleton. Images generated in IsoPlotR (Vermeesch, 2018).

Table 3. Mineralogical analysis via Terraspec of faulted and non-faulted alluvial material. The Terraspec rates matches on a 3-star scale, with 3 stars (\*\*\*) corresponding to the highest confidence match. Samples with lowercase 'f' indicate samples taken from faulted zones.

Sample Name	TerraSpec Sample Name	Mineralogy Results
CL-010520-19A-f	S-30079_1020	Ferrihydrite***, Rectorite**, Palygorskite*, Magnesite*
CL-010520-19A-f	S-30079_1021	Ferrihydrite***, [SWIR] - no match
CL-010520-19B-f	S-30079_1022	Ferrihydrite***, Rectorite**, Magnesite*, Muscovite*
CL-010520-19B-f	S-30079_1023	Ferrihydrite***, [SWIR] - no match
CL-010520-19C-f	S-30079_1026	Ferrihydrite***, [SWIR] - no match
CL-010520-19C-f	S-30079_1027	Ferrihydrite***, Beidellite**, Magnesite*, Palygorskite*
201-E47A-f	S-30079_1028	Heulandite***, Ankerite**, Hornblende*, [VNIR] - no match
201-E47A-f	S-30079_1029	Palygorskite***, Hydrobiotite***, Magnesite**, Roscoelite*
CL-010520-19D	S-30079_1030	Ferrihydrite***, [SWIR] - no match
CL-010520-19D	S-30079_1031	Ferrihydrite***, Goethite*
CL-010520-19E	S-30079_1032	Ferrihydrite***, Rectorite**, Magnesite*, Muscovite*
CL-010520-19E	S-30079_1033	Ferrihydrite***, [SWIR] - no match
CL-010520-19F	S-30079_1034	Ferrihydrite***, [SWIR] - no match
CL-010520-19F	S-30079_1035	Ferrihydrite***, [SWIR] - no match
201-E47B	S-30079_1036	Ferrihydrite***, Palygorskite***, Hydrobiotite***, Magnesite**
201-E47B	S-30079_1037	Ferrihydrite***, Palygorskite***, Magnesite***, Hydrobiotite**

## 5. DISCUSSION

### 5.1 Spatial Relationship to Bedrock Features

Alluvial lineaments in the Atacama Desert are undoubtedly related to structures present in the bedrock owing to several lines of evidence present both in field data and satellite imagery:

- 1) Along the Atacama fault system and the adjacent Taltal fault system, lineaments directly trace over mapped faults and connect disparate fault segments across alluvial deposits (Figure 7).
- 2) Lineaments are commonly found in close proximity to bedrock fissures and eroded fault cores, with the trough of the lineament tracing directly into the bedrock feature along strike (Figure 5,6,16).
- 3) The spatial geometry of the lineaments mapped in this study matches the overall N- to NNW- structural grain of the region, which is largely defined by the Atacama fault system (Figure 7,8).

### 5.2 Structural Features in Alluvium of Lineament Ridges

In the alluvium that forms lineament ridges, we noted two main types of structures, either examining lineament cross-sections in natural stream-cuts or within our own hand-dug trenches. In these cross-section exposures, we found dozens of very small-scale faults or shear fractures, including several with apparent mm- to cm-scale normal-sense offset (Figure 15). These small-scale faults almost exclusively dip towards the lineament trough. In two separate hand-dug trenches through lineament ridges, we observed deformed bedding that we interpret here as possible evidence for thrust faulting along planes that dip gently toward the troughs (Figure 17,18). Importantly, at site 050 (Fig. 17), the orientation of the trench with respect to flow direction of the fan makes it unlikely that this structure is a channel bedform. However, there were only two locations where we observed this apparent thrust faulting, as opposed to the many cases where we observed the apparent normal faulting.

### 5.3 Scaling Relationships and Spatial Trends Along Alluvial Surfaces of Different Ages

Apparent alluvium age roughly corresponds to the height and width of lineament ridges in some cases, where we can observe the same lineaments visibly tracing into progressively younger surfaces. Lineament expression on the older surfaces tends to be higher relief, the ridges are broader, and the trough is wider (Figure 11,12,13; Mavor, 2021, Fig. 4.7). From DEM analysis of lineaments in cross-section, the width of lineament troughs

and height of lineament ridges increases with increased relative age of alluvial surfaces (Fig 11,12). There is also a weak positive linear correlation between lineament trough width and ridge height, meaning that lineaments with a wider trough tend to have larger relief along the ridges (Figure 10). Because younger alluvium effectively repaves or “resets” the local landscape surface, these observations suggest that lineaments grow with time. If this interpretation is correct, it provides a simple explanation for the scaling relationships observed between lineament width and height (Fig. 10), suggesting that the wider and taller lineaments are older. This inference is consistent with evidence of faulting in alluvium we observed at different lineament sites, with normal faults adjacent to the troughs and some signs of thrusting on ridge margins, which suggests active deformation of lineaments.

#### **5.4 Geochronology**

In a natural stream cut, we located a tuff bed embedded within an alluvial fan containing several lineaments and normal-sense shear fractures (Figure A21). Utilizing LA-ICP-MS U-Pb geochronology, we found that the best age for the extracted zircons is  $2.2 \pm 0.1$  Ma, or the lower intercept of the Terra-Wasserburg plot (Figure 21c). Some of the grains plot off the concordia in a linear array, indicating a component of common Pb, which is why we use this intercept as the best age. The age for this tuff implies that the surface above (the fan containing the lineaments) is younger than  $2.2 \pm 0.1$  Ma (Lower Pleistocene), giving us an upper bound for the age of these specific lineaments. It is important to recognize that this is only one age estimate for lineaments in this particular alluvial fan, and provides no empirical age data for lineaments in different areas. However, we hypothesize that lineaments formed in nearby alluvial deposits similar in color and relief are relatively close in age.

#### **5.5 Hypotheses for Lineament Genesis**

I outline three hypotheses that may explain observable lineament occurrence and morphology. Based on the evidence and interpretations presented above, I discuss each hypothesis and present my preferred model for lineament genesis. Importantly, though I identify my preferred hypothesis, it does not mean that these other ideas are necessarily incompatible with my proposed model.

- 1) Non-tectonic model: There is an expansive soil wedge beneath the lineament trough, which through multiple shrink-swell cycles builds relief on ridges.
- 2) Tectonic model I: Lineaments are the surface expression of bedrock fault scarps.

- 3) Tectonic model II: Lineaments nucleate over any linear discontinuity in the bedrock, and are a product of expansion and contraction cycles brought on by the regional seismic cycle, with topography built through normal faulting combined with reverse faulting, then sculpting by wind and water.

Arabasz (1971) suggests a non-tectonic origin for lineaments, though he ultimately concludes that tectonic factors cannot be ruled out as lineaments are commonly found along bedrock faults and the alluvium itself is faulted. His hypothesis suggests a wedge of expansive soil is present beneath each trough, where repeated shrink-swell cycles develop the relief on the ridges (Arabasz, 1971). Arabasz's hypothesis for lineament formation does not attribute relief on lineament ridges to bedrock faulting or cracking. My investigation did not do any testing of soil expansivity, either in the trough or in the ridges, so it can neither confirm nor deny a pedogenic influence in lineament formation. The mineralogic analysis of the cement reveals mixed results as well: the clays present in the samples are mostly rectorite and palygorskite, rectorite being only a partially-swelling clay (Li et al., 2020) whereas palygorskite is known for its high swelling capacity (Murray, 2000; Aiban, 2006). However, in our visits to field sites we observed that the alluvium is generally coarse-grained (sand to pebbles) with little clay content, so it is unlikely that any expansive properties associated with the clays heavily influences expansivity of the alluvium as a whole.

In some areas, it is clear that lineaments are the surface expression of bedrock faults. They often trace directly over mapped bedrock faults and connect separate fault strands (Figure 2d, 5, 7). At one site, we observed a bedrock fault with apparent normal-sense offset along strike with a mapped alluvial lineament, dipping towards the trough (Figure 16). Here, this apparent normal fault appears to correspond with the trough margin (the point where the ridge and trough meet). Many lineaments, particularly ones with geometries consistent with the underlying structural geometry of the bedrock, may indeed be the surface expression of faults. Audin et al. (2003) mapped several NE-trending lineaments in the Andean Precordillera as eastward-dipping half-grabens (Audin et al., 2003, Fig. 4). However, the broad-scale symmetry of most lineament profiles is not consistent with fault scarps above dip-slip faults, which are largely asymmetrical owing to the down-thrown block. As for possible strike-slip motion, we did not observe any laterally offset drainages or any other indicators. In his study, Arabasz (1971) notes the absence of vertical offset across lineaments, and that "it would appear hazardous, then, to attribute their origin or development to strike-slip movement." In this point, he suggests that while there is no observable vertical/dip-slip

offset, one cannot assume that strike-slip motion is therefore responsible (Arabasz, 1971). Many lineaments may form over simple opening-mode cracks corresponding to the fissures we see exposed in nearby bedrock. In nearly all cases where a lineament can be traced directly into bedrock, the bedrock structure appears to record some component of opening-mode fracturing. While the overall orientation of lineament populations matches the NNW structural orientation of the region, there are small populations of lineaments that deviate from this overall dominant pattern, particularly in the lineament population mapped west of the AFS (Figure 8a). That said, small populations of faults in a variety of orientations do exist in this field area, including small-scale faults around the AFS (Mavor, 2021, Figure 4.3e).

Lineament genesis is likely a result of a combination of factors, including some of those described by the previous hypotheses. Our current hypothesis is predicated on the idea that lineaments are actively deforming features, influenced by the regional stress field generated by the convergent plate boundary that fluctuates from contraction to extension in parts of the forearc throughout the seismic cycle (Delouis et al., 1998). At less than ~2.2 Ma, at least a portion of the lineament population in the field area is relatively young. The positive linear correlation between lineament trough width and ridge height, combined with observations of larger lineaments present in relatively older alluvial surfaces, supports the idea that they are growing through time.

Our current hypothesis for lineament genesis is as follows:

- 1) A lineament nucleates over a sub-vertical, linear discontinuity in the bedrock, like a bedrock fault, an opening-mode fracture, or even an eroded dike.
- 2) During the coseismic/postseismic period of the seismic cycle, relaxation of the plate results in extensional structures like normal faults and opening-mode cracks ( $\sigma_1$  is trench-parallel,  $\sigma_3$  is trench perpendicular). These structures are responsible for the formation of the “trough” in the alluvial cover, which act like a graben structurally. The bedrock beneath accommodates extension through a vertical, opening-mode crack/fissure.
- 3) During the interseismic period, compressional stresses oriented perpendicular to the plate boundary form low-angle thrust faults in the flanks of the lineament. These reverse faults are responsible for the building of topography in lineament ridges.
- 4) Repeated episodes of extension and contraction throughout the seismic cycle build lineament topography.

- 5) Over a lineament's 'lifetime,' geomorphic processes of fluvial and eolian weathering and erosion further sculpt the lineaments into smooth, curvilinear ridges (Figure 22).

A key observation suggesting that faulting is responsible for the formation of the lineaments is the occurrence of small normal faults in the lineament shoulders (Figure 15,19). These small-scale faults are preserved in well-indurated alluvium, rather than bedrock, implying that they are likely relatively young structures. In addition, the thin sections of these faulted areas of alluvium show cement that penetrates the fractures within individual grains, suggesting that these areas may have experienced periods of fracturing and re-cementation (Figure 20). As the faults found in the alluvium are small and high-angle, it is likely they accommodated very little extension via normal-sense slip. Instead, larger bedrock fissures (Fig. 6) may accommodate most of the extension beneath the surface via opening-mode cracks. We observed both microcrystalline and coarse-grained gypsum and calcite in these nearby bedrock fissures where they crop out at the surface. Though these minerals may be pedogenic in origin, their presence on high ridgetops suggests otherwise. Groundwater upwellings have been attributed to earthquake activity in the region, resulting in successive salt crusts overlying faults associated with porphyry copper deposits. The salt crusts (which include the mineral gypsum) have a relatively high concentration of Cu, indicating the upward mobilization of the elements (Cameron et al., 2013). "Seismic pumping" of hydrothermal fluids is a mechanism by which fluids circulate within fault zones, emerging as steam or thermal springs (Sibson et al., 1975; McCaig, 1988; Chandrasekharam, 1989). Dilatation, or alternating episodes of compression and tensile stress (brought on by earthquakes) is the driving mechanism behind this model, with faults opening/closing and creating changes in the fluid pressure of the system (McCaig, 1988; Sibson et al., 1998; Chandrasekharam, 1989). It is possible that the presence of gypsum in bedrock fissures associated with lineaments indicates recent to semi-recent earthquake activity.

### **5.6 The Seismic Cycle in Subduction Systems**

In subduction systems, the seismic cycle exerts a strong control on the frequency, occurrence, and geometry of earthquake events in the region. Along the Nazca-South American plate boundary, the subduction margin is hypothesized to rupture in characteristic segments (e.g., Chlieh et al., 2004; Béjar-Pizarro et al., 2010; Jara-Muñoz et al., 2015). In general terms, the interseismic period is characterized by the accumulation of strain

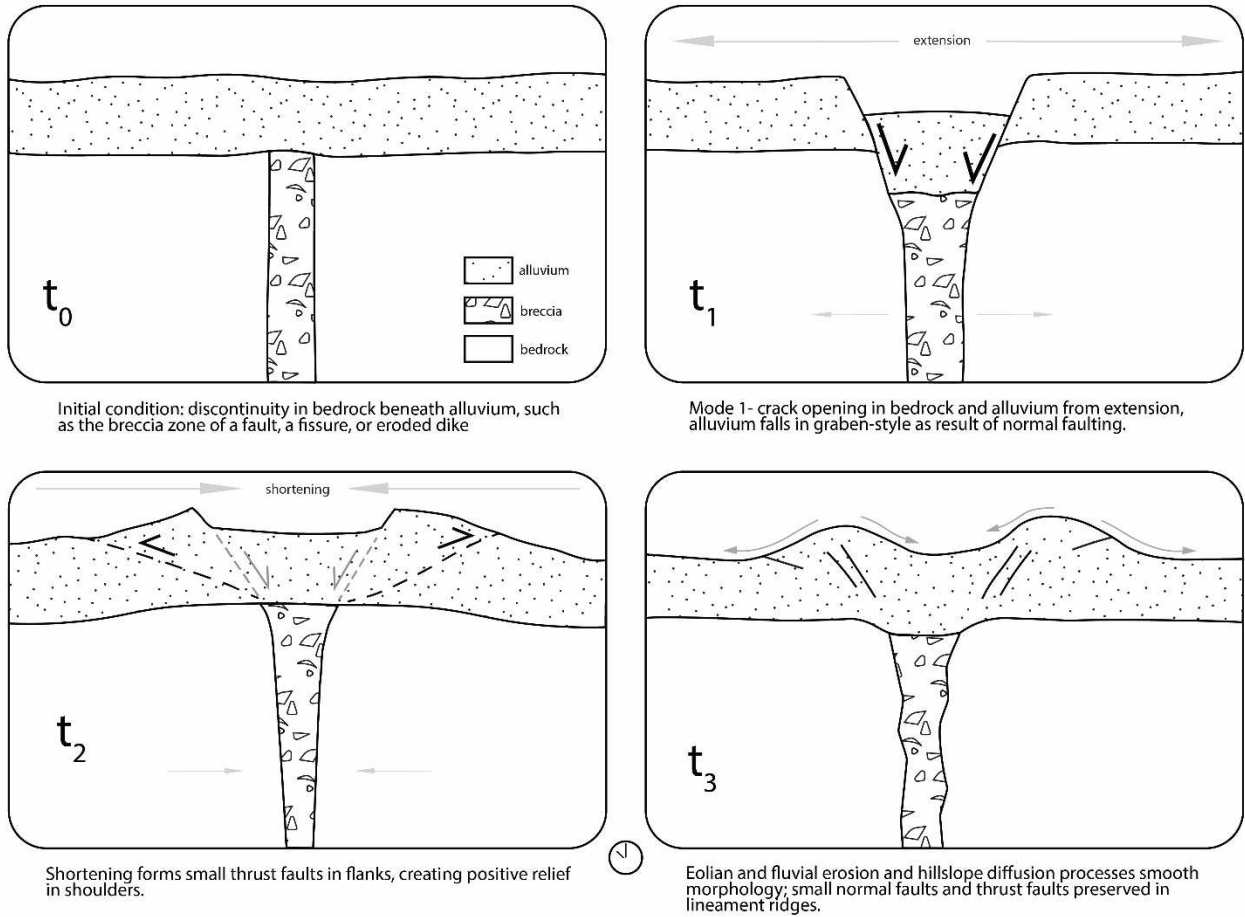


Figure 22. Illustration of lineament formation hypothesis in cross-section. Amount of offset pictured is exaggerated; not to scale. Repeated cycles of extension and shortening over time are implied before the final morphology pictured in t<sub>3</sub>.

along the plate interface and typically operates on a time scale of decades to centuries. The coseismic period is instantaneous, and the postseismic period immediately follows, lasting days to decades, characterized by “relaxation” and further deformation of the plate. The northern Chile rupture segment has an estimated recurrence interval of 111–264 years (Comte and Pardo, 1991; Nishenko 1991). Given a maximum age of the lineaments in one area of 2.2 Ma, and an estimated recurrence interval of ~200 years, these lineaments may have experienced somewhere on the order of 11,000 seismic cycles. Given that the overall NNW orientation of the lineament population is effectively perpendicular to the Nazca-South American convergence vector (Pardo-Casas and Molnar, 1987), this plate boundary geometry appears conducive to creating the alternating stress regimes responsible for the normal and thrust faulting hypothesized in lineament genesis.

Jolivet et al., (2020) suggests that large-scale topography in northern Chile (e.g., coastal landforms) grows during the interseismic period, so it is possible that relatively small-scale structures such as lineaments grow topography during this period as well as a result of accumulated strain. There is also evidence in some locations for normal faults reactivating as reverse faults (Loveless et al., 2010). In fact, Loveless et al. (2010) attribute these reverse fault activations as responses to stress changes in the upper plate as a result of the regional seismic cycle. It is possible that normal fault to reverse fault reactivation could contribute to building lineament topography over time, though we did not observe evidence of this in the field as we saw no moderate- to high-angle structures with apparent reverse-sense offset.

Normal faulting and formation of opening-mode cracks in the region has been widely documented (Arabasz 1971; González et al., 2003; Loveless et al., 2005), which we hypothesize may form lineaments via extension during the coseismic portion of the seismic cycle (and into the postseismic period as the plate relaxes). There is existing precedent for tectonic geomorphic features (surface cracks) being attributed to the characteristic rupture segments of the Nazca-South American plate boundary (Loveless et al., 2005; 2009), and we propose that lineaments may be similar to surface cracks in how they respond to regional tectonics. Allmendinger and Gonzalez (2010) notes that while surface cracks form via different mechanisms, crack formation resulting from coseismic extension is a particularly important one. The gypsum we observed in bedrock fissures may be a product of seismic pumping (discussed above), which could also indicate that the opening-component of the fissures is coseismic.

Importantly, the model I have outlined represents a simplified interpretation of the state of stress in the plate during the interseismic period, as the interseismic period may include seismic loading as well as relaxation in the plate (sometimes called the postseismic period; Delouis et al, 1998; Jolivet et al., 2020; Chlieh et al., 2004). The stresses and subsequent strain associated with lineament formation may represent an unrealized component in models of earthquake ruptures in subduction zones (e.g., van Dinther et al., 2014; Noda et al., 2021). Alluvial lineaments may be common features in many subduction zones across the world, though the extreme aridity and lack of vegetation in the Atacama Desert may preserve these features especially well. With the increasing availability of remotely-sensed data (LIDAR, drone footage, high-resolution satellite images) it is possible that lineaments could be detected in other subduction zones experiencing a similar regional stress regime.

## 6. CONCLUSIONS

### 6.1 Review of Key Findings

The Atacama Desert is an ideal place to study neotectonic features preserved in the forearc. Through this research, our conclusions can be summarized as follows:

- 1) Lineaments are visible in satellite imagery, characterized by continuous sets of linear ridges with an M-shaped topographic profile in cross-section; lineaments can be up to a few kilometers in length, up to ~100 meters wide, with the ridges ranging from ~0.5–3 meters tall.
- 2) Lineaments are commonly found in close proximity to planar bedrock features; typically faults and opening-mode cracks/fissures. Lineament troughs are commonly found along strike with bedrock fissures, which contain high concentrations of gypsum and calcite that may record seismic pumping and channelization of fluids during coseismic opening.
- 3) Multiple structures are visible in the alluvium in lineament cross-sections, exposed either through natural incision by stream cuts or through hand-dug trenches:
  - a. Small-scale faults dip moderately to steeply (~50–70°) towards the trough, some with cm- to mm-scale apparent normal-sense offset. Thin sections extracted from these faulted zones show increased cementation where cement penetrates fractured grain boundaries.
  - b. In trenches, gently dipping planes resembling thrust faults dip shallowly (~15–20°) towards the trough.
- 4) Lineaments in older alluvial surfaces (based on relative age) tend to have taller and broader ridges and wider troughs, indicating that lineaments have grown with time. There is a weak linear correlation between trough width and ridge height ( $r^2 = 0.39$ ), meaning that wider lineaments often have taller ridges.
- 5) An alluvial fan with several lineaments has an ash-fall tuff with a Lower Pleistocene age of  $2.2 \pm 0.1$  Ma, indicating that at least some of the lineaments are Quaternary structures.
- 6) We hypothesize that lineaments form in response to alternating forearc shortening and extension related to interseismic and coseismic phases of the earthquake cycle, with the development of ridges and thrust faults

recording interseismic shortening and normal faults and fissures which form the central troughs recording coseismic extension.

## **6.2 Future Work**

This project is another crucial step in the investigation into neotectonic alluvial lineaments. The mapping portion of this research is focused around the roughly one hundred field stations recorded during our one field season in January 2020, and also includes mapping in major alluvial deposits found between the stations. However, the lineament dataset used to compute orientation statistics in this study would more accurately represent the lineament population if more lineaments were added. This research project would also benefit from more drone flights over targeted lineament sites, particularly those like CL-010520-15, where lineaments cross alluvial fan surfaces of different ages. These flights would provide additional DEMs and profile data to show the changes in lineament morphology over surfaces of different ages. Additionally, further examination of lineaments in cross-section is needed, whether from natural exposures or by artificial trenching, to further test the hypothesis that normal faults create the down-dropped trough, and/or that ridges are built from thrust faults. Testing the soil for expansivity, both in the ridges and especially the trough, could help in confirming or refuting the validity of the non-tectonic hypothesis for lineament formation from Arabasz (1971). This body of research would also improve with more instances of absolute dating of lineament sites in order to more closely constrain lineament age. If lineament ages can be accurately determined, systematic comparison with seismic events and recurrence intervals may further serve to link their formation to the seismic cycle.

## REFERENCES

- Aiban, S. A. (2006). Compressibility and swelling characteristics of Al-Khobar Palygorskite, eastern Saudi Arabia. *Engineering Geology*, 87(3), 205–219. doi:10.1016/j.enggeo.2006.07.003
- Allmendinger, R. W., Cardozo, N., and Fisher, D. (2012) Structural geology algorithms: Vectors and tensors in structural geology: Cambridge University Press (book to be published in early 2012).
- Allmendinger, R. W., & González, G. (2010). Invited review paper: Neogene to Quaternary tectonics of the coastal Cordillera, northern Chile. *Tectonophysics*, 495(1–2), 93–110. doi:10.1016/j.tecto.2009.04.019
- Allmendinger, R. W., Siron, C. R., & Scott, C. P. (2017). Structural data collection with mobile devices: Accuracy, redundancy, and best practices. *Journal of Structural Geology*, 102, 98–112. doi:10.1016/j.jsg.2017.07.011
- Álvarez, J., Jorquera, R., Miralles, C., Padel, M., & Martínez, P. (2016). Cartas Punta Posallaves y Sierra Vicuña Mackenna, Región de Antofagasta. Servicio Nacional de Geología y Minería. Carta Geológica de Chile, Serie Geología Básica, 183–184, p.151, 1 mapa escala 1:100.000. Santiago.
- Angermann, D., Klotz, J., & Reigber, C. (1999). Space-geodetic estimation of the Nazca–South America Euler vector. *Earth and Planetary Science Letters*, 171(3), 329–334.
- Arabasz, W. J. (Jr). (1971). Geological and geophysical studies of the Atacama fault zone in northern Chile. Thesis.
- Audin, L., Hérail, G., Riquelme, R., Darrozes, J., Martinod, J., & Font, E. (2003). Geomorphological markers of faulting and neotectonic activity along the western Andean margin, northern Chile. *Journal of Quaternary Science*, 18(8), 681–694. doi:10.1002/jqs.787
- Béjar-Pizarro, M., Carrizo, D., Socquet, A., Armijo, R., Barrientos, S., Bondoux, F., Bonvalot, S., Campos, J., Comte, D., de Chabalier, J. B., Charade, O., Delorme, A., Gabalda, G., Galetzka, J., Genrich, J., Necessian, A., Olcay, M., Ortega, F., Ortega, I., ... Vigny, C. (2010). Asperities and barriers on the seismogenic zone in North Chile: State-of-the-art after the 2007 Mw 7.7 Tocopilla earthquake inferred by GPS and InSAR data. *Geophysical Journal International*, 183(1), 390–406. doi:10.1111/j.1365-246X.2010.04748.x

- Bell, C. M. (1982). THE LOWER PALEOZOIC METASEDIMENTARY BASEMENT OF THE COASTAL RANGES OF CHILE BETWEEN 25° 30' and 27° S. *Andean Geology*, 17(17).
- Bevis, M., Kendrick, E., Smalley Jr., R., Brooks, B., Allmendinger, R., & Isacks, B. (2001). On the strength of interplate coupling and the rate of back arc convergence in the central Andes: An analysis of the interseismic velocity field. *Geochemistry, Geophysics, Geosystems*, 2(11). [doi:10.1029/2001GC000198](https://doi.org/10.1029/2001GC000198)
- Buske, S., Lüth, S., Meyer, H., Patzig, R., Reichert, C., Shapiro, S., Wigger, P., & Yoon, M. (2002). Broad depth range seismic imaging of the subducted Nazca Slab, North Chile. *Tectonophysics*, 350(4), 273–282. [doi:10.1016/S0040-1951\(02\)00117-8](https://doi.org/10.1016/S0040-1951(02)00117-8)
- Cameron, E. M. (2013). From Chile to Nevada to the Athabasca basin: Earthquake-induced geochemical anomalies from near-field to far-field. *Geochemistry: Exploration, Environment, Analysis*, 13(1), 41–51. [doi:10.1144/geochem2012-143](https://doi.org/10.1144/geochem2012-143)
- Cardozo, N., and Allmendinger, R.W. (2013). Spherical projections with OSXStereonet: Computers & Geosciences, v. 51, p. 193 – 205. [doi:10.1016/j.cageo.2012.07.021](https://doi.org/10.1016/j.cageo.2012.07.021).
- Chandrasekharam, D. (1989). STEAM EMANATION DUE TO SEISMIC PUMPING, KILLARI, MAHARASHTRA. Geological Survey of India Special Publication.
- Charrier (coordinator), R., Pinto, L., & Rodríguez, M. P. (2007). Tectonostratigraphic evolution of the Andean Orogen in Chile. In T. Moreno & W. Gibbons (Eds.), *The Geology of Chile* (p. 0). Geological Society of London. [doi:10.1144/GOCH.3](https://doi.org/10.1144/GOCH.3)
- Chlieh, M., De Chabalier, J. B., Ruegg, J. C., Armijo, R., Dmowska, R., Campos, J., & Feigl, K. L. (2004). Crustal deformation and fault slip during the seismic cycle in the North Chile subduction zone, from GPS and InSAR observations. *Geophysical Journal International*, 158(2), 695–711. [doi:10.1111/j.1365-246X.2004.02326.x](https://doi.org/10.1111/j.1365-246X.2004.02326.x)
- Comte, D., & Pardo, M. (1991). Reappraisal of great historical earthquakes in the Northern Chile and Southern Peru seismic gaps. *Natural Hazards*, 4, 23–44. [doi:10.1007/BF00126557](https://doi.org/10.1007/BF00126557)

- Contreras, J.P., Espinoza, M., De la Cruz, R., Jorquera, R., Kraus, S., Ramírez, C., Naranjo, J.A., Escribano, & J., Martínez, P. (2013). Carta Cifuncho, Regiones de Antofagasta y Atacama. Servicio Nacional de Geología y Minería, Carta Geológica de Chile, Serie Geología Básica 161, 1 mapa escala 1:100.000. Santiago.
- Díaz, G. C., Mendoza, M., García-Veigas, J., Pueyo, J. J., & Turner, P. (1999). Evolution and geochemical signatures in a Neogene forearc evaporitic basin: The Salar Grande (Central Andes of Chile). *Palaeogeography, Palaeoclimatology, Palaeoecology*, *151*, 39–54. [doi:10.1016/S0031-0182\(99\)00014-0](https://doi.org/10.1016/S0031-0182(99)00014-0)
- Delouis, B., Philip, H., Dorbath, L., & Cisternas, A. (1998). Recent crustal deformation in the Antofagasta region (northern Chile) and the subduction process. *Geophysical Journal International*, *132*(2), 302–338. [doi:10.1046/j.1365-246x.1998.00439.x](https://doi.org/10.1046/j.1365-246x.1998.00439.x)
- Ericksen, G. E. (1983). The Chilean Nitrate Deposits: The origin of the Chilean nitrate deposits, which contain a unique group of saline minerals, has provoked lively discussion for more than 100 years. *American Scientist*, *71*(4), 366–374.
- Escribano, J., Martínez, P., Domagala, J., Padel, M., Espinoza, M., Jorquera, R., Contreras, J.P., De la Cruz, R., & Calderón, M. (2013). Cartas Bahía Isla Blanca y Taltal. Servicio Nacional de Geología y Minería, Carta Geológica de Chile, Serie Geología Básica 164-165: 75 p. 1 mapa escala 1:100.000. Santiago.
- Espinoza, M., Contreras, J. P., Jorquera, R., De la Cruz, R., Kraus, S., Ramírez, C., & Naranjo, J. A. (2014). Carta Cerro del Pingo, Regiones de Antofagasta y de Atacama. Servicio Nacional de Geología y Minería, Carta Geológica de Chile, Serie Geología Básica 169. 1 mapa escala 1:100.000. Santiago.
- Fuentes, P., Díaz-Alvarado, J., Fernández, C., Díaz-Azpiroz, M., & Rodríguez, N. (2016). Structural analysis and shape-preferred orientation determination of the mélangé facies in the Chañaral mélangé, Las Tórtolas Formation, Coastal Cordillera, northern Chile. *Journal of South American Earth Sciences*, *67*, 40–56. [doi:10.1016/j.jsames.2016.02.001](https://doi.org/10.1016/j.jsames.2016.02.001)
- Google. (n.d.-a). [Imagery of fissures and lineaments in the Atacama Desert near 25.671715° S, 70.382164°W]. Retrieved February 2, 2023, from Google Earth Pro Desktop, ver. 7.3.6.9345.

- Google. (n.d.-b). [Imagery of fissures and lineaments in the Atacama Desert near 25.915684° S, 70.520059°W]. Retrieved February 2, 2023, from Google Earth Pro Desktop, ver. 7.3.6.9345.
- Google. (n.d.-c). [Imagery of fissures and lineaments in the Atacama Desert near 25.932497° S, 70.525411°W]. Retrieved February 2, 2023, from Google Earth Pro Desktop, ver. 7.3.6.9345.
- Google. (n.d.-d). [Imagery of fissures and lineaments in the Atacama Desert near 25.636786° S, 70.319907°W]. Retrieved February 2, 2023, from Google Earth Pro Desktop, ver. 7.3.6.9345.
- Google. (n.d.-e). [Imagery of lineaments in the Atacama Desert near 25.896264° S, 70.519692°W]. Retrieved December 22, 2022, from Google Earth Pro Desktop, ver. 7.3.4.8642.
- Google. (n.d.-f). [Imagery of fissures and lineaments in the Atacama Desert near 25.504949° S, 70.336080°W]. Retrieved September 8, 2022, from Google Earth Pro Desktop, ver. 7.3.4.8642.
- González, G., Cembrano, J., Carrizo, D., Macci, A., & Schneider, H. (2003). The link between forearc tectonics and Pliocene–Quaternary deformation of the Coastal Cordillera, northern Chile. *Journal of South American Earth Sciences*, 16(5), 321–342. [doi:10.1016/S0895-9811\(03\)00100-7](https://doi.org/10.1016/S0895-9811(03)00100-7)
- Grocott, J., & Taylor, G. K. (2002). Magmatic arc fault systems, deformation partitioning and emplacement of granitic complexes in the Coastal Cordillera, north Chilean Andes (25°30'S to 27°00'). *Journal of the Geological Society, London*, 159, 425–442.
- Hartley, A. J., & Chong, G. (2002). Late Pliocene age for the Atacama Desert: Implications for the desertification of western South America. *Geology*, 30(1), 43–46. [doi:10.1130/0091-7613\(2002\)030<0043:LPAFTA>2.0.CO;2](https://doi.org/10.1130/0091-7613(2002)030<0043:LPAFTA>2.0.CO;2)
- Horton, B. K. (2018). Sedimentary record of Andean mountain building. *Earth-Science Reviews*, 178, 279–309. [doi:10.1016/j.earscirev.2017.11.025](https://doi.org/10.1016/j.earscirev.2017.11.025)
- Houston, J., & Hartley, A. J. (2003). The central Andean west-slope rainshadow and its potential contribution to the origin of hyper-aridity in the Atacama Desert. *International Journal of Climatology*, 23(12), 1453–1464. [doi:10.1002/joc.938](https://doi.org/10.1002/joc.938)

- Husen, S., Kissling, E., Flueh, E., & Asch, G. (1999). Accurate hypocentre determination in the seismogenic zone of the subducting Nazca Plate in northern Chile using a combined on-/offshore network. *Geophysical Journal International*, 138(3), 687–701. [doi:10.1046/j.1365-246x.1999.00893.x](https://doi.org/10.1046/j.1365-246x.1999.00893.x)
- Husen, S., Kissling, E., & Flueh, E. R. (2000). Local earthquake tomography of shallow subduction in north Chile: A combined onshore and offshore study. *Journal of Geophysical Research: Solid Earth*, 105(B12), 28183–28198. [doi:10.1029/2000JB900229](https://doi.org/10.1029/2000JB900229)
- International Seismological Centre (2023), On-line Event Bibliography, [doi:10.31905/EJ3B5LV6](https://doi.org/10.31905/EJ3B5LV6)
- Jara-Muñoz, J., Melnick, D., Brill, D., & Strecker, M. R. (2015). Segmentation of the 2010 Maule Chile earthquake rupture from a joint analysis of uplifted marine terraces and seismic-cycle deformation patterns. *Quaternary Science Reviews*, 113, 171–192. [doi:10.1016/j.quascirev.2015.01.005](https://doi.org/10.1016/j.quascirev.2015.01.005)
- Jenness, J. (2014). Polar plots for ArcGIS. Jenness Enterprises. Retrieved from: [http://www.jennessent.com/arcgis/polar\\_plots.htm](http://www.jennessent.com/arcgis/polar_plots.htm).
- Jolivet, R., Simons, M., Duputel, Z., Olive, J.-A., Bhat, H. S., & Bletery, Q. (2020). Interseismic Loading of Subduction Megathrust Drives Long-Term Uplift in Northern Chile. *Geophysical Research Letters*, 47(8), e2019GL085377. [doi:10.1029/2019GL085377](https://doi.org/10.1029/2019GL085377)
- Kendrick, E., Bevis, M., Smalley Jr., R., Brooks, B., Vargas, R. B., Lauría, E., & Fortes, L. P. S. (2003). The Nazca–South America Euler vector and its rate of change. *Journal of South American Earth Sciences*, 16, 125–131.
- Khazaradze, G., & Klotz, J. (2003). Short- and long-term effects of GPS measured crustal deformation rates along the south central Andes. *Journal of Geophysical Research: Solid Earth*, 108(B6). [doi:10.1029/2002JB001879](https://doi.org/10.1029/2002JB001879)
- Klotz, J., Khazaradze, G., Angermann, D., Reigber, C., Perdomo, R., & Cifuentes, O. (2001). Earthquake cycle dominates contemporary crustal deformation in Central and Southern Andes. *Earth and Planetary Science Letters*, 193, 437–446. [doi:10.1016/S0012-821X\(01\)00532-5](https://doi.org/10.1016/S0012-821X(01)00532-5)

- Li, S., He, H., Tao, Q., Zhu, J., Tan, W., Ji, S., Yang, Y., & Zhang, C. (2020). Kaolinization of 2:1 type clay minerals with different swelling properties. *The American Mineralogist*, 105(5), 687–696. doi:10.2138/am-2020-7339
- Loveless, J. P., Allmendinger, R. W., Pritchard, M. E., Garroway, J. L., & González, G. (2009). Surface cracks record long-term seismic segmentation of the Andean margin. *Geology*, 37(1), 23–26.  
[doi:10.1130/G25170A.1](https://doi.org/10.1130/G25170A.1)
- Loveless, J. P., Allmendinger, R. W., Pritchard, M. E., & González, G. (2010). Normal and reverse faulting driven by the subduction zone earthquake cycle in the northern Chilean fore arc. *Tectonics*, 29(2).  
[doi:10.1029/2009TC002465](https://doi.org/10.1029/2009TC002465)
- Loveless, J. P., Hoke, G. D., Allmendinger, R. W., González, G., Isacks, B. L., & Carrizo, D. A. (2005). Pervasive cracking of the northern Chilean Coastal Cordillera: New evidence for forearc extension. *Geology*, 33(12), 973–976. [doi:10.1130/G22004.1](https://doi.org/10.1130/G22004.1)
- María Pía Rodríguez, Sébastien Carretier, Reynaldo Charrier, Marianne Saillard, Vincent Regard, Gérard Hérail, Sarah Hall, Dan Farber, & Laurence Audin. (2013). Geochronology of pediments and marine terraces in north-central Chile and their implications for Quaternary uplift in the Western Andes. *Geomorphology*, 180–181, 33–46. [doi:10.1016/j.geomorph.2012.09.003](https://doi.org/10.1016/j.geomorph.2012.09.003)
- Mavor, S.P. (2021). Timing, Kinematics, and Tectonic Significance of Strike-Slip Fault Systems in the Atacama Desert of Northern Chile and the Lower Colorado River Corridor, USA (Doctoral dissertation, Colorado State University).
- Mavor, S. P., Singleton, J. S., Gomila, R., Heuser, G., Seymour, N. M., Williams, S. A., Arancibia, G., Johnston, S. M., Kylander-Clark, A. R. C., & Stockli, D. F. (2020). Timing, Kinematics, and Displacement of the Taltal Fault System, Northern Chile: Implications for the Cretaceous Tectonic Evolution of the Andean Margin. *Tectonics*, 39(2). [doi:10.1029/2019TC005832](https://doi.org/10.1029/2019TC005832)
- Marinovic, N.; Smoje, I.; Maksaev, V.; Hervé, M.; Mpodozis, C. (1995). Hoja Aguas Blancas, Región de Antofagasta. Servicio Nacional de Geología y Minería, Carta Geológica de Chile, No. 70, 150 p., 1 mapa escala 1:250.000. Santiago.

- McCaig, A. M. (1988). Deep fluid circulation in fault zones. *Geology*, 16(10), 867. [doi:10.1130/0091-7613\(1988\)016<0867:DFCIFZ>2.3.CO;2](https://doi.org/10.1130/0091-7613(1988)016<0867:DFCIFZ>2.3.CO;2)
- Mpodozis, C., & Ramos, V. (1989). The Andes of Chile and Argentina, in: *Geology of the Andes and its Relation to Hydrocarbon and Mineral Resources. Earth Science Series, 11*, 59–90.
- Murray, H. H. (2000). Traditional and new applications for kaolin, smectite, and palygorskite: A general overview. *Applied Clay Science*, 17(5–6), 207–221. doi:10.1016/S0169-1317(00)00016-8
- Nishenko, S. P. (1991). Circum-Pacific Seismic Potential: 1989–1999. In E. A. Okal (Ed.), *Aspects of Pacific Seismicity* (pp. 169–259). Birkhäuser. [doi:10.1007/978-3-0348-5639-3\\_2](https://doi.org/10.1007/978-3-0348-5639-3_2)
- Nishiizumi, K., Caffee, M., Finkel, R., Brimhall, G., & Mote, T. (2005). Remnants of a fossil alluvial fan landscape of Miocene age in the Atacama Desert of northern Chile using cosmogenic nuclide exposure age dating. *Earth and Planetary Science Letters*, 237, 499–507. [doi:10.1016/j.epsl.2005.05.032](https://doi.org/10.1016/j.epsl.2005.05.032)
- Noda, A., Saito, T., Fukuyama, E., & Urata, Y. (2021). Energy-Based Scenarios for Great Thrust-Type Earthquakes in the Nankai Trough Subduction Zone, Southwest Japan, Using an Interseismic Slip-Deficit Model. *Journal of Geophysical Research: Solid Earth*, 126(5). [doi:10.1029/2020JB020417](https://doi.org/10.1029/2020JB020417)
- Pardo-Casas, F., & Molnar, P. (1987). Relative motion of the Nazca (Farallon) and South American plates since late Cretaceous time. *Tectonics*, 6(3), 233–348. [doi:10.1029/TC006i003p00233](https://doi.org/10.1029/TC006i003p00233)
- Rech, J. A., Currie, B. S., Michalski, G., & Cowan, A. M. (2006). Neogene climate change and uplift in the Atacama Desert, Chile. *Geology*, 34, 761–764. [doi:10.1130/G22444.1](https://doi.org/10.1130/G22444.1)
- Regard, V., Saillard, M., Martinod, J., Audin, L., Carretier, S., Kevin Pedoja, Rodrigo Riquelme, Paola Paredes, & Gérard Hérail. (2010). Renewed uplift of the Central Andes Forearc revealed by coastal evolution during the Quaternary. *Earth and Planetary Science Letters*, 297, 199–210. [doi:10.1016/j.epsl.2010.06.020](https://doi.org/10.1016/j.epsl.2010.06.020)
- Riquelme, R., Martinod, J., Hérail, G., Darrozes, J., & Charrier, R. (2003). A geomorphological approach to determining the Neogene to Recent deformation in the Coastal Cordillera of northern Chile (Atacama). *Tectonophysics*, 361, 255–275. [doi:10.1016/S0040-1951\(02\)00649-2](https://doi.org/10.1016/S0040-1951(02)00649-2)

- Rodríguez, M. P., Carretier, S., Charrier, R., Saillard, M., Regard, V., Hérail, G., Hall, S., Farber, D., & Audin, L. (2013). Geochronology of pediments and marine terraces in north-central Chile and their implications for Quaternary uplift in the Western Andes. *Geomorphology*, 180–181, 33–46. [doi:10.1016/j.geomorph.2012.09.003](https://doi.org/10.1016/j.geomorph.2012.09.003)
- Sáez, A., Cabrera, L., Jensen, A., & Chong, G. (1999). Late Neogene lacustrine record and palaeogeography in the Quillagua—Llamara basin, Central Andean fore-arc (northern Chile). *Palaeogeography, Palaeoclimatology, Palaeoecology*, 151, 5–37.
- Scheuber, E., & Gonzalez, G. (1999). Tectonics of the Jurassic-Early Cretaceous magmatic arc of the north Chilean Coastal Cordillera (22°–26°S): A story of crustal deformation along a convergent plate boundary. *Tectonics*, 18(5), 895–910. [doi:10.1029/1999TC900024](https://doi.org/10.1029/1999TC900024)
- Schwanghart, W., Scherler, D. (2014): TopoToolbox 2 – MATLAB-based software for topographic analysis and modeling in Earth surface sciences. *Earth Surface Dynamics*, 2, 1-7. [doi:10.5194/esurf-2-1-2014](https://doi.org/10.5194/esurf-2-1-2014)
- Schween, J. H., Hoffmeister, D., & Löhnert, U. (2020). Filling the observational gap in the Atacama Desert with a new network of climate stations. *Global and Planetary Change*, 184, 103034. [doi:10.1016/j.gloplacha.2019.103034](https://doi.org/10.1016/j.gloplacha.2019.103034)
- Seymour, N. M., Singleton, J. S., Mavor, S. P., Gomila, R., Stockli, D. F., Heuser, G., & Arancibia, G. (2020). The Relationship Between Magmatism and Deformation Along the Intra-arc Strike-Slip Atacama Fault System, Northern Chile. *Tectonics*, 39(3), e2019TC005702. [doi:10.1029/2019TC005702](https://doi.org/10.1029/2019TC005702)
- Seymour, N. M., Singleton, J. S., Gomila, R., Mavor, S. P., Heuser, G., Arancibia, G., Williams, S., & Stockli, D. F. (2021). Magnitude, timing, and rate of slip along the Atacama fault system, northern Chile: Implications for Early Cretaceous slip partitioning and plate convergence. *Journal of the Geological Society*, 178(3), jgs2020-142. [doi:10.1144/jgs2020-142](https://doi.org/10.1144/jgs2020-142)
- Sibson, R. H., Moore, J. Mc. M., & Rankin, A. H. (1975). Seismic pumping—A hydrothermal fluid transport mechanism. *Journal of the Geological Society*, 131(6), 653–659. [doi:10.1144/gsjgs.131.6.0653](https://doi.org/10.1144/gsjgs.131.6.0653)

- Sibson, R., Robert, F., & Poulsen, K. (1988). High-angle reverse faults, fluid-pressure cycling, and mesothermal gold-quartz deposit. *Geology*, 16. [doi:10.1130/0091-7613\(1988\)016<0551:HARFFP>2.3.CO;2](https://doi.org/10.1130/0091-7613(1988)016<0551:HARFFP>2.3.CO;2)
- Somoza, R. (1998). Updated Nazca (Farallon)—South America relative motions during the last 40 My: Implications for mountain building in the central Andean region. *Journal of South American Earth Sciences*, 11(3), 211–215. [doi:10.1016/S0895-9811\(98\)00012-1](https://doi.org/10.1016/S0895-9811(98)00012-1)
- van Dinther, Y., Mai, P. M., Dalguer, L. A., & Gerya, T. V. (2014). Modeling the seismic cycle in subduction zones: The role and spatiotemporal occurrence of off-megathrust earthquakes. *Geophysical Research Letters*, 41(4), 1194–1201. [doi:10.1002/2013GL058886](https://doi.org/10.1002/2013GL058886)
- Vermeesch, P., 2018, IsoplotR: a free and open toolbox for geochronology. *Geoscience Frontiers*, v.9, p.1479-1493, [doi:10.1016/j.gsf.2018.04.001](https://doi.org/10.1016/j.gsf.2018.04.001).

APPENDIX A: DIGITAL ELEVATION MODELS AND DRONE IMAGERY

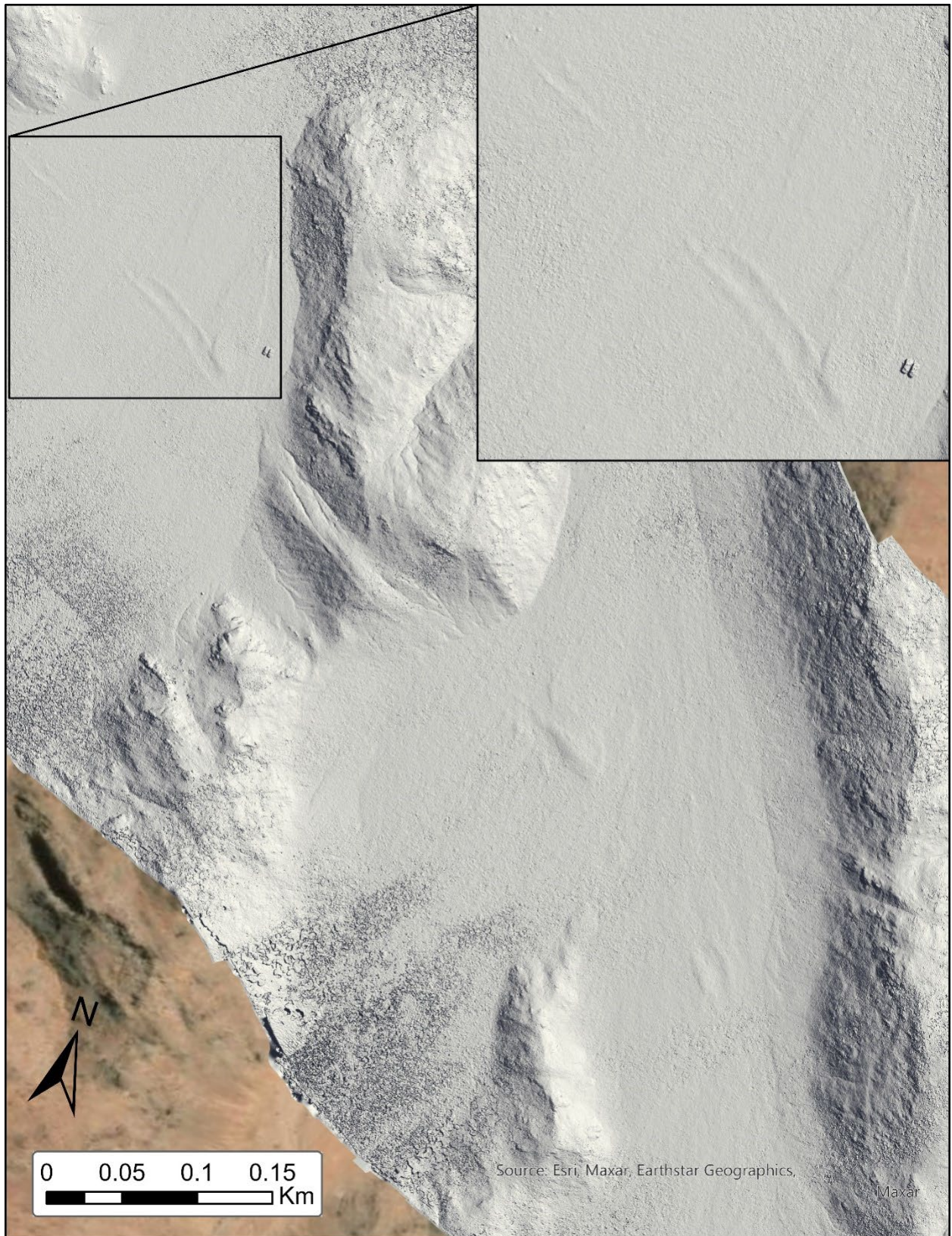


Figure A1. Site 003. Waypoint coordinates:  $-25.505623, -70.335153^\circ$ . Hillshade from DEM; flight 01\_10\_20\_1124\_1149.



*Figure A2.* Drone photos from site 003. View is roughly NW in both photos. Lineament crosses fractured bedrock outcrop and traces into the Quebrada Tipias Fault.

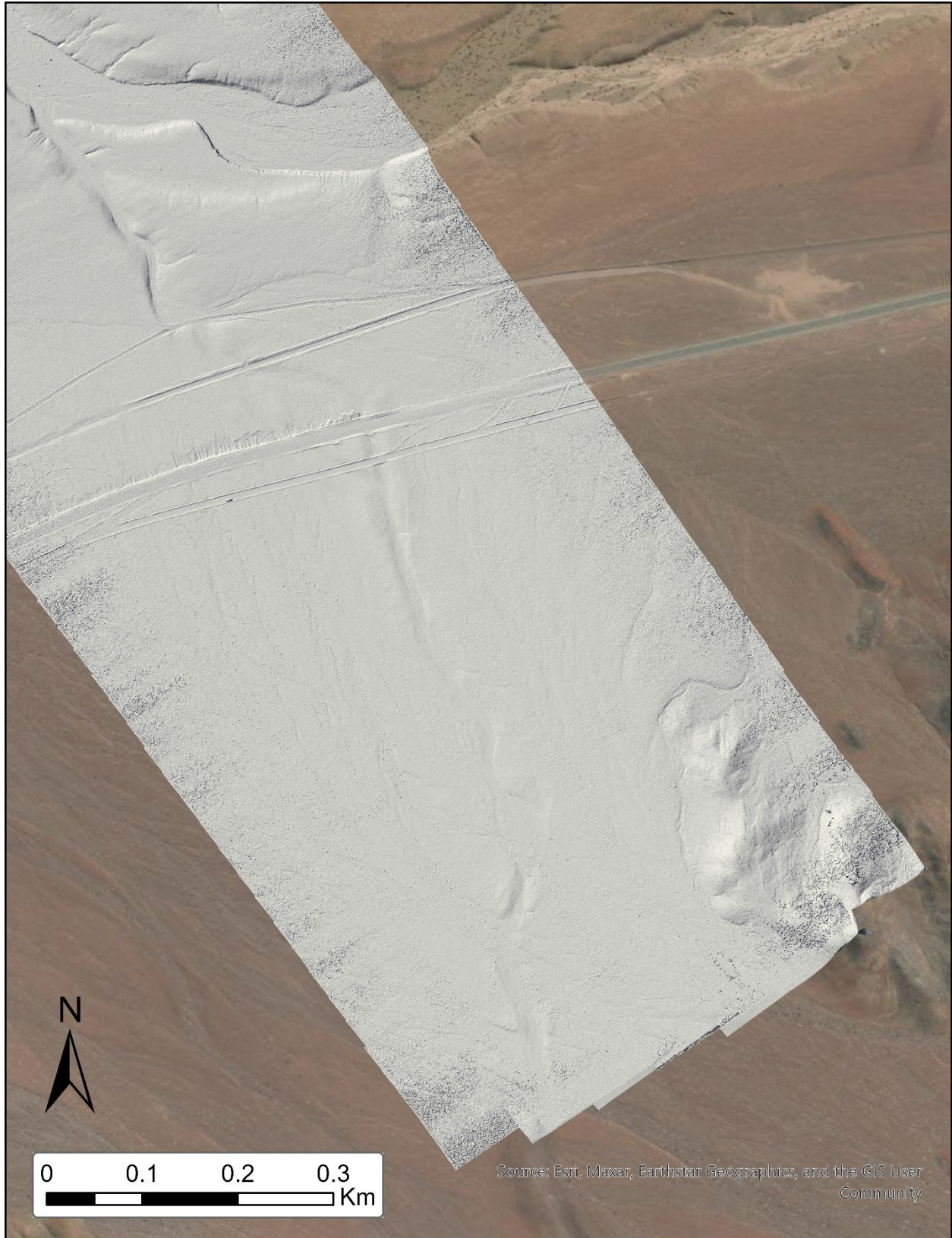
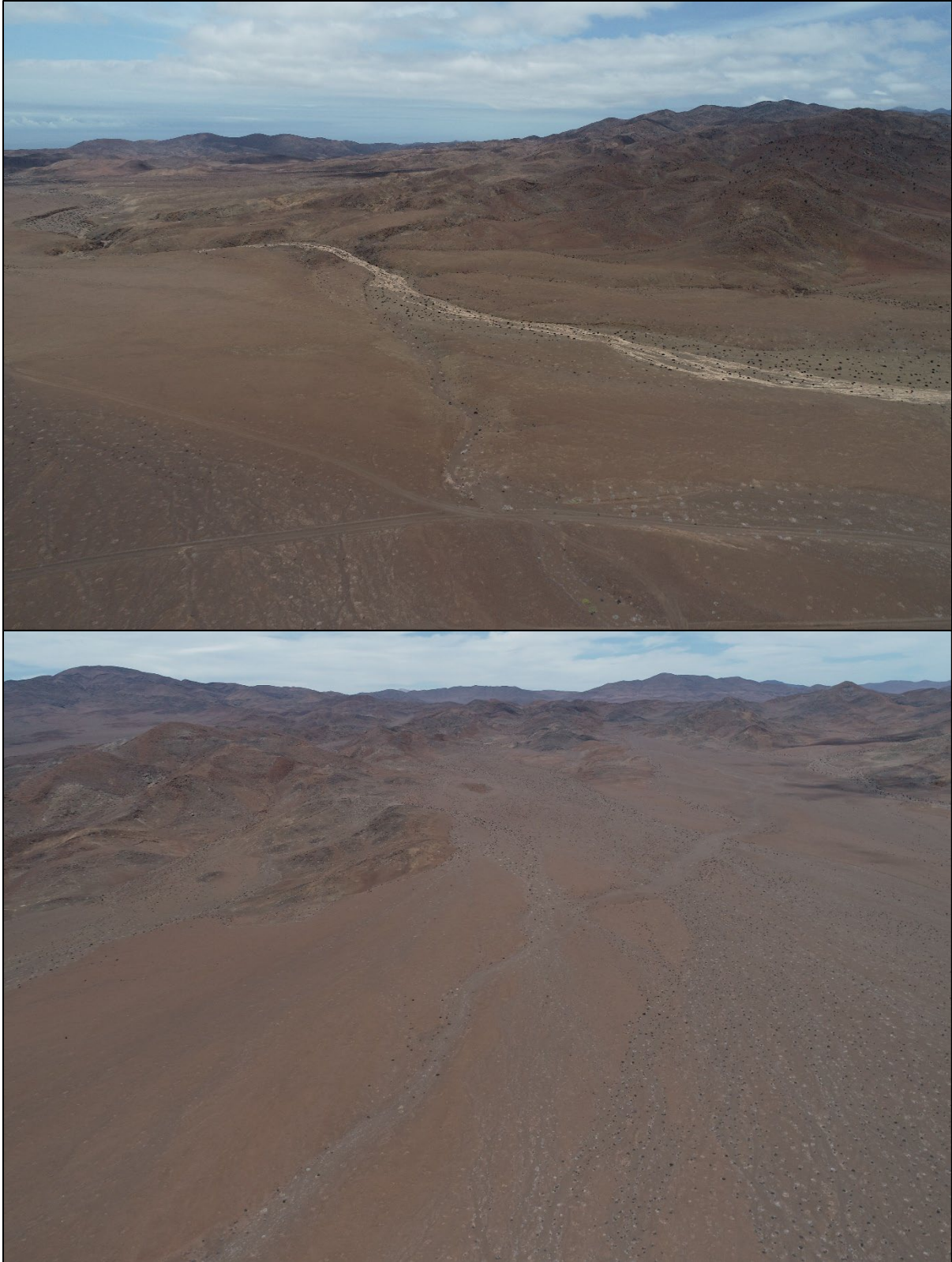


Figure A3. Site CL-010520-12. Waypoint coordinates: -25.539460, -70.467330°. Hillshade from DEM; flight 01\_14\_20\_1344.



*Figure A4.* Drone photos from site CL-010520-12. View is to NW in top photo, view is to S in bottom photo, showing a curvilinear lineament that intersects a major drainage.

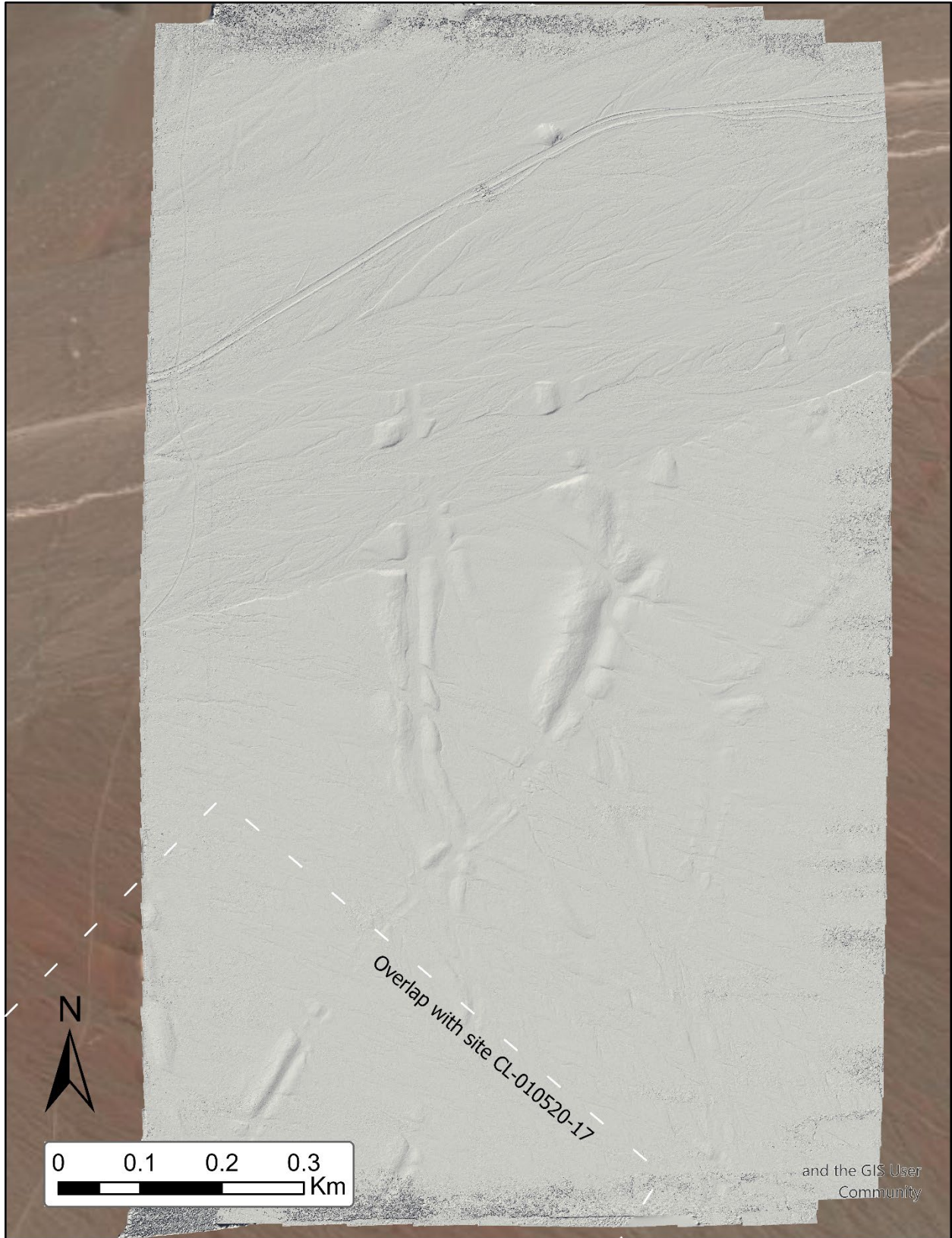
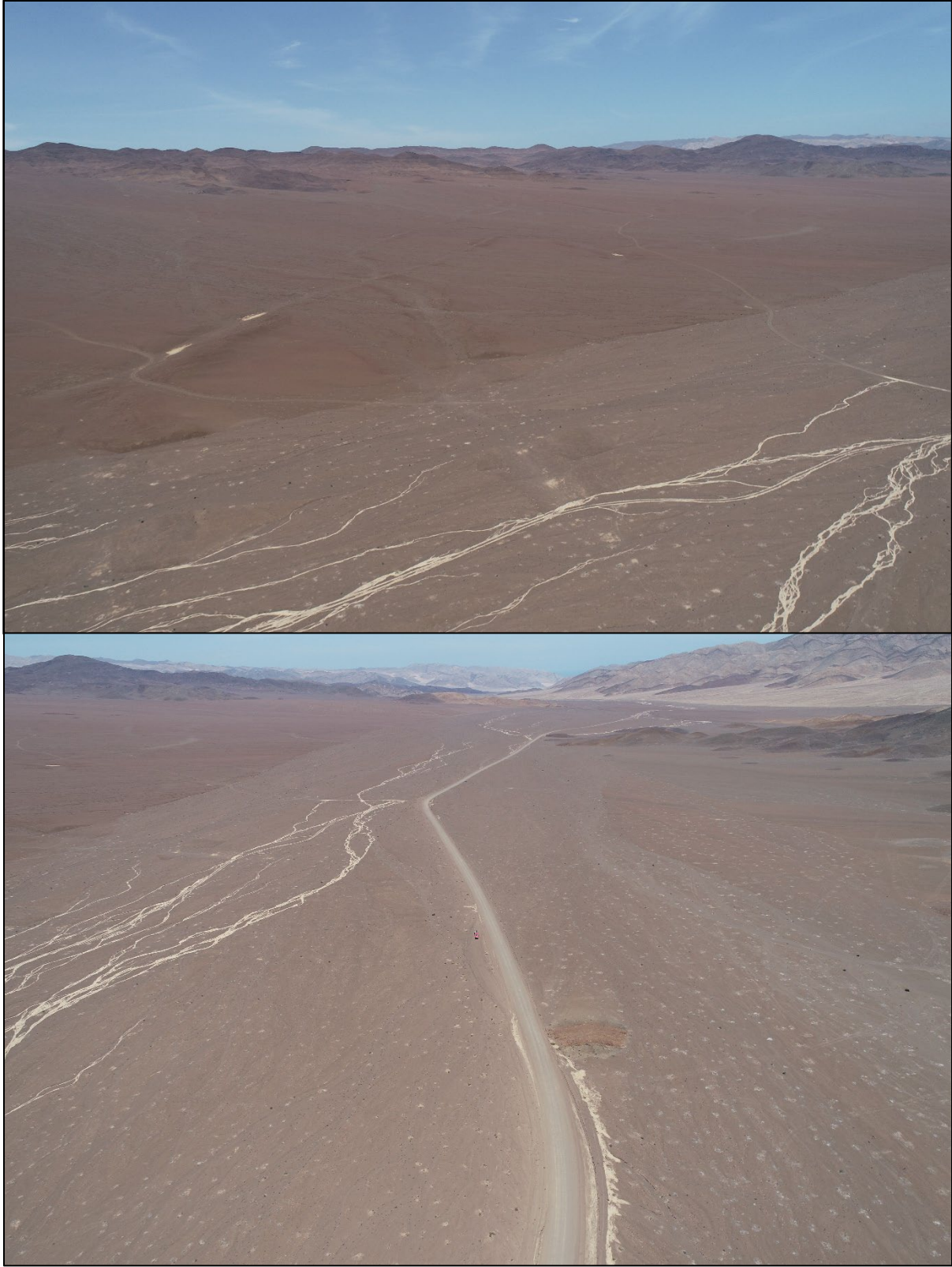


Figure A5. Site CL-010520-15. Waypoint coordinates: -25.616990, -70.502820°. Hillshade from DEM; flight 01\_16\_20\_1306.



*Figure A6.* Drone photos from site CL-010520-15. View is to the S in top photo, view is roughly E in bottom photo, showing two lineaments crossing and intersecting a modern drainage.

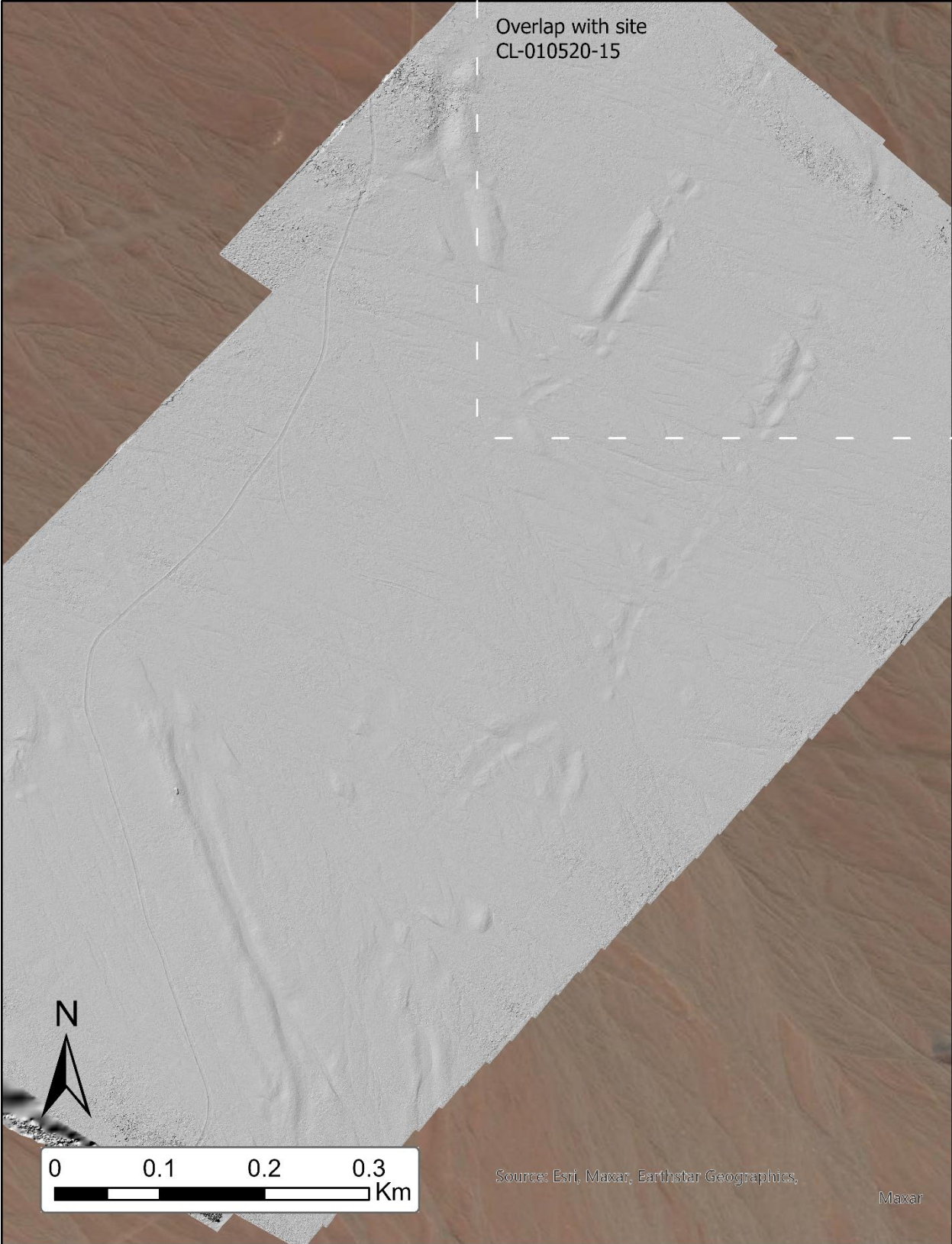


Figure A7. Site CL-010520-17. Waypoint coordinates: -25.626830, -70.508090°. Hillshade from DEM; flight 01\_16\_20\_1435.



*Figure A8.* Drone photos from site CL-010520-17. View is to the NW in top photo, roughly N in bottom photo. Crossing lineaments from CL-010520-15 are visible in the far distance; tip of lineament intersects drainage next to the road in bottom photo.

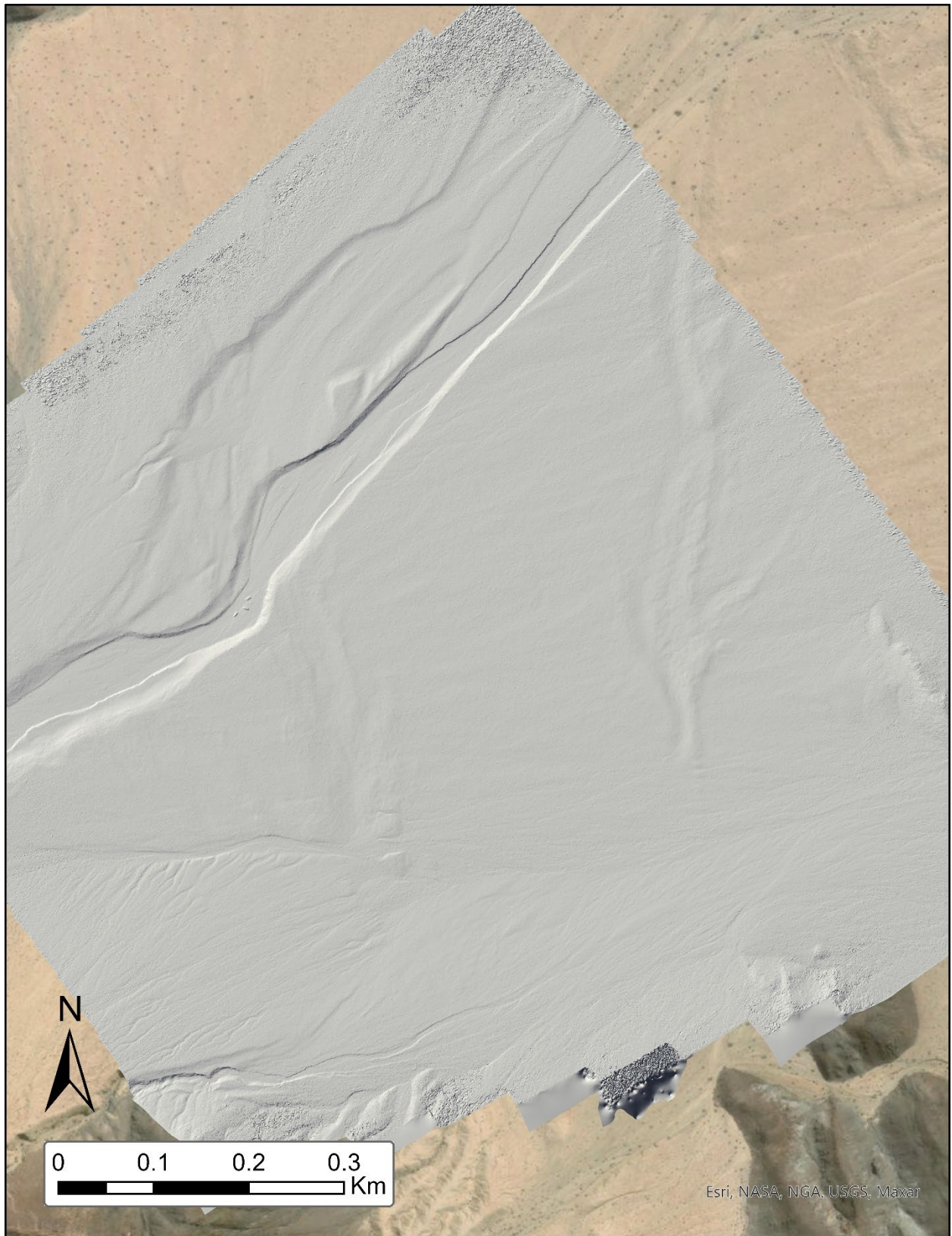


Figure A9. Site CL-010520-19. Waypoint coordinates:  $-25.703700, -70.574560^\circ$ . Hillshade from DEM; flight 01\_07\_20\_1239.



*Figure A10.* Drone photos from site CL-010520-19. View is to the SE in both photos, showing the lineament in cross-section (oblique). Subtle lineament ridges are low relief on the sloping fan surface where they intersect the drainage.

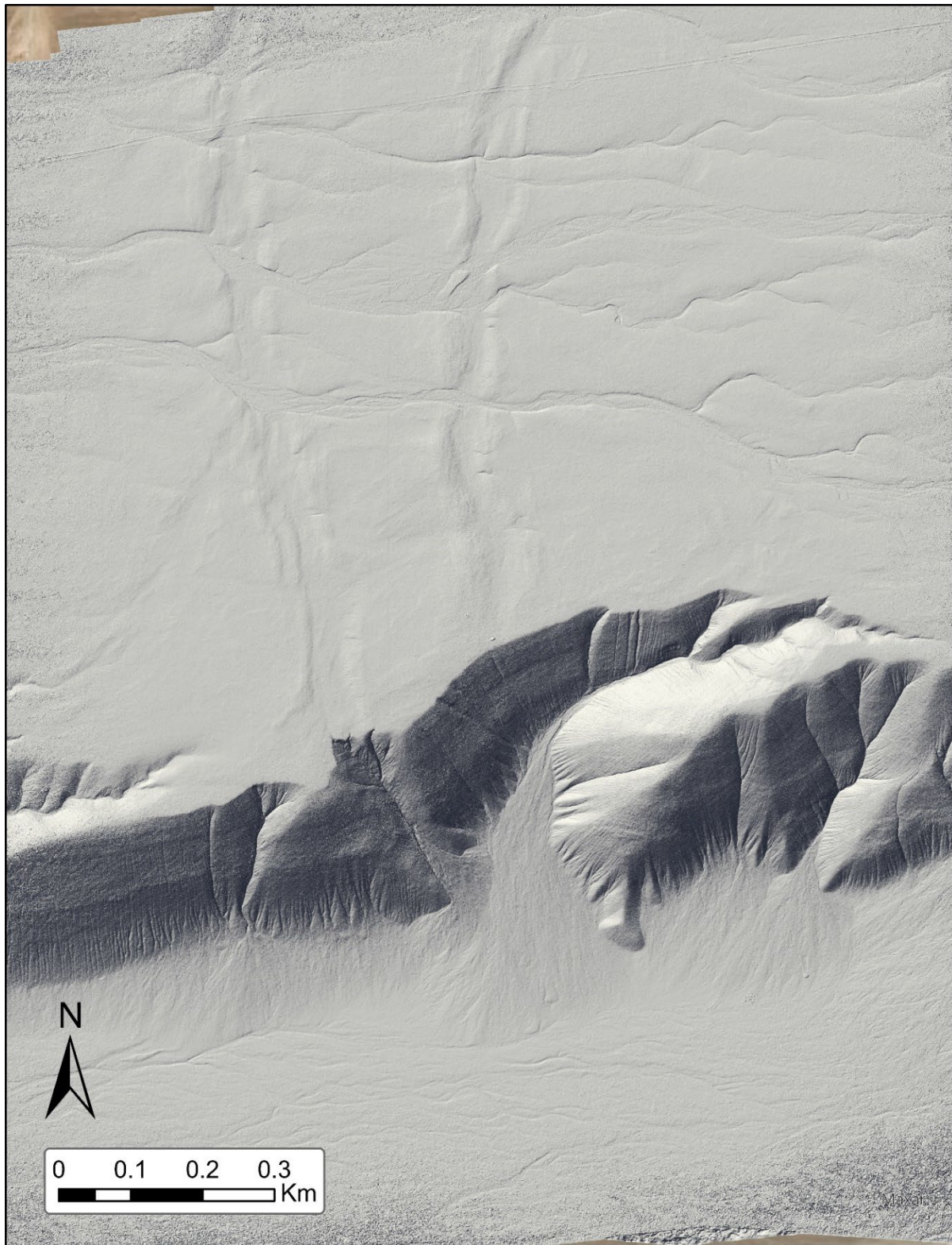
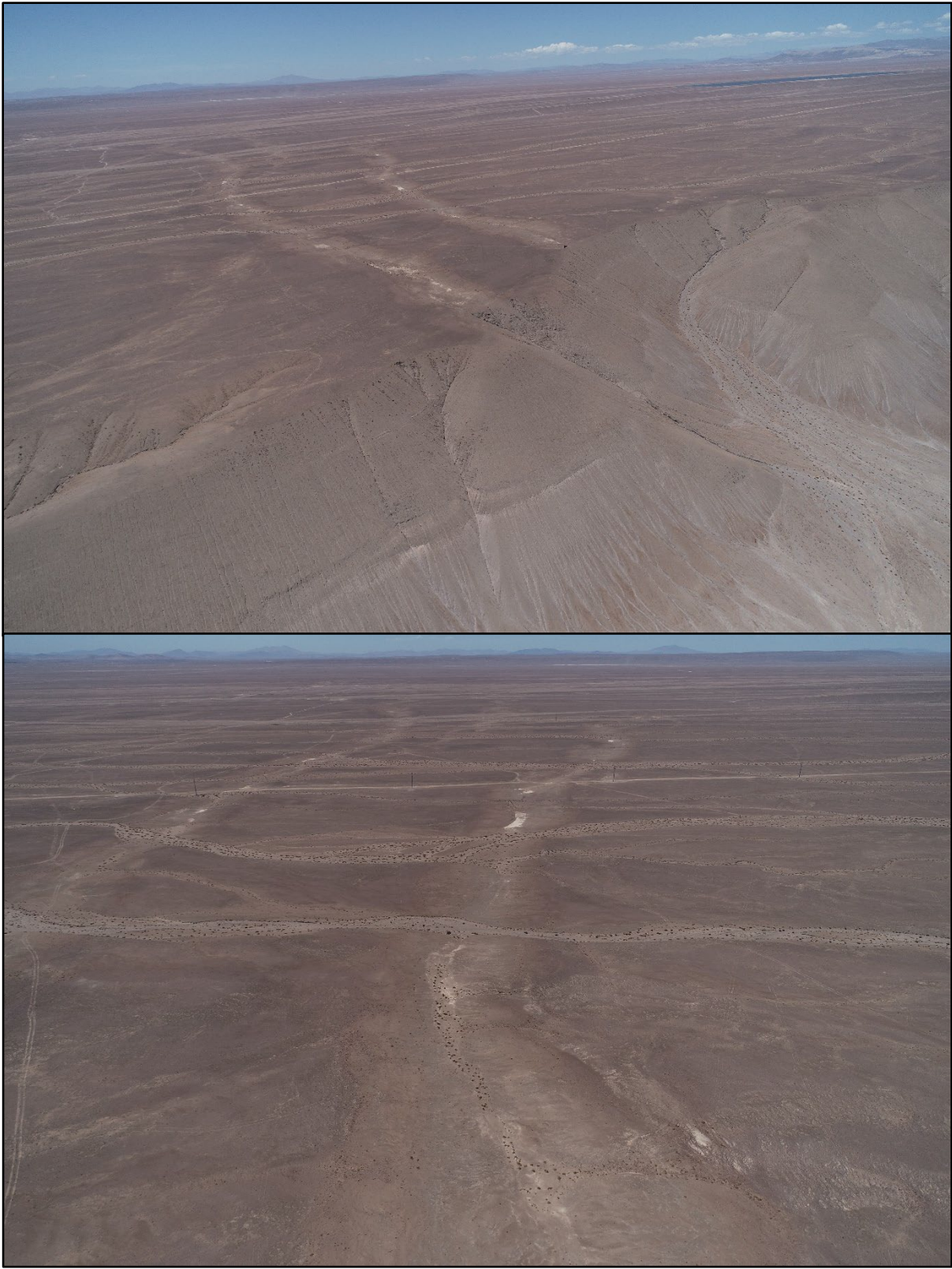


Figure A11. Site 035. Not shown on Figure 1b. Site is located ~40 km SE of area outlined in Fig. 1b, ~13 km ENE of town Diego de Almagro. Waypoint coordinates: -26.343315, -69.913235°. Hillshade from DEM; flight 01\_08\_20\_1356\_1421.



*Figure A12.* Drone photos from site 035. View is to the NW in top photo, view is to the N in bottom photo. Two curvilinear lineaments intersect major drainage, with the western lineament terminating in a fissure.

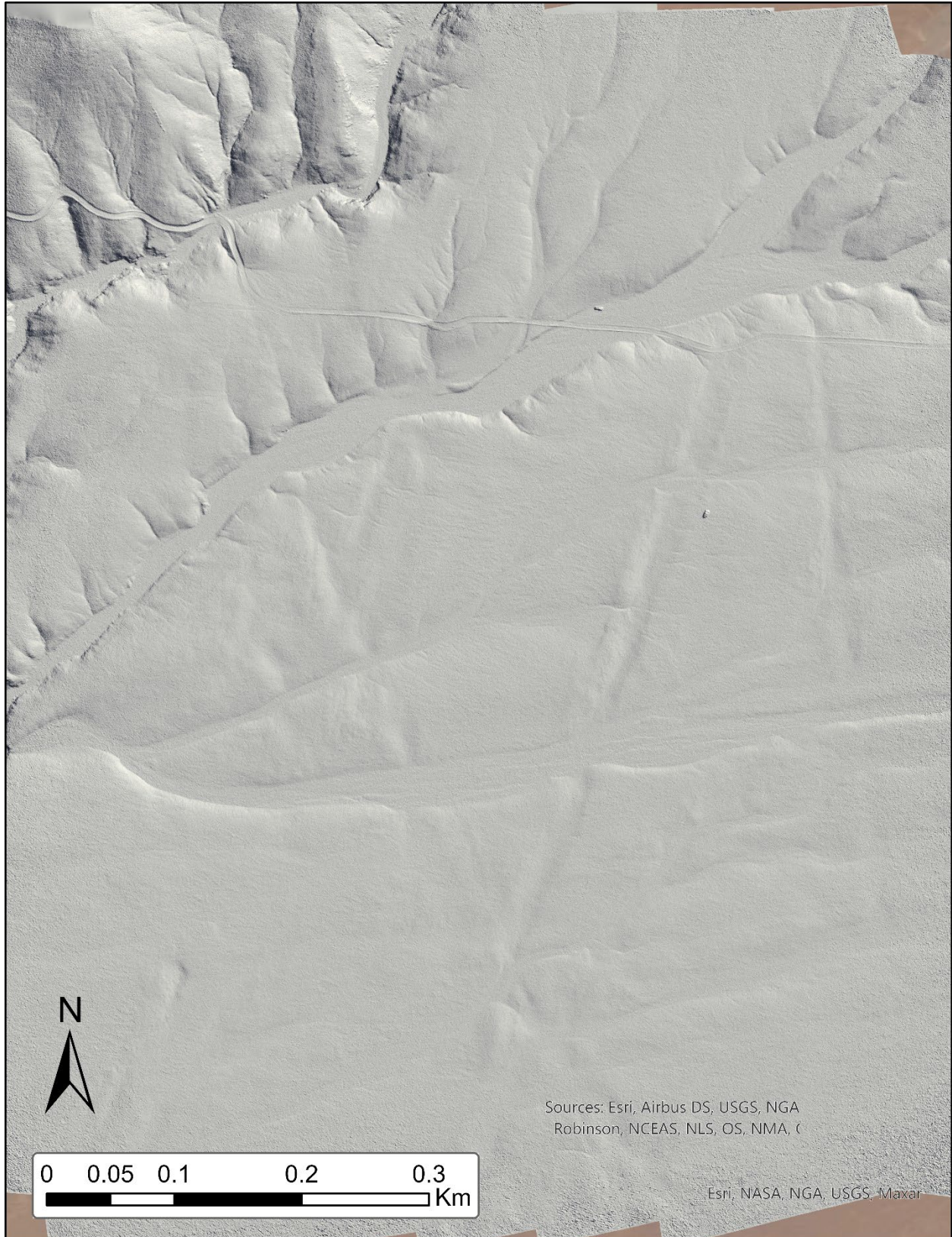
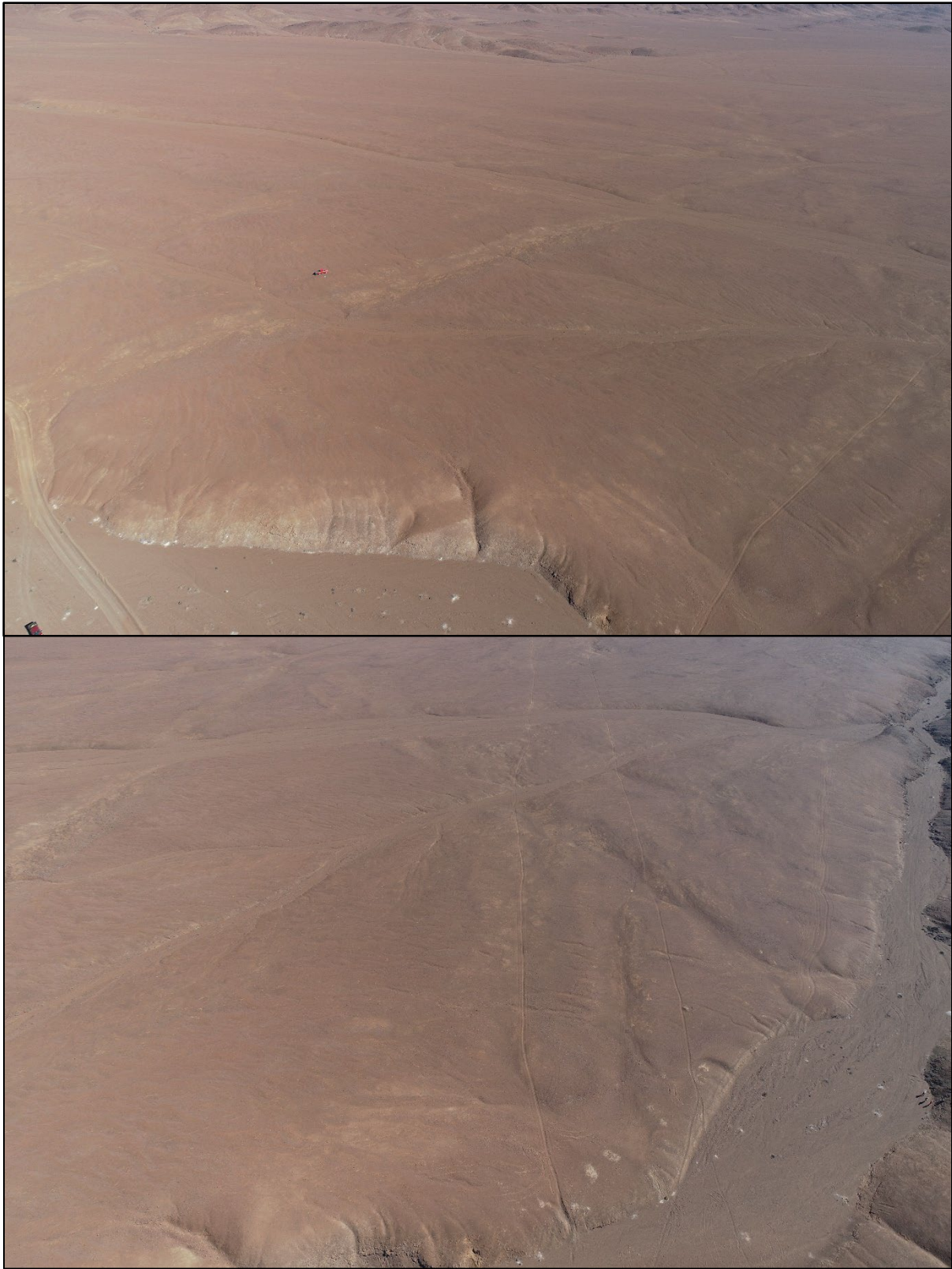
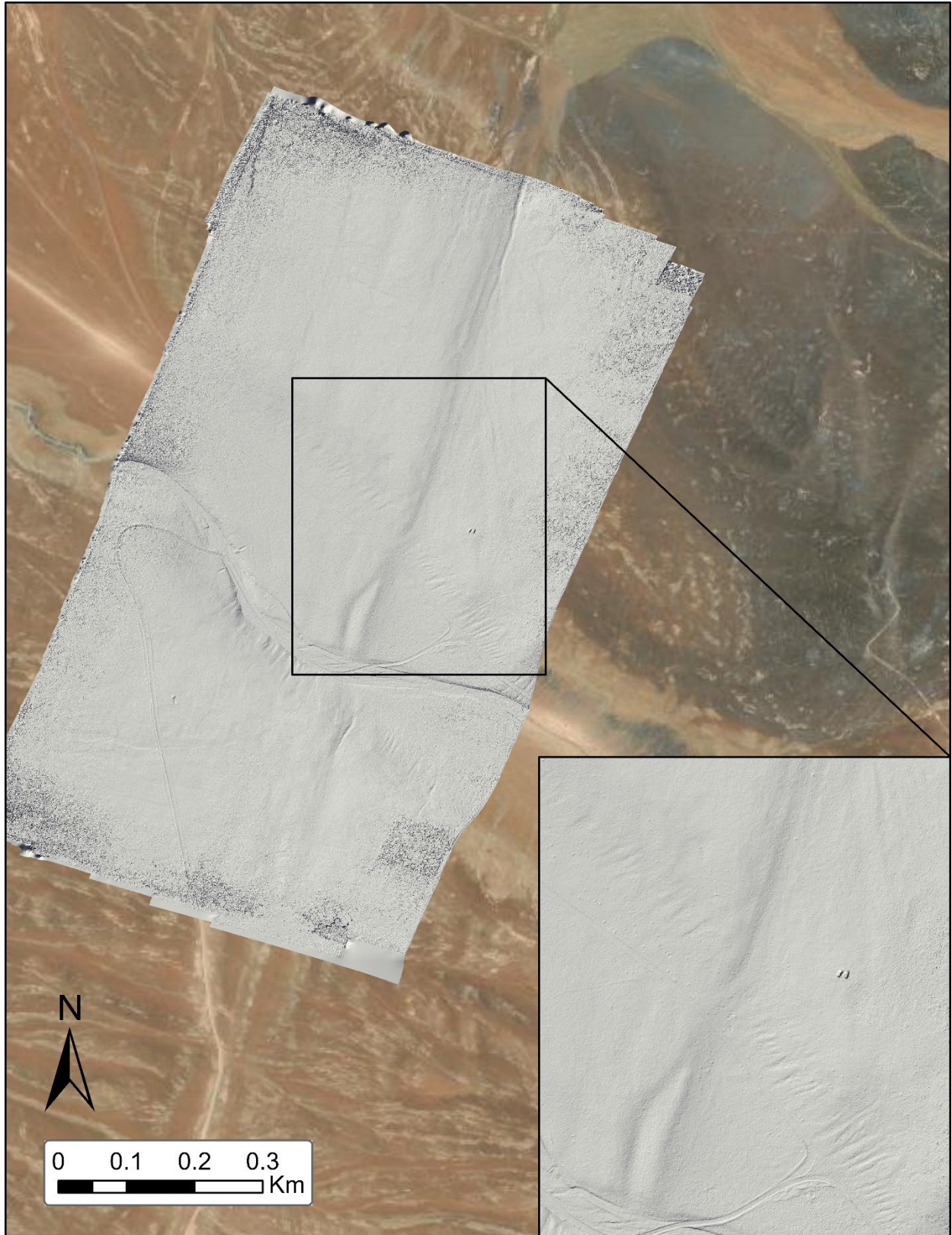


Figure A13. Site 047. Waypoint coordinates: -25.711973, -70.472788°. Hillshade from DEM; flight 01\_09\_20\_1736.



*Figure A14.* Drone photos from site 047. View is to the SE in top photo, view is to the S in bottom photo, showing multiple lineaments crossing.



*Figure A15.* Site 063. Not shown on Figure 1b. Site is located ~78 km E of area outlined in Fig. 1b, in the Precordillera. 1.4 km due S of site shown by Box B, Fig 4 in Audin et al., 2003. Waypoint coordinates: -25.832481, -69.348980°. Hillshade from DEM; flight 01\_12\_20\_0955.



*Figure A16.* Drone photos from site 063. View is to the SW in top photo, orthographic view in bottom photo (top of photo is S). Lineament intersects drainage in top photo, trucks immediately W of minor lineament ridge in bottom photo.

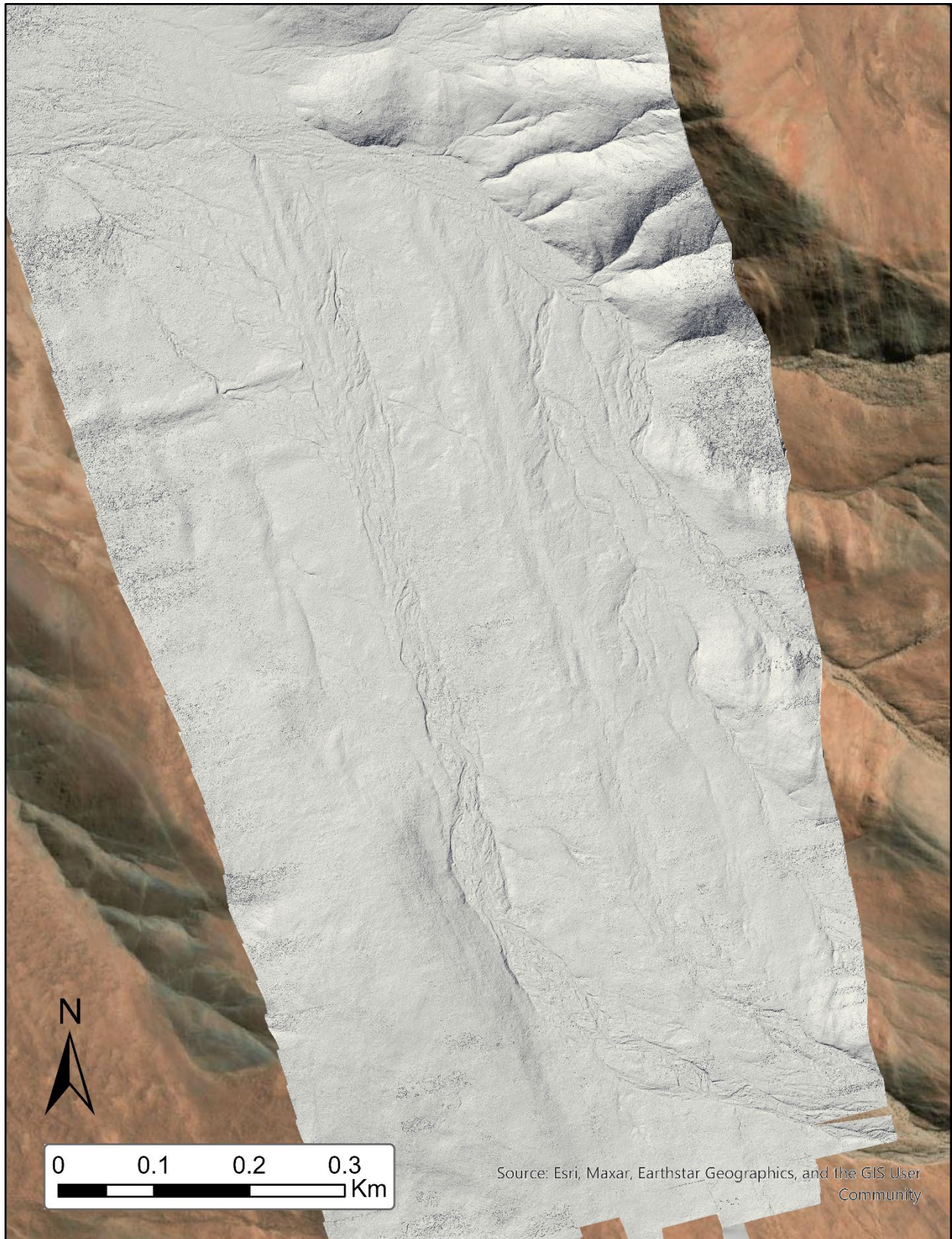


Figure A17. Site 074. Waypoint coordinates: -25.643036, -70.315940°. Hillshade from DEM; flight 01\_13\_20\_1341.



*Figure A18.* Drone photos from site 075. View is to the SE in top photo, view is roughly S in bottom photo. Two parallel lineaments (alluvium heavily incised by fluvial activity) trace over the eastern branch of the Atacama Fault.

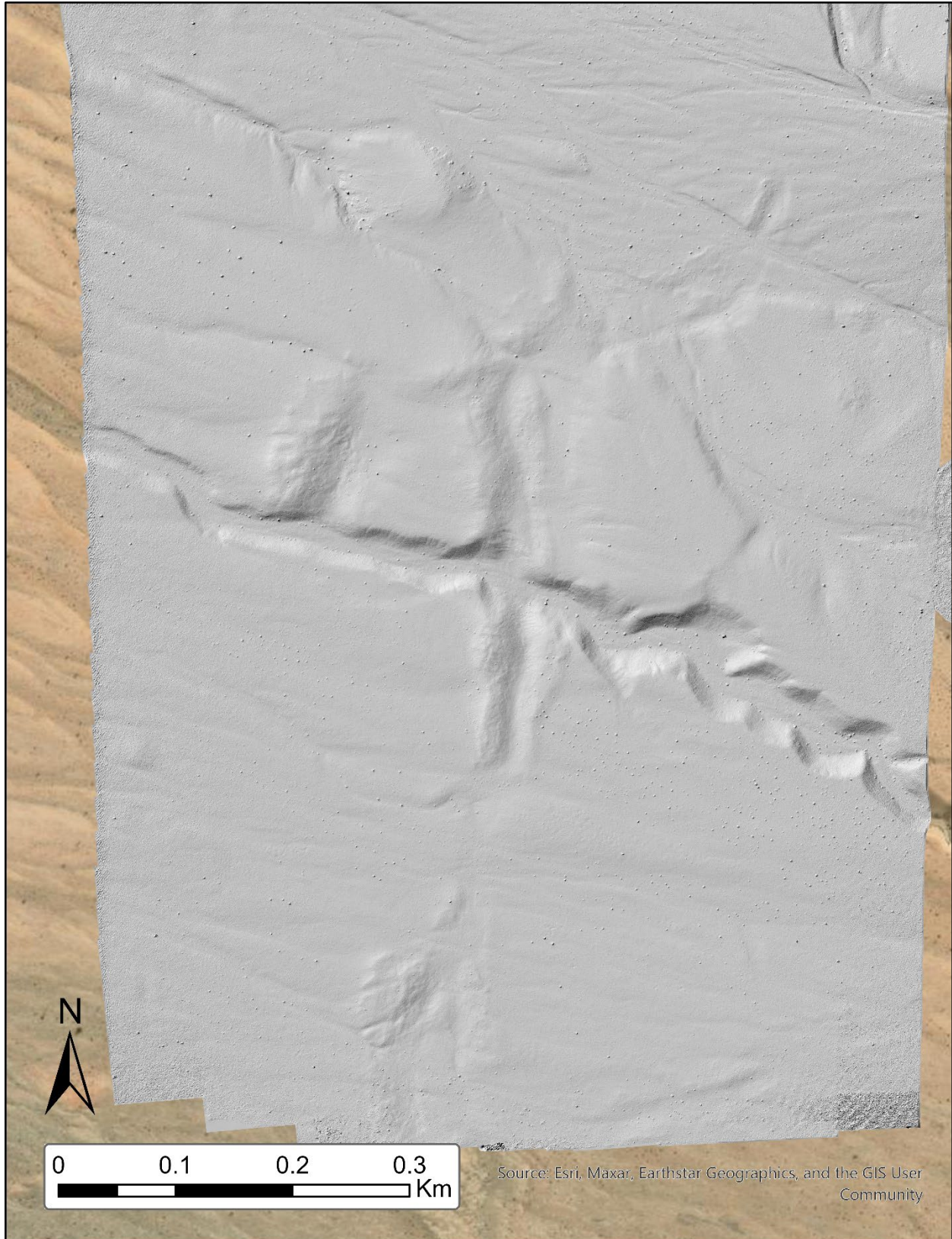
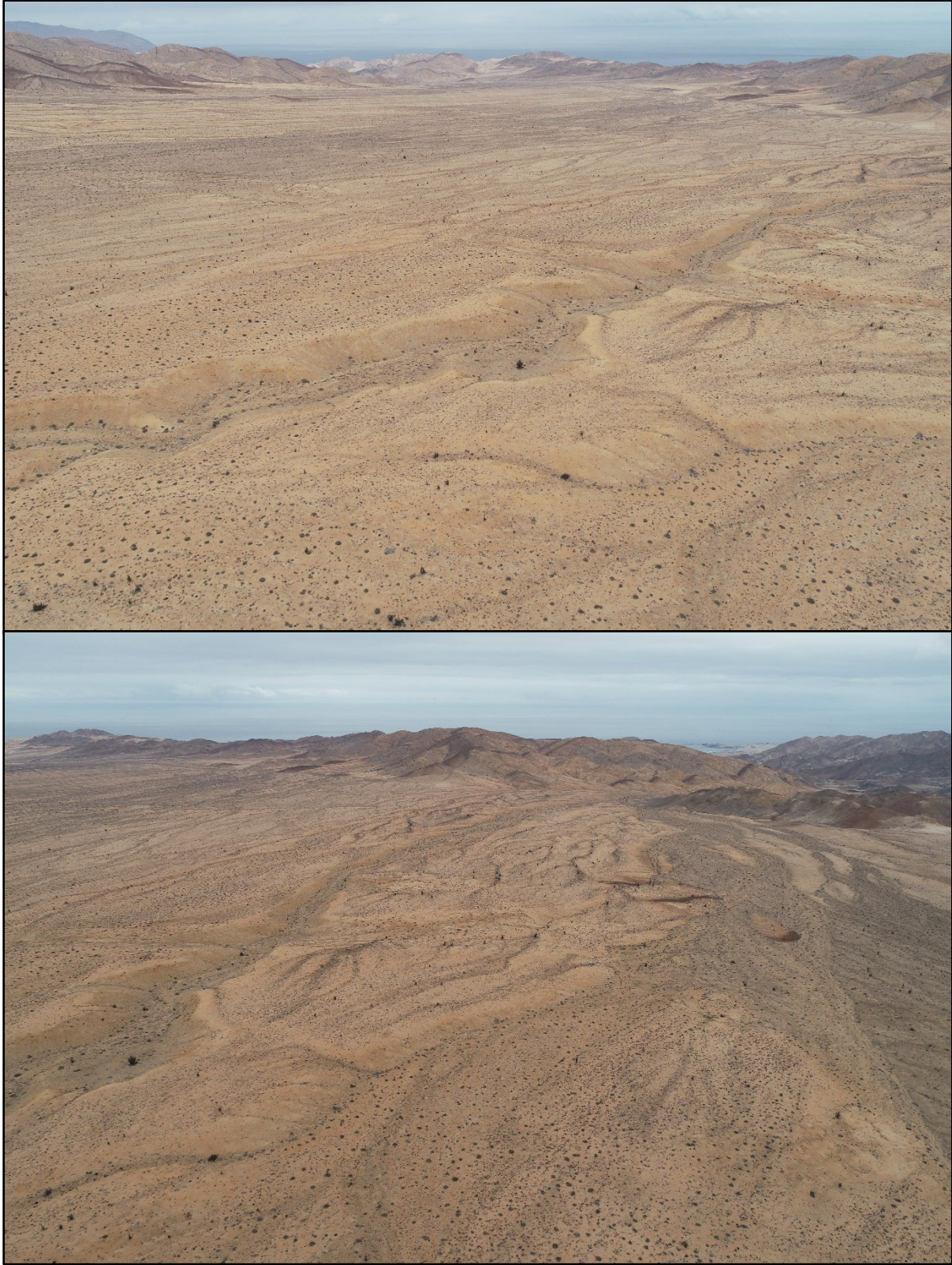


Figure A19. Site 079. Waypoint coordinates: -25.579251, -70.584099°. Hillshade from DEM; flight 01\_14\_20\_1048\_1107. Small bumps throughout DEM are individual cacti.



*Figure A20.* Drone photos from site 079. View is to the NW in top photo, view is roughly W in bottom photo. Central drainage intersects two N-striking lineaments with broad ridges.



*Figure A21.* Site CL-010520-08. View is to the NW in both photos, showing tuff sampled for U-Pb geochronology. Tuff is 5.8 m below fan surface and 3.2 m above the channel (measured with laser range finder).